The Density Profile of Clusters of Galaxies

Abell 1351 & Abell 1995

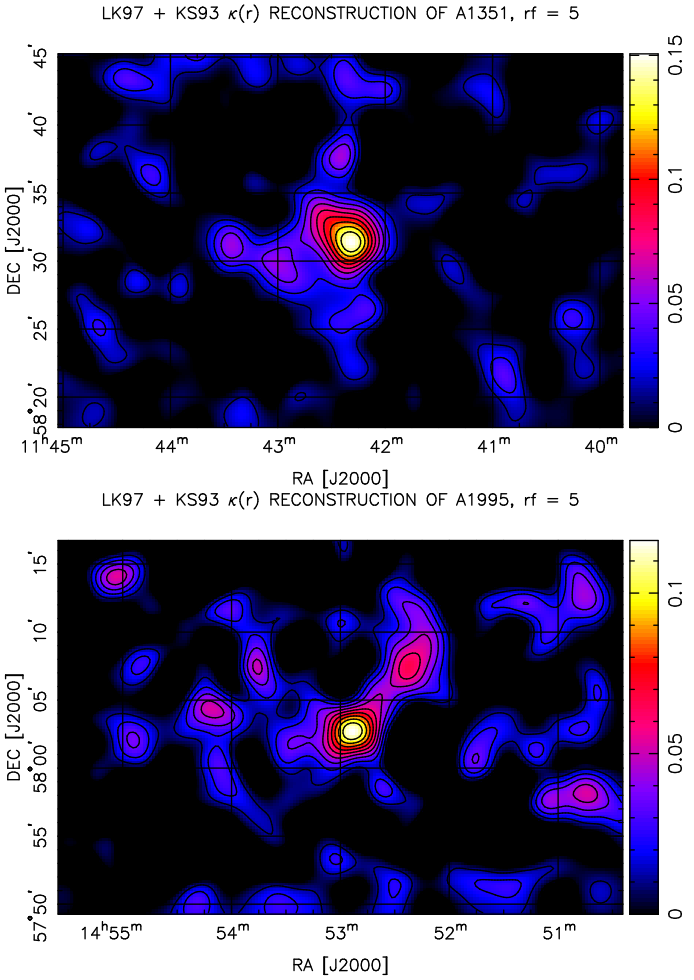

Master of Science thesis by
Karianne Holhjem
Institute of Theoretical Astrophysics
University of Oslo
Norway

March 2006

Contents

1 Introduction **1**

1.1 Cosmology . . . 3
1.2 Gravitational lensing . . . 5
1.2.1 Lensing geometry . . . 6
1.3 Mass estimations . . . 9
1.4 Dark matter . . . 12
1.5 Galaxy clusters . . . 13
1.5.1 Abell clusters . . . 13
1.6 The clusters Abell 1351 and Abell 1995 . . . 14
1.6.1 The fields of Abell 1351 and Abell 1995 . . . 15

2 Image reduction **19**

2.1 The CFH Telescope and the CFH12K camera . . . 20
2.2 Imaging: The charge-coupled device . . . 20
2.2.1 The CFH12K CCD . . . 23
2.3 IMCAT . . . 25
2.4 Bias and overscan . . . 26
2.5 Flat-field images . . . 27
2.6 Background . . . 30
2.7 Bad pixels and masking . . . 31
2.8 Astrometric calibration . . . 31
2.8.1 Orientation of the chips and cataloguing the objects . 32
2.8.2 The STScI Digitized Sky Survey and the USNO-B1.0 Catalogue . . . 33
2.8.3 Separating stars from galaxies . . . 34
2.8.4 Chip layout errors . . . 36
2.8.5 The reference system . . . 37
2.8.6 The low order spatial polynomial model . . . 38
2.8.7 Labelling the matching stars . . . 39
2.8.8 Astrometric solution . . . 39
2.8.9 Refining the solution . . . 40
2.9 The master image . . . 42
2.9.1 Gain variations and differential extinction . . . 42

2.9.2 Combining exposures . . . 44
2.9.3 Masking by examination . . . 45
2.10 Closing the reduction phase . . . 45

3 Weak lensing analysis **47**
3.1 Shear measurements . . . 48
3.1.1 Object ellipticities . . . 48
3.1.2 Correcting for the Point Spread Function . . . 50
3.2 Mass reconstruction . . . 55
3.3 Modelling the lensing data . . . 61
3.3.1 The singular isothermal sphere profile . . . 63
3.3.2 The NFW profile . . . 65

4 Discussion and conclusions **73**
4.1 Results . . . 73
4.1.1 Comparison with Dahle et al. 2002 . . . 78
4.2 Conclusion . . . 80
4.3 Future studies . . . 81

Bibliography **83**

A The shear-polarisation relation **87**

B Mathematical definitions **91**
B.1 Stereographic projection . . . 91
B.2 Taylor series . . . 91
B.3 The Bessel functions . . . 93
B.4 Convolution . . . 93
B.5 Maximum likelihood . . . 94

C IMCAT **95**
C.1 Using IMCAT . . . 95
C.1.1 Perl . . . 97

List of Figures

1.1 The deflection of starlight by the sun. 2
1.2 The effects of gravitational lensing. 6
1.3 Light deflection by a point mass. 8
1.4 The gravitational lens system. 8
1.5 The effects of shear and convergence on a circular image. . . . 10
1.6 The field of Abell 1351. 16
1.7 The field of Abell 1995. 17

2.1 The CFH12K CCD mosaic. 23
2.2 The 12 mask FITS files. 31
2.3 A size-magnitude diagram of Abell 1351. 35
2.4 A polarisation parameter diagram displaying stars. 37
2.5 Residuals in the image mapping, differences in the r-coordinates. 41
2.6 Residuals in the image mapping shown as vectors. 41
2.7 Residuals in the image mapping between the r-coordinates after corrections. 43
2.8 Residuals in the image mapping after corrections, shown as vectors. 43
2.9 The image used for masking purpose. 46

3.1 Ellipticities before PSF anisotropy corrections. 52
3.2 Ellipticities after PSF anisotropy corrections. 52
3.3 The approximate spacing of the bins used in estimating the PSF dilution. 54
3.4 Mass maps of Abell 1351 and Abell 1995. 58
3.5 Random noise in the mass maps of Abell 1351 and Abell 1995. 60
3.6 The percentage of cluster galaxies in the faint galaxy catalogues. 63
3.7 The percentage of cluster galaxies in the faint galaxy catalogues displayed in three dimensions. 64
3.8 The best fit values for the concentration parameter at a 68% confidence level. 68
3.9 Plot showing χ^2 as a function of c for the NFW profile with c as a free parameter. 69
3.10 The reduced tangential shear as a function of radius. 71

4.1 Mass maps of Abell 1351 and Abell 1995. 74

B.1 The map projection. 92
B.2 The stereographic projection. 92
B.3 Bessel functions of the first kind. 94

C.1 An example of a simple Perl script. 98

List of Tables

1.1 Characteristics about Abell 1351 and Abell 1995. 15

2.1 The mosaic layout. 24
2.2 Characteristics for each CCD. 24
2.3 CFH12K data. 25
2.4 Filter characteristics for the Cousins I band filter. 25

3.1 Best results for Abell 1351 and Abell 1995 I band shear profile using the SIS and NFW profiles. 70

Chapter 1

Introduction

The groundwork of modern science originated about 2500 years ago when Greek mathematicians and philosophers started describing natural phenomena using mathematics. Writing down their ideas, they preserved them for future generations. This concept then evolved into writing physical theories quantitatively in mathematical terms, making it possible to test the theories by observing nature.

Galileo Galilei was the first person to point a telescope towards the sky. His observations led to fundamentally new astronomical data since the Greeks started their recordings. The law of universal gravitation was then discovered by Isaac Newton, who later also postulated the theory that light is composed of particles. His particle theory dominated optics until the early 19th century when it was replaced by the wave theory of light. Later the two theories were combined in the modern quantum theory.

In 1905, Albert Einstein started a revolution in physics with his special theory of relativity, describing how measurements of distance, time, and mass are affected by motion. Ten years later his general theory of relativity included the effects of gravity and accelerating systems. Through this theory, Einstein predicted the path of light to be affected by nearby masses. This deflection of light was one of the first predictions of general relativity to be confirmed. In 1919 stars near the sun were observed during an eclipse. Measurements of the starlight proved it to be deflected by the sun, as shown in Figure 1.1.

Deflection of light by massive bodies and results from this process are now referred to as gravitational lensing. Although it is the oldest known observational consequence of general relativity, gravitational lensing is one of the newest areas in cosmology. The first gravitational lens ever observed was detected in 1979, when Walsh, Carswell and Weymann observed the twin quasi-stellar objects (QSO) 0957+561 (Walsh et al. 1979). The role of gravitational lensing is increasingly important, and as technology improves and wide-field cameras become more accessible, lensing studies are making

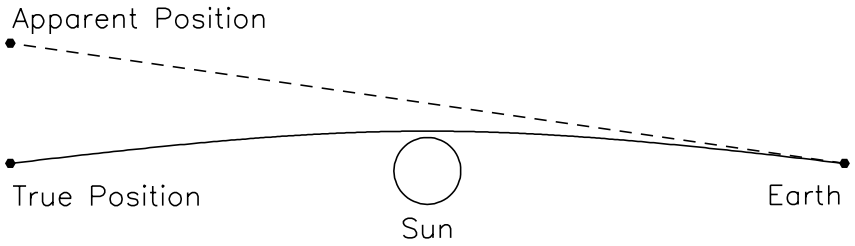

Figure 1.1: The deflection of starlight by the sun. The apparent position of the star moves away from the sun, as its light rays are bent towards the sun.

great contributions to the understanding of the large-scale structure in the universe.

Outline of the thesis

In this thesis the mass distributions of the galaxy clusters Abell 1351 and Abell 1995 are examined through gravitational lensing. The studies are based on observational data, where observed values are compared to theoretical models to obtain an estimate of the mass. Mass maps are also created to display the mass distributions of the clusters in two dimensions.

In this chapter a short introduction to the topics of cosmology and gravitational lensing is given together with some basic equations, and a summary is given concerning how the lensing measurements can be used to estimate the mass distribution of the lensing object. A brief overview is given concerning dark matter, whilst galaxy clusters are explained in more detail. Some basic data about Abell 1351 and Abell 1995 are presented, together with images showing the fields of the two clusters.

The historical introductions given throughout this chapter are based on summaries and descriptions given in the textbooks "Encyclopedia of astronomy and astrophysics", Murdin (2000), "Cosmology: The Origin and Evolution of Cosmic Structure", Coles and Lucchin (2002), and "Discovering the Universe", Comins and Kaufmann (2003), together with the compendium "Lectures on Gravitational lensing", Narayan & Bartelmann (1997). Facts and explanations are also taken from the web pages "Erik Weisstein's World of Physics"[1] and "Answers.com"[2].

In Chapter 2 image processing is explained. It covers a description of the telescope and camera used in obtaining the observational data used in

[1] http://scienceworld.wolfram.com/physics/
[2] http://www.answers.com/

this thesis. It also gives an introduction to CCD cameras, together with a small description of the `IMCAT` software used for reduction and analysis throughout this thesis. The image reduction is then discussed in detail, as is the astrometric calibration of the data in this thesis. The production of a final image by co-addition of all exposures is treated towards the end of the chapter.

In Chapter 3 a detailed summary of the weak lensing analysis done in this thesis is given. A description of the measurements and how they were carried out is presented, together with details of corrections of Point Spread Function (PSF) variations caused by the instrument. The reconstruction of the mass distribution is explained, first by generating mass maps, and then by modelling the lensing data to fit realistic density profiles. The chapter also gives an introduction to the theories behind the mass estimates presented here. Finally the results from the fittings are presented in a table.

A small summary is given in Chapter 4. The chapter also presents a discussion of the results obtained, these being compared to outcomes from other papers presenting similar mass analyses.

1.1 A brief introduction to cosmology

Cosmology is the study of the large-scale structure of the universe. Trying to derive a model of the universe, Newton assumed a homogeneous and isotropic, yet static universe. He never succeeded, realising that the universe was in fact unstable. With the theory of general relativity at hand, Einstein derived another model. Concluding, like Newton, that for a finite universe a stable model was not permitted, he introduced the cosmological constant, Λ, which implied a repulsive force that varied directly with distance. The resulting model could then be derived as static, requiring the universe to be closed.

At the same time de Sitter developed another model, predicting an expanding universe. Although the model was considered exotic and controversial at the time, it later became of great influence to cosmology. The deduction of Hubble's law lead to the models of an expanding universe to get more attention. Hubble's law is given by $v = Hr$, and states that the radial velocity, v, of a typical galaxy moving away from us is directly proportional to its distance, r, from us. H is the Hubble constant (explained later this section). Because of this law Einstein later concluded that a static model was unrealistic, and abandoned his cosmological constant. Despite Einstein's own conclusion Λ is still a disputed topic.

Models of the universe are based on an assumption called the cosmological principle, stating that the universe is homogeneous and isotropic. This implies that on large enough scales the universe looks the same from all positions and in all directions in space. The simplest model is the Einstein-

de Sitter model, assuming a flat universe (no curvature) and $\Lambda = 0$.

The Hubble constant is defined by

$$H \equiv \frac{\dot{a}}{a} , \tag{1.1}$$

where a is the expansion parameter, both evaluated at epoch t. Here a is a function to be determined which has the dimensions of a length, and is also called the cosmic scale factor. It is related to redshift, z, by $a_0/a = 1 + z$, where $a_0 = a(t_0)$ and t_0 represents the present epoch. Equation (1.1) implies that more distant objects are receding faster than closer ones, and states that $H_0 = H(t_0)$ represents the current rate of expansion of the universe. Since there is some uncertainty in the value of H_0, cosmologists usually parametrise it in terms of a dimensionless number, h, such that

$$H_0 = 100\ h\ \mathrm{km\ s^{-1}\ Mpc^{-1}} \tag{1.2}$$

The critical density at t is defined as

$$\rho_c = \frac{3H^2}{8\pi G} , \tag{1.3}$$

where G is the universal gravitational constant, $G = 6.672 \times 10^{-11} \mathrm{Nm^2/kg^2}$. The density parameter is defined by

$$\Omega = \frac{\rho}{\rho_c} . \tag{1.4}$$

In a universe containing no dark energy (and hence $\Lambda = 0$) the critical density determines the closure of the universe, as it is the density required for the universe to stop expanding, and eventually collapse. As the universe is strongly believed to contain dark energy this approach is no longer valid, but for historical reasons ρ_c is still called the critical density. The parameter is still an important part of modern physics and astronomy.

Observational cosmology seeks to measure the expansion parameter accurately and use the results to derive the material content of the universe. The ΛCDM (Cold Dark Matter) model is a simple cosmological model postulating a flat universe, where a fraction, Ω_M, of the mass-energy density is predominantly cold matter. Cold matter is matter having a velocity much smaller than the speed of light at the onset of galaxy formation. The remaining fraction, $\Omega_\Lambda = 1 - \Omega_M$, is a constant dark energy density. Dark energy is a repulsive force, opposing the self-attraction of matter. It causes the expansion of the universe to accelerate, and one possible explanation is the cosmological constant. Since the ΛCDM model assumes a flat universe, these densities sum to one, $\Omega_0 = \Omega_\Lambda + \Omega_M = 1$. A universe containing curvature needs to include a parameter accounting for this, resulting in the equation

$$\Omega_\Lambda + \Omega_M + \Omega_k = 1 \tag{1.5}$$

Generalising observations of many different cluster luminosities to the universe as a whole provides a method of estimating Ω_M. By assuming that the mass-to-luminosity ratio is the same for individual clusters and for all clusters seen together, the mass of the universe is the only unknown parameter and can hence be calculated. Gravitational lensing provides a way of measuring the mass without making any assumptions between mass and light, and offers a method to examine and measure Ω_M from direct observations of mass. This is one of many reasons why gravitational lensing studies are important in present and future cosmology.

1.2 Gravitational lensing

Gravitational lensing occurs when stars, entire galaxies, or clusters of galaxies focus light from more distant objects. This thesis will mainly cover gravitational lensing by galaxy clusters only, as the two gravitational lenses studied in this thesis are clusters of galaxies. Figure 1.2 shows the effect as light from the source (distant object) passes the lens (galaxy cluster). The gravitational field of the lensing object will bend light rays in such a way that the image of the distant object is altered if its light passes close enough to the foreground mass. Depending on the mass of the lens and the relative positions of lens and background source, the observed effect varies. Gravitational lensing measurements depend solely on gravitation and geometrical properties like source and lens position. Lensing mass measurements are therefore independent of the dynamical state of the gravitating object,and offer an ideal way to detect and study dark matter.

Strong lensing produces multiple images of the same source, all having very distorted object shapes observed as big arcs. *Weak lensing* causes the shape of the image to change, this is usually seen as an elongation of the image in one direction. *Very weak lensing* is only detected by measuring the object shapes of a large number of objects and looking for statistical alterations.

X-ray studies and virial analysis vs. lensing studies

Unlike mass estimations obtained from X-ray studies or virial analyses, lensing mass measurements of galaxy clusters are independent of the dynamical state of the gravitating matter. While X-ray studies are based on the assumption of hydrostatic equilibrium in the cluster X-ray gas and virial analyses are based on the assumption of dynamical equilibrium in the cluster, lensing studies make no such assumptions. As a result, there are no restrictions on the dynamical states of the clusters examined by gravitational lensing. The studies can be applied to systems undergoing major merger events as well as to dynamically relaxed clusters, whereas X-ray and virial analysis data can only be used to obtain precise mass measurements for the latter type.

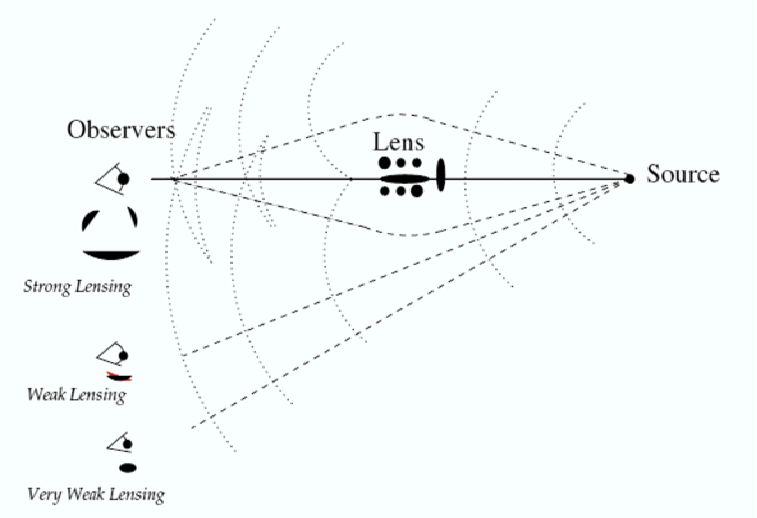

Figure 1.2: The effects of gravitational lensing. Images of the source are seen in the direction normal to the wavefront. If the wavefront is delayed enough by the lens, parts of it can double itself. The source is then seen as multiple images (strong lensing) or as a single image (weak lensing), depending on the relative positions of lens and background source with respect to the observer. Due to the gravitational lensing the size and shape of the images are usually altered. The figure is taken from Narayan & Bartelmann (1997).

1.2.1 Lensing geometry

General relativity is needed to express the details of how photons are affected by a gravitational field. However, in astrophysics some useful approximations apply which make the physics of this process much simpler. The effect gravitation has on light can hence be expressed through a wavefront approach. A wavefront is the locus of points given the same light travel time from the source (see Figure 1.2). As the wavefront crosses the observer an image of the source is seen in the direction normal to the wavefront. Normally light travels in straight lines, the wavefront being an expanding sphere. But if parts of the wavefront pass through a gravitational field these parts will be delayed, as the effective speed of light is reduced relative to propagation in vacuum. The shape of the wavefront therefore changes, and hence also the direction normal to it, i.e. the position of the image. This is equivalent to saying that the light ray is bent. Given a large enough delay the wavefront will double itself, leading to multiple images.

There are four standard approximations applied in gravitational lensing:

- The gravitational fields are weak enough that massive particles follow Newtonian dynamics.
- As the extent of the lens mass in the line of sight is negligible compared

with the distances between source and lens and observer, the lens behaves as if it had only a two-dimensional mass distribution projected along the line of sight.

- As the lens and the source are nearly aligned along the line of sight, the angular separation on the sky between lens and source is small enough to apply the approximation $\sin \angle \simeq \angle$.
- The effects of diffraction[3] are negligible.

Figure 1.3 displays the bending of light towards a point mass, M. Applying the above approximations this can be described as the bending of a light ray by an angular amount $\hat{\alpha}$, defined as the deflection angle and given by

$$\hat{\alpha} = \frac{4GM}{c^2 b} \, . \tag{1.6}$$

Here G is the gravitational constant, c is the speed of light and b is the angular distance between M and the unperturbed light ray, called the impact parameter. The effect of a distributed mass is the sum of contributions from all points making up the mass distribution.

A gravitational lens system has the geometry shown in Figure 1.4 (Refsdal 1964). S is the source position, O is the position of the observer, and $\hat{\alpha}$ is the deflection angle. β is the angle between the optic axis and the true source position, and θ between the optic axis and the image, I. D_d, D_{ds} and D_s are the angular diameter distances between observer and lens, lens and source and observer and source respectively[4]. The parameter η is the distance from S to the optic axis, orthogonal to this, and ξ is the impact parameter. The reduced deflection angle, α, is given by

$$\alpha = \frac{D_{ds}}{D_s} \hat{\alpha} \, . \tag{1.7}$$

It is seen from Figure 1.4 that

$$\theta D_s = \beta D_s + \hat{\alpha} D_{ds} \, . \tag{1.8}$$

From this the *lens equation* is derived, giving the relation between the positions of source and image:

$$\beta = \theta - \alpha(\theta) \, . \tag{1.9}$$

As the equation is nonlinear in the general case, the possibility of multiple images corresponding to a single source position is present.

From the assumption made earlier the mass of the lens can be treated as two-dimensional. While considering a lens with constant surface mass density, Σ, M can therefore be calculated from

$$M(\xi) = \Sigma \pi \xi^2 \, . \tag{1.10}$$

[3]Diffraction denotes the breaking up of light as the light passes an object.

[4]Note that as $D_{d,ds,s}$ are defined in curved space-times, in general $D_{ds} \neq D_s - D_d$.

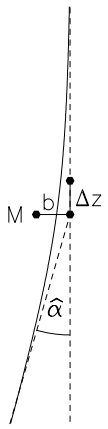

Figure 1.3: The bending of light by a point mass, M. The dashed line represents the unperturbed light ray. The ray passes M at the impact parameter, b, and is bent by an angle $\hat{\alpha}$. Most of this deflection takes place within $\Delta z \sim \pm b$ from the point of closest approach. The solid line represents the true light ray. The figure is taken from Narayan & Bartelmann (1997).

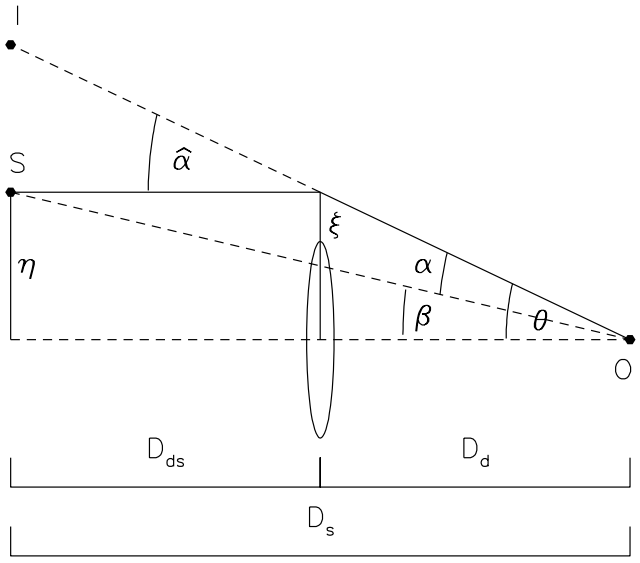

Figure 1.4: The gravitational lens system. The light from the source, S, is deflected by an angle $\hat{\alpha}$ and reaches the observer, O. The angle between the optic axis and the true source position is given by β, and the angle between the same axis and the image, I, is given by θ. D_d, D_{ds} and D_s are the angular diameter distances between observer and lens, lens and source and observer and source respectively. The distance from S to the optic axis is given by η, and ξ is the impact parameter.

The reduced deflection angle is hence given from equations (1.6) and (1.7) by

$$\begin{aligned} \alpha(\theta) &= \frac{D_{ds}}{D_s}\frac{4G}{c^2\xi}(\Sigma\pi\xi^2) \\ &= \frac{4\pi G\Sigma}{c^2}\frac{D_d D_{ds}}{D_s}\theta \ , \end{aligned} \tag{1.11}$$

with $\xi = D_d\theta$. The *critical surface mass density*, Σ_{crit}, is defined by

$$\Sigma_{crit} = \frac{c^2}{4\pi G}\frac{D_s}{D_d D_{ds}} \ . \tag{1.12}$$

Given a lens with a constant $\Sigma = \Sigma_{crit}$, equation (1.11) yields a deflection angle of $\alpha(\theta) = \theta$, resulting in $\beta = 0$ for all θ.

The Einstein radius

Using equation (1.10) and (1.11) the lens equation can be written as

$$\beta(\theta) = \theta - \frac{D_{ds}}{D_d D_s}\frac{4GM(\theta)}{c^2\theta} \ . \tag{1.13}$$

A source lying exactly on the optic axis ($\theta = 0$) of a circularly symmetric lens will be imaged as a ring due to the rotational symmetry of the lens system. The mass profile of the lens is arbitrary, but the lens must be supercritical, $\Sigma > \Sigma_{crit}$, for the phenomenon to occur. The radius of the ring is defined as the *Einstein radius*, θ_E, and is given by setting $\beta = 0$ in equation (1.13),

$$\theta_E = \left[\frac{4GM(\theta_E)}{c^2}\frac{D_{ds}}{D_d D_s}\right]^{1/2} \ . \tag{1.14}$$

The Einstein radius is important in describing gravitational lensing geometry. $2\theta_E$ is the typical angular separation of multiple images, and in many lens systems the Einstein ring represents an approximate boundary between source positions that are multiple-imaged and those that are single-imaged. Also, strong lensing occurs to sources closer than about θ_E to the optic axis, whereas weak lensing takes place in sources located well outside the Einstein ring. By comparing equations (1.12) and (1.14) it is seen that the mean surface mass density inside the Einstein ring equals Σ_{crit}.

1.3 Mass estimations in weak gravitational lensing

Gravitational lensing is currently the most direct method to determine the entire mass distribution of a galaxy cluster. Due to its ubiquitousness, weak lensing yields moderate resolution maps of projected mass over wide areas,

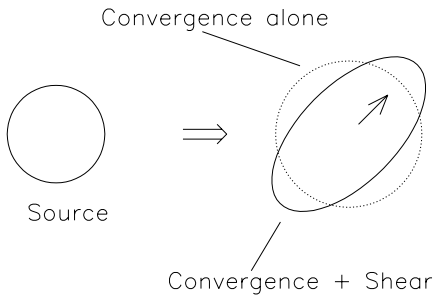

Figure 1.5: The effects of convergence and shear on a circular image. Convergence leads to magnification of the source, whilst shear causes an angular deformation on the image.

whilst strong lensing provides high mass resolution near the source image positions.

Clusters of galaxies are massive, and this large mass causes them to bend light from all background objects. This is seen as distortions in the images of thousands of distant galaxies. The gravitational surface potential of the lens, ϕ, is defined as a two-dimensional Newtonian potential from which the lens equation (1.9) can be derived. The distortions are characterised by this surface potential, which again can be described by two factors; convergence, κ, and shear, γ. Convergence will lead to an isotropic magnification of the source, causing the image of the source to retain its shape but with a larger size. Shear causes an angular deformation on the image without changing its volume, the magnitude of the shear given by $\gamma = (\gamma_1^2 + \gamma_2^2)^{1/2}$. The two components of γ, $\gamma_{1,2}$, are defined in equations (1.19) and (1.20). With both κ and γ present, a circular source will become an elliptical image, as displayed in Figure 1.5. If this source has a radius of unity, the major and minor axis of its image is, respectively,

$$a = (1 - \kappa - \gamma)^{-1}, \quad b = (1 - \kappa + \gamma)^{-1} , \tag{1.15}$$

and the magnification, μ, is given by

$$\mu = \frac{1}{(1-\kappa)^2 - \gamma^2} . \tag{1.16}$$

The relation between ϕ and κ is

$$\nabla_\theta^2 \phi = 2\kappa , \tag{1.17}$$

where the Laplacian of ϕ is taken with respect to θ. κ is therefore given by[5]

$$\kappa(\theta) = \frac{1}{2}\left(\frac{\partial^2\phi(\theta)}{\partial\theta_1^2} + \frac{\partial^2\phi(\theta)}{\partial\theta_2^2}\right) . \tag{1.18}$$

The components of the shear are given as two additional linear combinations of the second derivative of ϕ by

$$\gamma_1(\theta) = \frac{1}{2}\left(\frac{\partial^2\phi(\theta)}{\partial\theta_1^2} - \frac{\partial^2\phi(\theta)}{\partial\theta_2^2}\right) \tag{1.19}$$

$$\gamma_2(\theta) = \frac{\partial^2\phi(\theta)}{\partial\theta_1\partial\theta_2} . \tag{1.20}$$

The Kaiser & Squires method

Kaiser & Squires (1993) have developed a method using weak lensing measurements to quantitatively reconstruct the surface mass distribution of a cluster. From the deduction of equation (1.17) it is clear that κ can be given in terms of the two-dimensional surface mass density, Σ, by

$$\kappa(\theta) = \frac{\Sigma(\theta)}{\Sigma_{crit}} , \tag{1.21}$$

where Σ_{crit} is the critical surface mass density. κ is therefore also defined as the dimensionless surface mass density of a galaxy cluster. The surface mass distribution of the lensing cluster can hence be obtained from $\Sigma(\theta) = \kappa(\theta)\Sigma_{crit}$.

The Kaiser & Squires method is based on the fact that both κ and $\gamma_{1,2}$ are linear combinations of the second derivative of ϕ. Fourier transforming equations (1.18) - (1.20) yields expressions of $\tilde{\kappa}$, $\tilde{\gamma_1}$, and $\tilde{\gamma_2}$. It is then possible to express $\tilde{\kappa}$ as a function $\tilde{\gamma_1}$ and $\tilde{\gamma_2}$, and inverse Fourier transforming this function leads to an estimate of κ. All that is required to estimate the surface mass density of a galaxy cluster is an estimate of the shear. This estimate is provided by the Kaiser & Squires method, that builds upon the fact that the shear field, $\gamma(\theta)$, can be measured[6]. This is done by first defining the ellipticity of an image by

$$\epsilon = \epsilon_1 + \mathrm{i}\epsilon_2 = \frac{1-r}{1+r}\mathrm{e}^{2\mathrm{i}\zeta} , \quad r \equiv \frac{b}{a} , \tag{1.22}$$

where ζ is the position angle of the ellipse and a and b are its major and minor axes, respectively. Using equations (1.15) an expression for the average

[5] See section 3.2 for a more detailed deduction on equations (1.18) - (1.20). The presentation done here is only meant as a general introduction to the topic of shear and convergence.

[6] Detailed descriptions about how this is done is found in Kaiser, Squires & Broadhurst (1995).

ellipticity induced by lensing can be deduced as

$$\langle \epsilon \rangle = \left\langle \frac{\gamma}{1-\kappa} \right\rangle \ , \tag{1.23}$$

where the average is taken over a finite area of the sky. In weak lensing $\kappa \ll 1$, which then validates the assumption that the shear is directly given by the ellipticity:

$$\langle \gamma_1(\theta) \rangle \approx \langle \epsilon_1(\theta) \rangle \ , \quad \langle \gamma_2(\theta) \rangle \approx \langle \epsilon_2(\theta) \rangle \ . \tag{1.24}$$

The $\gamma_1(\theta)$, $\gamma_2(\theta)$ fields are hence obtained from measurements of the ellipticity of weak distortions of background galaxy images. It is important that $\langle \epsilon_1(\theta) \rangle$ and $\langle \epsilon_2(\theta) \rangle$ are obtained from an image of reasonable S/N ratio in order to provide reliable measurements with low errors. From the shear field $\kappa(\theta)$ can be derived, which then provides a method of generating a two-dimensional surface mass map displaying $\Sigma(\theta)$.

1.4 Dark matter

It is currently believed that about 85% - 90% of the mass of the universe is made up by dark matter. Because it neither emits nor reflects electromagnetic radiation (such as light) it is not readily visible. However, its presence can explain gravitational anomalies seen in the motion and distribution of galaxies.

In 1933 Zwicky observed the Coma galaxy cluster and derived its total mass by measuring the velocities of individual galaxies in the cluster, assuming that the cluster was in stable equilibrium. He calculated the mean amount of mass per unit luminosity to about $200h^{-1}M_{\odot}/L_{\odot}$, whereas both observation and modelling indicated the stars to have a mean mass-to-light ratio of about $10M_{\odot}/L_{\odot}$. Zwicky therefore concluded that about nine tenth of the mass was dark matter and not possible to detect visually. This conclusion was controversial, mainly because the dynamic state of clusters was not clear. In the 1970's the first imaging X-ray telescopes in space observed that large galaxy clusters contained gas at a temperature of about 10^8 K. Such hot gas requires a large, deep potential well to contain it, thus proving the galaxy clusters to be in stable equilibrium and showing that Zwicky was correct.

As dark matter can only be detected indirectly, gravitational lensing provides a unique method to obtain a deeper understanding of its nature. Dark matter has so far only been detected by its gravitational influence in astronomical observations. There are several studies trying to detect dark matter by direct measurements, but none has succeeded so far.

1.5 Galaxy clusters

Galaxy clusters were first tentatively recognised in the sky surveys of nebulae in the 1800s. At that time neither the size and structure of the Galaxy nor the distinction between various types of nebulae was known. An essential step towards the physical investigation of galaxy clusters came with Hubble's distance scale of the late 1920's. Zwicky's indications about dark matter then gave rise to further investigations, and Abell's constructions of the first Abell cluster catalogue in the 1950's radically changed the studies of large-scale structures.

Galaxy clusters are the largest stable structures in the local universe, forming the densest components of the large-scale structure of the entire universe. The clusters consist of galaxies held together by gravitation, containing from as few as ten to thousands of galaxies. They typically have a diameter of 2 to 10 Mpc. Large groupings of galaxy clusters are called superclusters, which again appears in filaments, the largest known structures of the universe. The filaments are thread-like structures with a typical length of 70 to 150 Mpc.

Clusters of galaxies can roughly be divided into regular and irregular clusters. Regular clusters have a strong concentration of galaxies towards the centre, and are fairly symmetrical spherical systems. The vast majority of their galaxies are elliptical or lenticular (SO) galaxies. Irregular clusters are more diffuse and less structured. They contain all types of galaxies, with substantial numbers of spiral galaxies.

1.5.1 Abell clusters

The most conspicuous groupings of galaxies are called Abell clusters and were identified by George Abell. The first photographic survey was provided by the Palomar Sky Survey, made with the Schmidt telescope at Mount Palomar in the 1950's. Abell used this database to construct a catalogue containing 2712 of the richest such groupings in the northern hemisphere, describing the process in his 1958 paper (Abell 1958). The catalogue was later extended to the southern hemisphere by Abell, Corwin and Olowin (Abell et al. 1989), and the total sample consists of 4076 galaxy clusters.

The Abell catalogue formed the basis for the first quantitative studies of galaxy clusters, and revolutionised the study of large-scale structure in the universe. Abell took great care when classifying the clusters, and the fact that his catalogue still is the fundamental low-redshift sample proves this. The process of defining galaxy clusters from wide-field survey plates has been repeated in recent years using automatic plate-scanning machines. Results from this process showed that the subjective factor in Abell's visual selection is very small. A very large fraction of the rich clusters in the Abell catalogue represent compact, localised peaks in the spatial distribution of

galaxies. Most of the clusters have redshifts less than 0.2, and they are all held together by gravitation. From the resulting Abell catalogue Abell drew the important conclusion that galaxy clusters are not randomly distributed.

1.6 The clusters Abell 1351 and Abell 1995

The galaxy clusters Abell 1351 and Abell 1995 were observed with the Canada-France-Hawaii Telescope (`CFHT`) using the wide-field CCD mosaic camera `CFH12K` on the 4 nights of $7^{th} - 11^{th}$ of May 2000 by Håkon Dahle. Nine exposures, each of 600s, were obtained in the I band[7], giving a total exposure time of 5400s for each galaxy cluster. Three of the Abell 1351 exposures were obtained under significantly worse seeing conditions (about $1\farcs3$) than the other six (about $0\farcs8$). As gravitational lensing analysis in general needs seeing conditions around $1''$ (no larger than $1\farcs2$), and because the six "good seeing exposures" were sufficient for analysis purposes, the three "bad seeing exposures" were excluded from this study.

The weather conditions while observing were very good, with photometric sky most of the time. There was some moon in the beginning of the nights, but as the observations were obtained in the I band, this did not have a significant influence on the data. The good weather conditions and the excellent seeing resulted in exposures containing on average high signal-to-noise (S/N) values. This is a huge advantage when dealing with weak gravitational lensing as it is the faintest objects (lowest S/N) that are of interest.

There was a great advantage in having the observations already obtained when starting a Master's degree, as no delays were to be expected due to bad observing conditions. There exists no previous wide-field studies on the galaxy clusters Abell 1351 and Abell 1995 using gravitational lensing. Looking further into these data was therefore very interesting, precisely because it was possible to investigate the mass distribution to further radii than done earlier. Dahle et al. (2002) describes a study of 38 clusters of galaxies including Abell 1351 and Abell 1995 measuring the mass distribution using weak gravitational lensing. This study goes out to radii of about $18\farcm7$, covering an area of 350 square arcminutes, whilst the data in this thesis are obtained to outermost radii of $41\farcm2$, covering an area of 1133 square minutes. With an area three times larger and a radius twice as large in the east-west direction this thesis' analysis will put considerably more accurate constraints on the density profiles of the clusters. Since Dahle et al. establish Abell 1351 and Abell 1995 to be gravitational lenses, this gives grounds for further examination of the clusters.

From the morphology of the X-ray emitting gas in the galaxy cluster, Abell 1995 is classified as a regular cluster (Pedersen & Dahle, 2006). It is

[7] using the Cousins I band filter

	Abell 1351	Abell 1995
Right Ascension[a]	11h 42m 30.7s	14h 52m 50.4s
Declination[a]	$+58°32'21''$	$+58°02'48''$
Redshift[a] $[z]$	0.322400	0.318600
Heliocentric radial velocity[a] [km s^{-1}]	96,653	95,514
$\mathbf{L}_{0.1-2.4}{}^{b,e}$ $[10^{44}h_{50}^{-2}$erg s$^{-1}]$	8.31	13.42
$\mathbf{L}_{0.1-2.4}{}^{c,f}$ $[10^{44}h_{50}^{-2}$erg s$^{-1}]$	13.7	16.5
$\mathbf{D}_d{}^{d,e}$ $[h^{-1}$Mpc]	782	775
$\mathbf{D}_d{}^{d,f}$ $[h^{-1}$Mpc]	894	884

[a] NASA/IPAC Extragalactic Database, http://nedwww.ipac.caltech.edu/index.html

[b] Boehringer et al. 2000

[c] Allen et al. 2003

[d] The Redshift Distance Calculator, http://sa1.star.uclan.ac.uk/~cph/redshift.html

[e] Einstein - de Sitter universe, $\Omega_M = 1, \Omega_\Lambda = 0$

[f] The cosmology model of $\Omega_M = 0.3, \Omega_\Lambda = 0.7$

Table 1.1: Characteristics about the galaxy clusters Abell 1351 and Abell 1995.

assumed to be in dynamical equilibrium. Abell 1351 is by Allen et al. (2003) classified as being a galaxy cluster undergoing a major merger event, based on X-ray data from ROSAT and Chandra. The cluster is probably not in dynamical equilibrium. Table 1.1 lists some characteristics about the galaxy clusters. The Right Ascension (RA), Declination (DEC), redshift (z) and the heliocentric radial velocity are taken from the web pages of NASA/IPAC Extragalactic Database (NED)[8]. The rest-frame X-ray luminosities, $L_{0.1-2.4}$, are found in the articles of Boehringer et al. (2000) and Allen et al. (2003), calculated in the $0.1 - 2.4$ keV energy band. $L_{0.1-2.4}$ are together with the angular diameter distances D_d determined for two different models of the universe; the ΛCDM model of $\Omega_M = 0.3$ and $\Omega_\Lambda = 0.7$, and the Einstein-de Sitter model of $\Omega_M = 1$ and $\Omega_\Lambda = 0$. D_d is calculated using an online "Redshift Distance Calculator"[9].

1.6.1 The fields of Abell 1351 and Abell 1995

Figure 1.6 shows the field of Abell 1351, made from stacking the 6 reduced images[10]. The field of Abell 1995 is shown in Figure 1.7. This image is

[8] http://nedwww.ipac.caltech.edu/index.html

[9] http://sa1.star.uclan.ac.uk/~cph/redshift.html

[10] The image reduction is carried out in Chapter 2 together with the astrometric calibration.

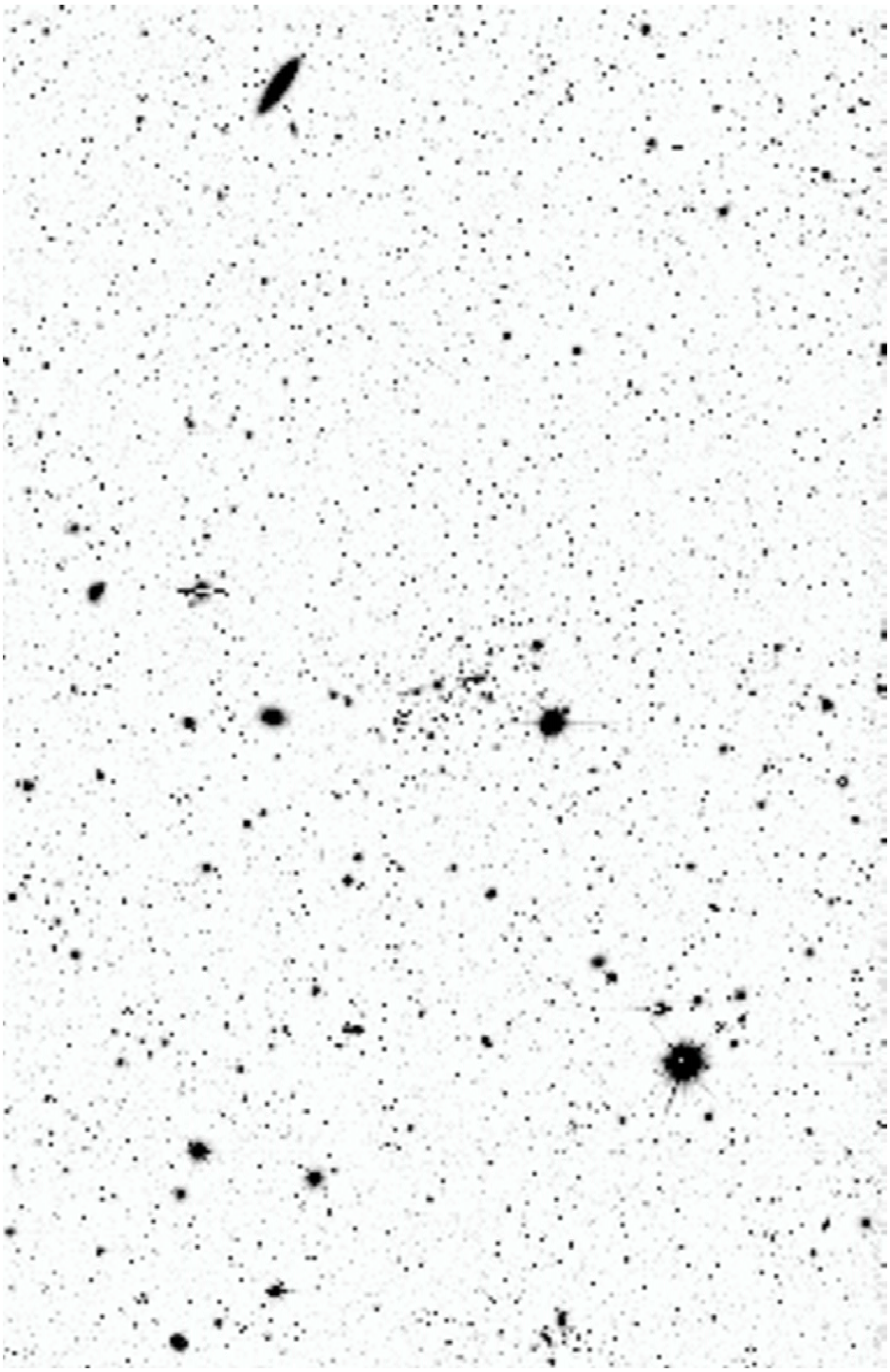

Figure 1.6: The field of Abell 1351. North is up and east to the left in the field that covers $41'.2 \times 27'.5$.

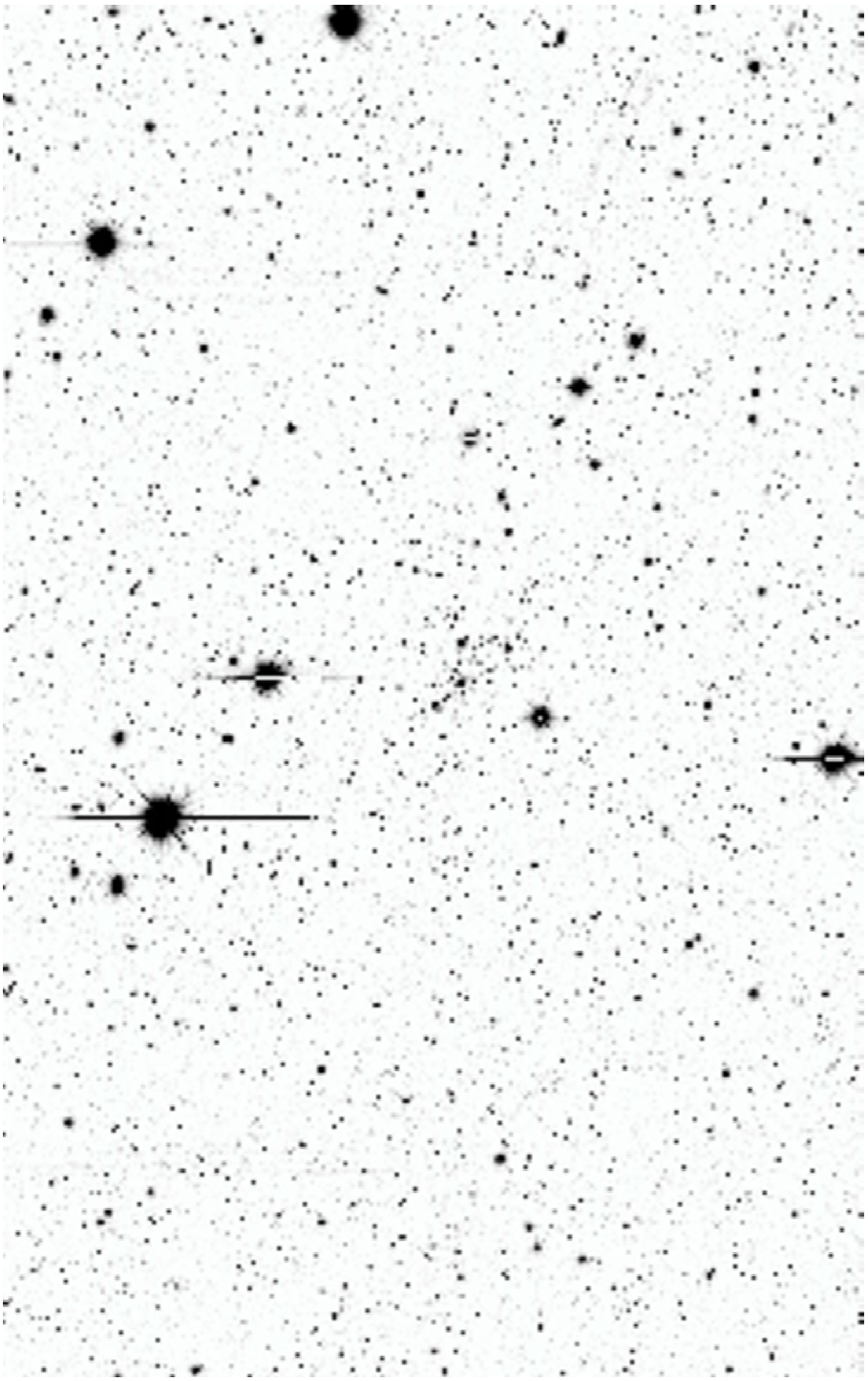

Figure 1.7: The field of Abell 1995. North is up and east to the left in the field that covers $4\farcm2 \times 2\farcm5$.

made from stacking the 9 reduced images of the field. North is up and east to the left in the images, and they cover an area of $41\farcm2 \times 27\farcm5$ each. The field centres are visible in the middle of the images as the galaxy density is higher here, this being more visible in the field of Abell 1351. The number of galaxies detected in the final stacked images is 44,363 for Abell 1351 and 40,461 for Abell 1995.

Chapter 2

Instrumentation, pre-processing, and astrometric calibration

Detecting electromagnetic radiation is the essence of observational astronomy. The search for methods to detect and store as much light as possible makes astronomers continue developing the technology. A telescope greatly enhances the possibilities of seeing distant objects. The more light that is collected, the fainter the objects that can be detected. This is what makes the telescope the most important tool in astronomy.

The invention of photography during the nineteenth century led to a revolution in astronomy. By mounting a photographic plate at the focal point of the telescope and taking long exposures, extremely faint features could be detected. Film has the ability to sum up the intensity of all the photons affecting its emulsion, whereas the eye has no possibility of gathering this information, but rather erases the image several times a second. Using a camera to give deep, high-resolution images made it possible to see faint objects, and with the advent of photography astronomers could now see deeper into the universe than ever before.

Though cameras gave astronomers a way of discovering the universe once more, it is well known that a photographic plate is an inefficient detector of light because it depends on a chemical reaction to produce an image. About 2% of the photons striking the photographic plate trigger this reaction, which means that almost all of the light is lost. Improvements in technology have lead to new methods of detecting light, and now most telescopes are equipped with instruments containing much more efficient detectors called CCDs (charge-coupled devices). Commonly, 80% of the light falling on a CCD is stored. The quantum efficiency (QE) of a CCD is a measurement of how efficiently the CCD detects photons and converts them to useful output. Today's CCDs have very high QEs, and they are also linear

in their response to light in the sense that the output value is linearly related to the number of incoming photons[1]. The CCD is therefore a much more efficient and accurate detector than the photographic plate.

This chapter describes the instruments used, and also looks into the reduction of the data set. This pre-processing is done to remove instrumental signature and improve the signal-to-noise (S/N) in the data before attempting to extract any scientific information. The historical review given in the introduction is based on summaries given in the textbook "Discovering the Universe", Comins and Kaufmann (2003). The facts concerning CCDs and data reduction are found in "Handbook of CCD Astronomy", Howell (2000).

2.1 The Canada-France-Hawaii Telescope and the CFH12K camera

The Canada-France-Hawaii Telescope[2] (`CFHT`) is a 3.6 meter telescope situated on the top of Mauna Kea, Hawaii. The volcano, rising 4,200 meters above the Pacific Ocean, is located on the Big Island of Hawaii and is regarded as one of the best ground based astronomical observing sites in the Northern Hemisphere, with the `CFHT` built on one of the best locations near the summit. The high altitude of the site results in a clearer and dryer atmosphere, a darker sky, and sharper images because of low turbulence in the atmosphere on the top.

The `CFHT` saw first light in 1979 and was originally designed for use with large photographic plates covering four times the area of the full moon on the sky. Ever since the arrival of `CFH12K` in early 1999 the major strength of `CFHT` has been wide-field imaging. The `CFHT` is highly versatile due to its four foci and is very efficient for direct imaging.

The `CFH12K`[3] camera was the largest close-packed CCD mosaic camera in use when it saw first light in January 1999. The camera covers $42\farcm2 \times 28\farcm1$ of the sky with each exposure and its large number of pixels provides a high angular sampling. The image scale at the `CFHT` prime focus is $0\farcs206$/pixel. The camera consists of 12 back-side illuminated CCDs, each consisting of 2048×4096 pixels. The CCDs are made in the MIT Lincoln Laboratories.

2.2 Imaging: The charge-coupled device - the CCD

In 1976 the first astronomical image from a CCD was produced. Today CCDs are used in all major observatories, and one can also find them on many amateur telescopes. Still, the most common use of CCDs today are

[1] See section 2.2 for a more detailed description about QE and linearity.
[2] http://www.cfht.hawaii.edu/HawaiianStarlight/
[3] http://www.cfht.hawaii.edu/Instruments/Imaging/CFH12K/

probably in digital cameras. The CCD is divided into an array of picture elements called *pixels*. Each pixel is a small light-sensitive square made from silicon, with the characteristic that an electric charge builds up in the pixel when light is incident on it. The incoming photons striking the pixel are easily absorbed by the silicon if they possess the correct wavelength. The absorption of photons causes the silicon atom to give up a valence electron and move it into the conduction band. In silicon, the photoelectric effect takes place in the wavelength range near IR - soft X-ray, and outside these limits the CCD appears transparent to incoming photons.

Left alone, the conduction band electrons would recombine back into the valence level within approximately 100 milliseconds. These electrons must therefore be collected and held in place until readout occurs. Each pixel has the ability to collect the valence electrons and keep them in a potential well until the end of the exposure. When the exposure ends and CCD readout begins, the electrons collected during the exposure are now shifted within the device. The total charge of each pixel is shifted along the corresponding column. Since each column in the array is connected in parallel, each pixel shift is mimicked throughout the entire array simultaneously. The charges contained in each row are moved up one row, and the top row, called the output shift register, serves as the transition between active rows on the array and the output of the device. From the output register the charge collected within each pixel is transferred one at a time into the output electronics and measured as a voltage. This voltage is then converted into an output digital number called *ADU* (analog-to-digital units). The process of moving the charges of each CCD row into the output register, shifting each pixel charge within this row and transforming the voltage stored in each pixel into ADUs continues until the entire array of pixels has been read out. This might take up until a few minutes for large-format modern CCD arrays, such as a 2048×2048 CCD.

The gain of the CCD determines how the charge collected in each pixel is transferred into a digital number in the output image. This is set by the output electronics, and is given as the number of electrons needed to produce one ADU step within the Analog-to-digital (A/D) converter. Gain values usually range from $1 - 10$ e^-/ADU, lower values being the most common. Although some CCDs are non-linear over the whole range of data values, most CCDs are linear in their response to incoming photons for nearly all values. *Linearity* here implies there is a simple linear relation between the number of incoming photons (the input value) and the digital number stored in the output image (the output value).

There are three factors that can possibly limit the largest usable output pixel value in a CCD image; A/D saturation, saturation from exceeding a pixel's full well capacity, and non-linearity. A/D saturation appears when the input value exceeds the largest value possible for the CCD to convert into an output number. The input value is hence limited by the number of

bits in the A/D converter, for a 16 bit converter this number corresponds to $2^{16} = 65536$. All CCDs become non-linear at very high input values. There might therefore be situations where the non-linear region starts before any saturation appears in the image, and if the astronomer is unaware of this, he could have a number of non-linear pixels. Non-linear data values can still be used in subsequent scientific analysis, though the non-linearity must be carefully measured and corrected for, making it important to know the linear range of the CCD being used. It is clear that using a non-linear CCD requires deliberate image processing before any data analysis can be carried out, this being the reason that the majority of today's CCDs are linear for most data values.

Quantum efficiency (QE) is a measure of the ability of a CCD to detect photons and turn them into useful output. The QE is defined as the ratio of incoming photons to those actually detected. For over two thirds of their total spectral range QEs of current CCDs are typically 60% or more, and the QE curves typically peak near 90%. Because the absorption of a photon of a specific wavelength depends on the absorption length of silicon[4], the QE of a typical CCD will approximately mirror the photon absorption curve for silicon. All pixels within the same CCD device are assumed to work identically and have equal responses to the same wavelengths. Even though this is true to a certain extent, there will always be some inequality between pixels and this is one of the reasons that make flat-fielding necessary[5]. The other reason for flat-fielding comes from variations in throughput. When observing with a wide-field camera the whole field of view will not receive the same amount of light. Considering the area of the telescope mirror less light hits the edges than the centre, due to the parabolic shape of the mirror, resulting in less light hitting the edges of the detector too. This is not readily visible for a small detector, but can give rise to variations over the field when using a wide-field detector.

The transfer of the total charge from each pixel to the readout of the CCD leads to small losses and additional uncertainties. *The read noise* for the CCD reflects this and is given in terms of electrons collected by the pixel to the final signal upon readout. Read noise consists of two components; the conversion from an analog signal to a digital number and the occurrence of spurious electrons created by the electronics causing unwanted random fluctuations in the output. These two effects add uncertainty to the final output value, and is the basis for calculating the read noise. Thermal noise within the silicon in the CCD will also add electrons (dark current) to the potential well of a pixel. This is why most CCD devices are cooled down to temperatures near $-100°$C.

[4]Absorption length is defined as the distance for which 63% $(1 - \frac{1}{e})$ of the incoming photons will be absorbed (Howell, 2000).

[5]section 2.5

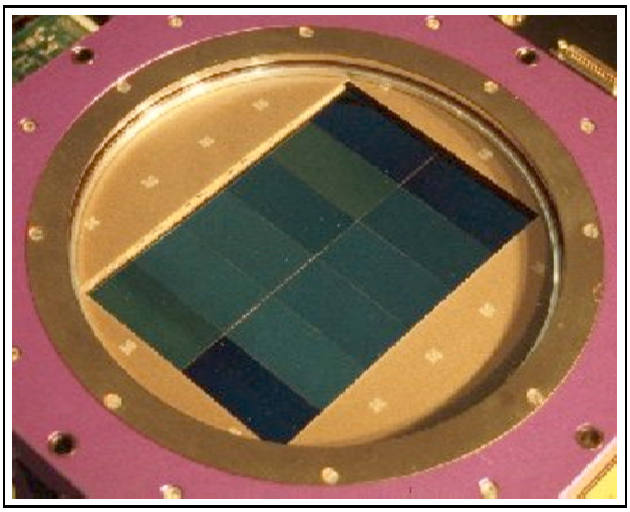

Figure 2.1: The CFH12K CCD mosaic.

2.2.1 The CFH12K CCD

The `CFH12K` CCD mosaic consists of 12 CCDs arranged in a 6×2 mosaic with a physical size of about 21×14 cm. Each CCD contains 2048×4096 pixels, which means that together the 12 chips cover an area of $12,288 \times 8,194$ pixels, that is $42\farcm2 \times 28\farcm1$ arcminutes of the sky at the same time. The CCDs are thinned, backside illuminated and the usable sensitivity ranges from the B band to near infrared. They are cooled down by liquid Nitrogen (LN2) to $-90°$C and have low dark current.

The `CFH12K` chips are made from two different types of material; nine chips are made out of standard epitaxial silicon (EPI) and three chips are made out of resistivity bulk silicon (HiRho). Due to their larger thickness, the HiRho chips have a higher quantum efficiency and produce less fringing[6] than the EPI chips. The QE in the I band (all data used in this thesis were taken using the Cousins I band filter)[7] for each chip is listed in Table 2.2. The three HiRho chips are grouped together in the lower right corner of the mosaic as shown in Table 2.1. This table also shows how the chips are located with respect to each other, with north down and east to the right.

The average gain for the whole mosaic is 1.6 e^-/ADU, with Table 2.2[8] showing the accurate gain for each chip. The dynamic range for the chips

[6]Fringing is the pattern of fringes occurring on a CCD image from observations of monochromatic light. The fringes are caused by interference between light waves reflecting within the CCD, or long wavelength light passing through the array and reflecting back into the array (Howell 2000). Fringing in the I band is discussed further in section 2.5

[7]See section 2.5 for a discussion about the reasons for only observing in this filter.

[8]http://www.cfht.hawaii.edu/Instruments/Imaging/CFH12K/Summary/CFH12K-FocalPlane.html

	EPI				
06	07	08	09	10	11
			HiRho		
00	01	02	03	04	05

Table 2.1: The mosaic layout. The three HiRho chips are located it the lower right corner of the mosaic, the rest of the chips are made from EPI. North is down and east to the right.

CCD	**00**	**01**	**02**	**03**	**04**	**05**	**06**	**07**	**08**	**09**	**10**	**11**
Gain [e/ADU]	1.5	1.5	1.6	1.5	1.3	1.7	1.8	1.7	1.4	1.5	1.8	1.5
Read noise [e]	4.2	3.0	5.4	5.1	10.5	3.4	5.0	5.1	3.4	3.9	3.4	5.2
Linearity [$\times 10^3$ADU]	62	65	51	65	60	65	52	53	65	54	51	65
Relative QE (I band) [%]	57	55	52	72	70	70	52	54	51	53	54	51

Table 2.2: Characteristics for each CCD.

with a high gain is reduced by the 16-bit A/D converter because of saturation occurring when the pixel well is full. The resulting linearity domain can be 51,000 ADU at the lowest, while for those chips with lower gain, the dynamic range is only limited by the digital saturation at 65,535 ADU.

For CCD01, CCD02, and CCD07 the serial charge transfer efficiency (CTE) is 0.99995; this is lower than for the other CCDs that have a CTE of at least 0.99999. CTE is the efficiency value, given as the fraction of charge transferred compared with the charge actually collected. It follows that for these three chips tails may appear on saturated objects, though for non-saturated objects very little flux is lost. The effect from this lower CTE on the image quality is therefore minor. The point spread function (PSF) peak displacement is limited to 0.1-0.2 pixels by the `CFH12K` spatial sampling of $0\farcs2$/pixel. A CTE of 0.99995 will "shift" the PSF a maximum of $0\farcs04$, but as this is only a fraction of one pixel the displacement does not create a problem.

With a fast beam of f/4.2[9] and the large surface of the `CFH12K` mosaic the depth of field is critical. For $0\farcs4$ seeing the depth of field at the `CFHT` prime

[9]The focal ratio, obtained by dividing the focal length of the mirror by its diameter.

Pixel size	15 micron square pixels
Scale at prime focus (f/4)	$0\farcs206$/pixel
Field size	$42\farcm2 \times 28\farcm1$
Readout time	58 sec
Digital saturation	65,535 ADU

Table 2.3: CFH12K data.

Central wavelength	822 nm
Cut on wavelength at 50%	725 nm
Cut off wavelength at 50%	930 nm
Transmission (average)	80%
Bandwidth	205 nm

Table 2.4: Filter characteristics for the Cousins I band filter.

focus is 60 microns, and achieving this flatness was important in making the focal plane structure. Individually the chips are flat within 20 microns, and a combined flatness below 100 microns is measured. Across the field the typical variation in image quality is less than $0\farcs1$ for a seeing of $0\farcs5$.

The `CFH12K` has very good cosmetic properties. The instrument web page claims that the mosaic has a total of 200 bad columns, most of them on CCD05. However, while reducing the data more useless columns were found on CCD00. This resulted in it being necessary to mask out 219 more columns, leaving them disregarded by the analysis software for the rest of the analysis[10]. These 219 bad columns were all next to each other, covering over half the size of the chip in Y direction. The CCD06, 08, 09, 10, and 11 are free of bad columns.

The chips are aligned with gaps from 28 to 43 pixels between them, with an average of 38 pixels in east-west direction (X) and 33 pixels in north-south direction (Y). In arcseconds this corresponds to $7\farcs8$ east-west and $6\farcs8$ north-south. The relative angles between the chips range from $-0.3°$ to $0.3°$.

More detector data are found in Table 2.3 and characteristics for the Cousins I band filter are found in Table 2.4.

2.3 IMCAT

The image reduction and lensing analysis in this thesis are performed using the `IMCAT` software package. `IMCAT` is developed by Nick Kaiser[11]. It is a tool specially designed for weak lensing purposes, and is optimised for shape

[10] section 2.3

[11] kaiser@hawaii.edu, http://www.ifa.hawaii.edu/~kaiser/

measurements of faint galaxies. Due to the intrinsic ellipticity present in background galaxies, precise measurements of object shapes are crucial in obtaining accurate weak lensing results.

IMCAT processes both FITS files and object catalogues. General operations can be carried out on the FITS files, such as image subtraction and division. This is useful in bias removal and flat-fielding (sections 2.4 and 2.5). The FITS files can also be combined to obtain a median frame free from noise and objects (section 2.4), or stacked to improve the S/N quality (section 2.9). Catalogues can be both combined or compared, yielding a possibility to find mapping parameters between two catalogues (section 2.8). IMCAT provides a method of extracting faint objects from a catalogue[12], making it possible to carry out shear measurements on solely these lensed background objects. The software uses plotcat[13] in visualising catalogues, and hence provides a method to extract or reject objects visually.

IMCAT can generate FITS files from object catalogues, or create a catalogue based on object detections in a FITS file. When creating such object catalogue, the coordinates and characteristics of each object are detected/calculated and stored. Finally it can plot objects from a catalogue on top of a FITS file, as done in Figure 2.9.

To make IMCAT disregard corrupt data such as bad pixels and columns, these are given the MAGIC value, this being the most negative number expressible in the pixel format used. The IMCAT software functions then test for this value during processing and neglect the pixel if MAGIC, letting the MAGIC pixels remain MAGIC in the output.

IMCAT is used in all image processing and lensing analysis throughout this thesis. Appendix C gives a detailed introduction to the software.

2.4 Bias and overscan

For each image taken, the CCD electronics are set up to provide a positive offset value called *the bias level*. This is done in order to avoid negative counts in the output image. Calibration measurements of the bias level and its uncertainty are usually made using one or both of the following two processes; overscan regions produced with every readout of a CCD frame, or use of bias frames. *Bias frames* are made by taking exposures of 0.000 seconds. The shutter remains closed and the image is just a readout of the unexposed CCD. This way the read noise level of the CCD is determined and a median bias frame[14] can then be subtracted from the images in order

[12] or objects of any S/N

[13] section C.1

[14] The median bias frame should be made as the median of 10 or more bias frames in order to capture all the statistical variations. Due to statistical rejection when combining, the median bias frame will also be free from cosmic rays, read noise variations, and random fluctuations that will appear in a single bias frame.

to create a bias-corrected image.

The method of *overscan regions* can be used together with or instead of using bias frames. In this process overscan strips are added to and stored with every frame during readout. The overscan strips are numbers of rows or columns of pseudo-pixels produced by sending additional clock cycles to the CCD output electronics. The mean value of the overscan pixels is then determined and subtracted from each pixel within the frame to create an image free from additional bias values.

Both methods should be applied when observing with a CCD having a two-dimensional structure in the bias level and in addition suffers from a non-stable bias level. As the bias level varies throughout the night the median of the overscan stripes must be removed from all images first, including the bias frames. These bias frames can then be removed from the images to remove the bias structure completely. Removing the bias level from the images is the first step in the image reduction process.

As the bias frames represent any two-dimensional structure that might exist in the CCD bias level they provide more information than overscan regions. The bias structure of the CCD may contain some two-dimensional patterns. However, as these usually are of low level and stable with time they are often considered being of low importance and the mean of the overscan strips is used for calibration instead.

Dark frames are also exposures taken with the shutter closed, but for some time period that is usually equal to the exposure time for the object images. These frames measure the dark current[15] in the CCD, but as the CCD is usually cooled with LN2 they reach temperatures in which the dark current is essentially negligible.

The process with overscan strips was used for bias removal in this thesis. The median bias value in each image frame was measured and then subtracted from the image. Then the overscan region was cut off before further image reduction was carried out. This method was sufficient because the bias level of the `CFH12K` chips has no significant two-dimensional variance.

2.5 Flat-field images

A *flat-field image* is used in calibration to make up for the slightly different gain or QE value of each pixel in the CCD when compared to its neighbours, and also to correct for large scale throughput variations[16]. To flatten the pixels' relative response to the incoming light, the object frames are divided by a flat-field frame. The ideal flat-field image would be an exposure with uniform illumination of every pixel in order to obtain the internal variations of the pixels within the CCD, preferably by a light source that has a similar spectral

[15] Dark current is the same as thermal noise.

[16] section 2.2

energy distribution to that of the object images. The number of counts in a flat-field exposure should be slightly less than half the amount that leads to saturation. Also, for each filter used for the science exposures a new flat-field image should be made, this is due to the wavelength-dependence of the pixel response to incoming light.

Before being used in calibration the flat-field image needs to be normalised to an average value of 1. This means that a pixel with a normalised value less than 1 have a smaller value than it would have had if all the pixels had reacted in the same way. By dividing the object image by the flat-field image the corresponding pixel value in the object frame will increase and the pixel variations will be evened out.

There are several ways of obtaining a flat-field image, all of which involve a bright light source giving a CCD calibration image of high signal-to-noise ratio. One way to acquire a flat-field image is by taking *dome flats*. This is done by illuminating the telescope dome from the inside and taking short exposures as not to saturate the CCD. The flats are then averaged together to form a master flat-field image to be used for calibration of the CCD.

By taking exposures during twilight in the evening or in the morning *sky flats* are obtained. The sky flats often give better results than dome flats when averaged into a master flat-field image, and are therefore preferred to dome flats by many astronomers. The reason for this is that the dome is difficult to illuminate uniformly, and with the sky being quite smoothly lit during twilight all the pixels in the CCD are more likely to receive the same amount of light in a sky flat. On the other hand, a problem with sky flats would arise from bright stars being visible in the image. These stars can, however, be removed from the master flat-field image by dithering between exposures and using the median rather than the average value of each pixel. The advantage of dome flats, though, is that they can always be obtained, even during daytime. For both methods five to ten flats from each filter should be obtained in order to get the master flat-field image of the quality required for proper image reduction.

One last method is to not use any specific flat-field frames but rather all the object frames to obtain the master flat-field image. For each exposure the telescope is slightly displaced each time. This dithering is done in order to avoid the same region of the sky falling onto a pixel more than once, and hence avoid having important data fall on bad pixels in all the images. It also means that a star will not be in the same place in any of the images (when the dithering is done properly). By using the median to make a combined image, it is possible to obtain an image frame free from stars and galaxies, and this can then be used as a master sky flat. A problem with using this method is that it requires long exposure times to get the needed signal-to-noise ratio. It also requires multiple exposures with spatial offset to be able to remove the stars when combining images into the master flat. An advantage of using this type of sky flat is, however, the better colour match

from the dark night sky with that of the object frames. In addition, the fringing that usually occurs in narrow-band science images will also occur in this science flat and will then be removed during the flat-fielding process. As opposed to the dark night sky that is dominated by emission lines, the reflected sunlight dominating the twilight sky has a continuum spectrum and the fringing will therefore not appear in the twilight flats. The fringing causes undesired light to be imaged onto the CCD. This extra light increases the apparent background and decreases the resulting S/N. Using science flats hence saves a lot of difficult calibration that would otherwise have been necessary.

Although the main purpose of flat-fielding is to get rid of pixel variations in the CCD, the process will also compensate for possible dust specks present on the dewar window or the filter. The dust specks (if any) are visible as darker "doughnuts" since they are not on the CCD surface and therefore out of focus.

Flat-fielding the data in this thesis was done with the use of a master sky flat made from averaging object frames. There were a satisfactory number of object images to be used for this purpose[17], all well displaced from each other, and the exposure time of 600 seconds was sufficient to gain the amount of counts required in a flat-field image. Only 8 twilight flats were obtained[18] during the 4 night run. To be able to make a master flat of the desired quality more than 8 twilight flats would be needed, which means that the method chosen gave the best result. Also, when using this type of master flat, the fringing that appears in the science images is removed better than by any other method. The more object frames that are averaged into a master sky flat, the better the quality of this flat. To obtain a master flat of highest possible quality, it was convenient to obtain images in the band used by the other programs sharing the run. As these programs observed mostly using the Cousins I band filter, this was the natural choice of band. Also, as the moon was present in the beginning of the nights, the I band minimises the effects of the moonlight compared to narrower filters.

The spectral regime of the I band contains strong narrow emission lines, this being the reason for the large amount of fringing that is usually seen in I band exposures. The night sky emission lines present in Earth's upper atmosphere are mainly attributed to OH transitions in the atmosphere and are powered by sunlight during the day. Since they are forbidden transitions, they have long decay lifetimes and are very narrow spectrally, resulting in fringing patterns in most I band science frames. Fringing was seen in all images used in this thesis, and in order to obtain the highest possible S/N the fringing obviously had to be removed.

[17] 56 exposures obtained with the Cousins I band filter were used to make the master sky flat.

[18] 4 at the beginning of the run and 4 at the end of the run.

The last task in the image reduction was to divide the object exposures by the master sky flat exposure. Examining the object frames after flat-fielding established that the fringing was cleanly removed.

2.6 Background

During exposures the CCD not only collects light from the target of interest, it also receives radiation from the background sky. In addition there will be ADU counts from undetected objects, moonlight, sky-glow and perhaps a torch, together forming a background level in the CCD image that needs to be accounted for. By determining this background level and removing it from the image, only the source flux will remain.

The usual technique in determining the background level is to statistically estimate the mean level per pixel in an annulus placed around the target of interest. This can be done by simply adding all the pixel values inside the annulus and dividing the sum by the number of pixels. By using the median value rather than the mean, this estimation will be more robust, as extreme values like cosmic rays will have less importance in the averaging process.

Using `IMCAT`, the background subtraction was done in a slightly different way whilst processing the data in this thesis. As a galaxy cluster represents several targets of interest rather that one single object, the background level was estimated from the heights of minima of the sky level of the images. The smoothed background estimate was determined as follows; if x_i are the locations of the minima and $f_i = f(x_i)$ are their values, then a pair of images $n(x) = \delta(x - x_i)$ and $f(x) = f_i\delta(x - x_i)$ are created. As $\delta(x)$ is the Dirac function yielding that $\delta(x - x_i) = 0$ for $x \neq x_i$ and one otherwise, this gives that $n(x)$ is an image where the value is one at the locations of the minima end zero elsewhere. $f(x)$ is hence a similar image, except that the values are f_i instead of one at the same locations. Smoothing $n(x)$ and $f(x)$ with a 32 pixel two-dimensional Gaussian results in the images n_s and f_s, n_s representing the density of minima in the image and f_s mapping the same density multiplied with each minimum's respective value. The ratio image f_s/n_s will then be the resulting background image, as this now represents only the values of the minima with no regards to the density. This f_s/n_s image is then subtracted from the object images in order to correct for the background radiation.

At the end of the process the mode of the pixel values in each image is set to zero by simply subtracting its current mode value from the image pixel values. Certain `IMCAT` commands require the mode of the images to be zero, so in order to avoid problems with later executions this task is performed now.

Figure 2.2: The 12 mask files put in a grid according to the relative positions of the chips. The 219 bad columns in CCD00 are clearly visible in the lower left corner.

2.7 Bad pixels and masking

Bad pixels and columns are likely to cause problems during the analysis and lead to incorrect results if they are not dealt with properly during the calibration process. They therefore need to be marked during the reduction process. A simple way of making the processing software disregard these corrupt data is to mask the incorrect pixels by assigning them a certain value. This value is then recognised by the software programs and the pixels are hence neglected. This can be done by making a mask file and applying this to the object images to flag the abnormal pixels.

From its web page[19] it is found that all the chips of the `CFH12K` mosaic together has 200 bad columns that need to be masked out. While examining the object images it was found that another 219 bad columns in the CCD00 also needed to be flagged as unreliable. Ready made mask files were available at Nick Kaiser's web page[20], and as they appeared to be quite good upon examination, these were used to mask out bad pixels in the object frames. The mask files are shown in Figure 2.2.

2.8 Astrometric calibration

As is normal for wide-field images, the pixel/detector coordinates and the sky coordinates do not have a simple relation. It is therefore necessary to

[19] http://www.cfht.hawaii.edu/Instruments/Imaging/CFH12K/
[20] http://www.ifa.hawaii.edu/~kaiser/cfh12k/masks/

perform some kind of mapping from the pixel coordinates onto a planar projection of the sky. This is solved for in a series of steps, all described in this section. The theory behind this section can be found the papers of Kaiser, Squires & Broadhurst (1995; hereafter KSB95), Kaiser et al. (1999) and the manual pages of `IMCAT`.

2.8.1 Orientation of the chips and cataloguing the objects

First of all it was important to make sure all the chips had the same orientation. It was convenient to let north be up and east to the left as this is the orientation of the images obtained from the STScI Digitized Sky Survey used later on in the actual mapping process. The `CFH12K` web page[21] showed the CCDs to have an orientation of north down and east to the right, which made it necessary to rotate all the chips by 180°. By further examination of the data it was discovered that some of the chips were mirrored; CCD06, 07, 08, 09, 10, and 11 were mirrored about the x-axis and CCD02 was mirrored about the y-axis. These chips had to be mirrored back in all exposures to match the true orientation on the sky.

After making sure the orientation of the chips was now correct the objects in the `FITS` files were detected and stored in corresponding catalogues, one for each image frame (using the command `hfindpeaks`). This object detection was done by letting a variety of Mexican hat filters with different radii smooth the image, adding to the catalogue the detection with the highest significance together with parameters like ellipticity and the radius of the smoothing filter, r_g, maximising the detection significance.

Aperture photometry was then carried out and the information added to the respective catalogue. *Digital aperture photometry* aims at estimating the collected source intensity of an object. This is done by placing a software aperture on top of the object and summing all the pixel values within the radius of the aperture (using the command `apphot`), the background level being already removed from the image. Ideally this aperture radius should be big enough to contain nearly all the light from the target object but no light from neighbouring objects. The radii used by `IMCAT` in this process were just 3 times the r_g found and stored by the program performing the object detection. This proved to be a good choice, mainly because the two `IMCAT` programs used here were created for this purpose. In addition to providing the source intensity of the objects, the instrumental magnitudes are also calculated in the process of aperture photometry, together with several other parameters.

[21] http://www.cfht.hawaii.edu/Instruments/Imaging/CFH12K/Summary/CFH12K-FocalPlane.html

2.8.2 The STScI Digitized Sky Survey and the USNO-B1.0 Catalogue

The next step was to match the objects of interest with already identified objects, whose positions on the sky are known. The web page of the Space Telescope Science Institute (STScI)[22] gives access to free downloads of images that together cover the whole sky, these being stored in the *Digitized Sky Survey*[23] (DSS). The DSS contains data from photographic sky survey plates obtained by the Palomar Schmidt and UK Schmidt telescopes. These have been digitised by the Catalogs and Surveys Branch (CASB)[24], mainly to support the Hubble Space Telescope (HST) observing programs, but also to offer the service to the astronomical community. Any part of the sky can be accessed and the images downloaded from the DSS web site in the format of either FITS or GIF. This was done for the targets of interest (Abell 1351 and Abell 1995), and two FITS files containing the field of each galaxy cluster were downloaded and stored.

The *USNO-B1.0 Catalogue*[25] contains 1,042,618,261 objects, all sorted by right ascension and stored in sub-catalogues of $0^\circ.1$ width in declination. The catalogue uses the Tycho-2 Catalogue as its astrometric reference, and it is considered to cover all of the sky with a completeness reaching down to a V band magnitude of 21. The astrometric accuracy at J2000 is considered to be $0''.2$, the photometric accuracy to be 0.3 magnitude in up to five colours and the accuracy for distinguishing stars from non-stellar objects to be 85%. There exists a program made by A. Jaunsen that with some help from IMCAT allows the targets of interest in the USNO-B1.0 Catalogue to be downloaded. This enabled the creation of two separate catalogues, each containing objects in the field of one of the targets.

It was now necessary to establish a connection between the objects in each galaxy cluster's DSS FITS file and those stored in its corresponding USNO-B1.0 Catalogue, that is to say "name" the objects in the DSS image and store them together with the corresponding USNO-B1.0 coordinates in a new catalogue. The first task was therefore to detect the objects in the DSS FITS file. This was done by first making and subtracting a background image, setting the mode to zero, detecting the objects and storing them in a catalogue (from now on called the DSS catalogue), and then performing the same aperture photometry as on the object files described earlier in this section. After having recorded the objects, the celestial coordinates (Right Ascension (RA) and Declination (DEC), epoch J2000) were computed and added to the DSS catalogue. This computation was done with the help of a "world coordinate system" (WCS) definition stored in the DSS FITS image header, relating DSS

[22] http://www.stsci.edu/resources/
[23] http://archive.stsci.edu/dss/index.html
[24] http://www-gsss.stsci.edu/
[25] http://tdc-www.harvard.edu/software/wcstools/wcstools.files.html

pixel indices to celestial coordinates. Also, the software SAOimage DS9[26] automatically decodes this WCS such that the cursor positions appear in (α, δ) rather than pixel coordinates. These celestial coordinates are accurate enough to use in later observations, e.g. for the purpose of making slit masks for multi-slit spectroscopy. In addition the stereographic[27] coordinates were computed from the WCS.

Each `DSS` catalogue was compared with the corresponding `USNO-B1.0` catalogue and the objects present in both catalogues were stored. The transformation between the two coordinates of these matching objects was calculated and a second order polynomial solution for the transformation obtained. This spatial correction was then applied to the objects of the `DSS` catalogue in order to bring the coordinates into agreement with the `USNO-B1.0` system.

2.8.3 Separating stars from galaxies

The objects detected from the `FITS` files now needed to be identified and their correct `USNO-B1.0` coordinates computed. The easiest way of doing this was by first separating the stars from the non-stellar objects and then compare these to stars with known coordinates. The stars are generally brighter, have the smallest positional errors, and are hence easier to recognise and match. It is therefore desirable to use the stars to find some kind of transformation parameters between the two catalogues. These parameters can then be applied to the rest of the objects to find their corresponding `USNO-B1.0` coordinates.

By manually plotting the objects from the catalogues and examining the diagrams it was possible to extract the stars and store them in separate catalogues. All objects from the same exposure were plotted together in a diagram showing r_g vs. instrumental magnitude. The $r_g \approx r_h =$ the half-light radius, that is the radius within which half of the intensity of the object is found. r_g is considered by KSB95 to be a better half-light radius than the usual r_h. Using the surface brightness corrected for the local background, r_g is determined by calculating the growth curve for the integrated light as a function of radius,

$$l(< r) \equiv 2\pi \int \boldsymbol{\theta} f(\boldsymbol{\theta})\, d\boldsymbol{\theta}\ , \tag{2.1}$$

where $f(\boldsymbol{\theta})$ denotes the surface brightness[28] and $\boldsymbol{\theta}$ is the angular coordinate, measured relative to the centre of the object (defined by the centroid of the surface brightness). r_g is then determined within an aperture, together with the luminosity.

[26] used for displaying FITS files

[27] section B.1

[28] The surface brightness is the intensity of a radiating source. It is measured in magnitudes per unit area.

The size-magnitude diagram can be used to distinguish the brighter stars from the galaxies as the stars within certain magnitudes will form a clearly defined locus at a constant half-light radius. Figure 2.3 displays this phenomenon. Brighter stars appear to have larger half-light radius because they are saturated, which means they cannot reliably be used in the mapping process. Fainter stars blend in with small galaxies and it is therefore not possible to clearly separate them, leading to the decision that moderately bright, non-saturated stars are the best ones to utilise for the astrometric calibration.

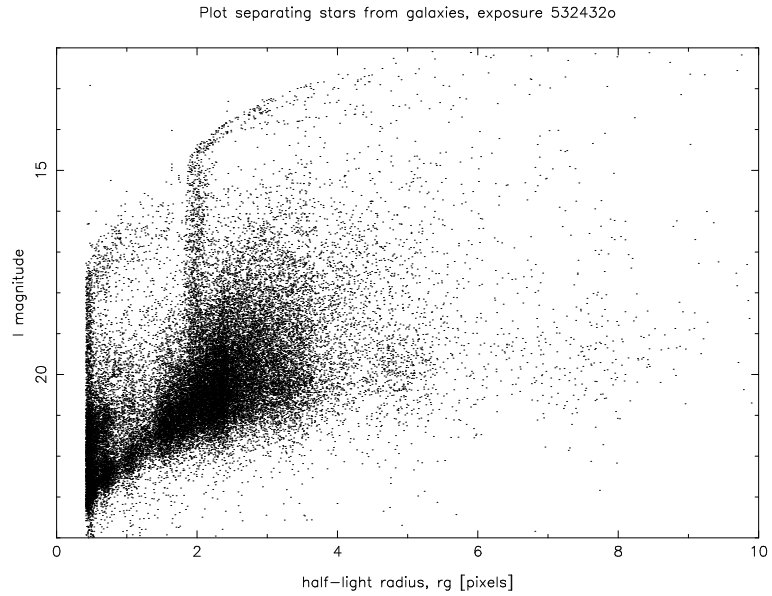

Figure 2.3: This size-magnitude diagram shows objects in the galaxy cluster Abell 1351 obtained in the I band. The diagram clearly shows the vertical stellar locus at a half-light radius of approximately 2 pixels $\approx 0''.4$. The moderately bright stars of interest are located between a magnitude of 15 and 18.5. The saturated stars are clearly seen with magnitude smaller than 15, where r_g suddenly start to increase.

An `IMCAT` program is used to extract the stars by marking them in the r_g-magnitude diagram, yet another criterion is applied in the star selection process. A diagram plotting the polarisation parameters, e_α, is used to get rid of galaxies that might have been collected together with the stars. The polarisation parameters are defined by KSB95 to be

$$e_1 \equiv \frac{Q_{11} - Q_{22}}{Q_{11} + Q_{22}}\,, \quad e_2 \equiv \frac{2Q_{12}}{Q_{11} + Q_{22}}\,, \tag{2.2}$$

where Q_{ij} are weighted quadrupole[29] moments,

$$Q_{ij} \equiv \int W(\boldsymbol{\theta})\theta_i\theta_j f(\boldsymbol{\theta})\, d^2\boldsymbol{\theta}\,, \tag{2.3}$$

with $\boldsymbol{\theta}$ being measured relative to the centre of the object, $f(\boldsymbol{\theta})$ being the surface brightness of the object, and $W(\boldsymbol{\theta})$ a Gaussian distributed weight. The resulting $e_1 - e_2$ plot (see Figure 2.4) is a diagram where the varying degree of polarisation and orientation of an object will decide its placement. A circularly symmetric object will have $e_\alpha = 0$ and will therefore be in the centre of the plot. A vertical ellipsoid will have $e_1 = 0$, $e_2 < 0$ and a horizontal ellipsoid will have $e_1 = 0$, $e_2 > 0$. This also means that the stars are expected to concentrate near the origin, with $e_1 \approx e_2 \approx 0$, as they are considered to be point sources and hence also circular and symmetric. However, because of distortions in the optics, errors whilst guiding, etc, they will not appear exactly in the middle of the diagram. They will also have a certain dispersion due to noise, variations in the PSF as a function of position in the observed field, and the effect from sampling the intensity distribution with a discrete number of pixels. Figure 2.4 shows an example of the polarisation parameter diagram extracted from the galaxy cluster Abell 1351.

This process was carried out on both the object catalogues obtained from the galaxy cluster fields of interest and also on the `DSS` catalogue.

2.8.4 Chip layout errors

The layout of the chips of the `CFH12K` mosaic does not form a completely regular grid, as they are slightly shifted and rotated with respect to each other. In addition, the `CFHT` wide-field corrector introduces a pin-cushion distortion to the telescope. These errors, if not corrected for, will affect the weak lensing analysis and hence lead to incorrect results.

The telescope distortion is a relatively easy error to correct, though if not corrected the effect of a "negative mass" gravitational lens will appear. A more serious potential problem, resulting from errors in the astrometric registration, is a large anisotropy of the summed image PSF. It is therefore desirable to find a method to avoid this anisotropy and get the registration correct. Obtaining a low-order polynomial mapping for each image frame, from pixel coordinates to the rectilinear sky coordinates, is a way of solving this problem. By assuming there is no connection between the exposures concerning the mapping, i.e., by allowing for changes in the telescope and detector system between exposures, both the telescope distortion and the chip layout is accounted for, as well as image distortions arising from filters, atmospheric refraction, thermal expansion, and mechanical strain.

[29] A quadrupole is a system composed of two dipoles of equal but oppositely direct moment.

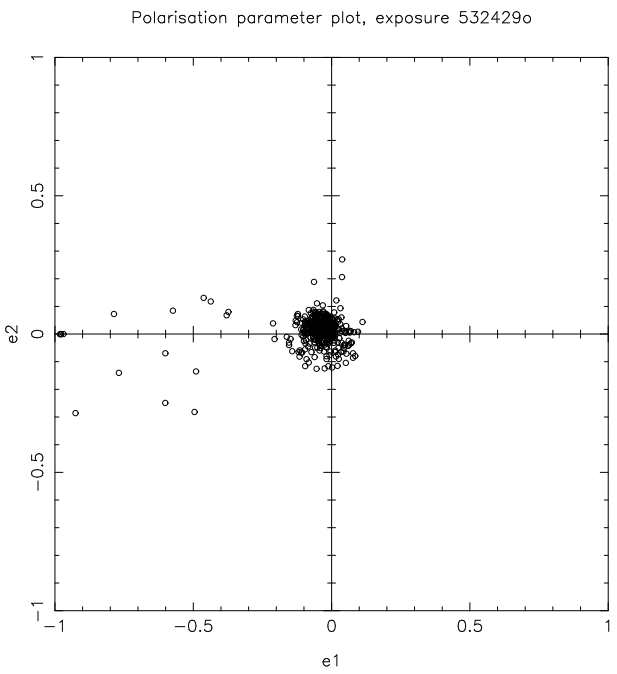

Figure 2.4: This polarisation parameter diagram shows objects from an exposure of the galaxy cluster Abell 1351. The stars are clearly gathering in the middle of the diagram while some objects stay to the left of the centre, indicating that they are non-stellar objects. Perfectly circular stars will have $e_1 = e_2 = 0$.

2.8.5 The reference system

In principle it is possible to determine a set of polynomial mappings using only the CFHT images without any external reference catalogue. By taking one image to define the reference coordinate system the images can be mapped onto each other with very high precision. It is then easy to establish a connection to any other astrometric coordinate system by inspecting the coordinates of a random pair of stars. The problem is, however, that this procedure does not solve for the telescope or atmospheric field distortion, and it also has a tendency of being unstable when further artificial field distortion is introduced. A reasonable solution is therefore to include the external astrometric information already from the beginning of the fitting process. This can be done by using an external catalogue to define the reference coordinate system. A catalogue derived from the Digitized Sky Survey, for example, provides the information needed, including a mapping from pixel coordinates to the "world coordinate system"[30]. However, there is a tendency for the reference catalogue positions to be relatively inaccurate. This makes the process more complicated, in that it is necessary to incorpo-

[30] section 2.8.2

rate this inaccuracy by using weights in the fitting. This means that both the measured position and an estimate of the precision must be included in the input catalogues.

The `IMCAT` software contains several programs designed for the purpose of together solving this problem, using a low order spatial polynomial model. However, to determine a model of this kind the different catalogues must first be matched to a certain level. This is done by establishing a correspondence between the objects in the catalogues in a way that pairs are found whose coordinates are more or less the same to within a small deviation. To make the process more reliable only the stars included in both the reference catalogue and the catalogues to be fitted are used. An algorithm is used to establish this approximate merging between catalogues by determining only the scale (a), rotation (ϕ), and displacement/translation (x_0, y_0) that maps (x_a, y_a) $\rightarrow$ (x_b, y_b)

$$x_b = a(x_a \cos\phi - y_a \sin\phi) + x_0 \quad (2.4)$$

$$y_b = a(a_a \sin\phi + y_a \cos\phi) + y_0 \; . \quad (2.5)$$

The method of determining these parameters is fairly simple. All pairs found from the two source catalogues are stored in a new catalogue and then plotted in a φ - $\log(d)$ diagram, φ being the orientation angle of the pair and d the pair separation. This gives a plot where the two pair catalogues need only be shifted with respect to each other, the shift in φ giving the rotation of the mapping and the shift in $\log(d)$ giving the logarithm of the scale factor.

2.8.6 The low order spatial polynomial model

After establishing this connection between the reference catalogue and the catalogues of interest no more information is needed before proceeding to the next step. Solving for a set of low order spatial polynomials that map pixel coordinates onto the sky is done by repeatedly refining the least squares minimisations. One solution is obtained for each chip. The accurate astrometric solutions for each CCD in the mosaic guarantees that the images can be mapped onto each other with high precision. The artificial distortion that would generally result from a purely internal solution is damped down by the use of an external catalogue.

The mapping from pixel coordinates to sky (`USNO-B1.0`) coordinates is given as a second order polynomial

$$r_p = x_{pi} + \sum_{l=0}^{l=2} \sum_{m=0}^{m=l} a_{ilm} f_{lm}(x_{pi}) + e_{pi} \quad (2.6)$$

where the position of the p'th star on the i'th image is given as x_{pi} and the `USNO-B1.0` coordinate for the p'th star is r_p. Given the mode functions

$$f_{lm}(r) = r_0^{l-m} r_1^m$$

$$= \quad x^{l-m}y^m \tag{2.7}$$

with $r_0 = x$ and $r_1 = y$ as $l_{max} = 2$, the modes are made up by the three quadratic functions x^2, xy, and y^2, the two linear functions x and y, and the constant solution c. The parameter e_{pi} is the observational error, assumed to have an isotropic two-dimensional Gaussian PSF. A lot of research has been done in different projects to determine this error empirically, leading to well tested results of $e_{pi} = 0.03$ pixels for observational data and $e_{p0} = 1$ pixel for the DSS catalogue (H. Dahle, priv. comm.). For my data this corresponds to $e_{pi} \approx 0\farcs006$ and $e_{p0} = 0\farcs206$. For the reference catalogue (the DSS catalogue)

$$r_p = x_{p0} + e_{p0} \ , \tag{2.8}$$

i.e. the index $i = 0$ is assigned to this catalogue. By defining $a_{0lm} = 0$ for this catalogue equation (2.6) can be used for all i.

2.8.7 Labelling the matching stars

The particle identifier, the p-index, is used to label the stars in order to know which objects in the different images are the same star. After calculating the star positions from equation (2.6) using the methods described earlier, an "object count" image is made from a master catalogue containing all the catalogues from the same galaxy cluster. The image size is 2048×4096 pixels and the image covers the whole field in r-coordinates, with each detection of a star being measured as 1 pixel value. From this image a new catalogue is then generated, the "detection catalogue", containing only the stars with more than a certain amount of counts. Whilst the stars are being stored, they are assigned the p-index. This index is then applied when the object catalogues are merged[31] with the detection catalogue, resulting in a new set of catalogues containing only the stars being detected in more than a certain number of images.

2.8.8 Astrometric solution

The astrometric solution contains a set of second order polynomials consisting of star positions, r_p, and mode amplitudes, a_{ilm}, that together minimise the sum of the squared residuals:

$$\chi^2 \quad = \quad \sum_p \sum_i \frac{e_{pi}^2}{\sigma_{pi}^2} \tag{2.9}$$

$$= \quad \sum_p \sum_i \frac{(r_p - x_{pi} - \sum_{l,m} a_{ilm} f_{lm}(x_{pi}))^2}{\sigma_{pi}^2} \ . \tag{2.10}$$

[31] To merge two catalogues means finding pairs of detections whose coordinates are the same to within a certain tolerance.

Because of χ^2 being quadratic in r_p and a_{ilm}, the result is a set of linear equations

$$\partial\chi^2/\partial a_{ilm} = 0\ , \qquad \partial\chi^2/\partial r_p = 0 \tag{2.11}$$

being solved for the mode amplitudes and the star positions. Assuming the position errors rising from variance in the `DSS/USNO-B1.0` coordinates to be Gaussian distributed, this solution corresponds closely to the maximum likelihood solution[32].

After the labelling process the object catalogues are merged, outliers rejected, and an `IMCAT` program run on the resulting catalogue, performing the least squares solution from equation (2.11). In order to obtain an accurate solution, the reference catalogue solution is compared to that obtained by applying the polynomial model to the object catalogue. The objects containing coordinates that differ by more that a certain value from the reference solution are then rejected from their respective catalogues, and the least squares process is repeated.

2.8.9 Refining the solution

Before proceeding, it is necessary to check the quality of the solutions just obtained. This is done by comparing the r-coordinates of the stars in separate exposures after applying the image mapping solution. The results are shown in Figure 2.5 - 2.6. Figure 2.5 shows the residuals in the r-values between a random pair of exposures. Figure 2.6 shows the same residuals, but now plotted as vectors where the object position is the base of the vector and the vector length is magnified 1000 times. Both figures show some inaccuracy, leading to the determination that the least squares solution needs to be refined.

The refinement is done by once again calculating equation (2.6) and then proceeding with the steps described in section 2.8.6 - 2.8.8. Now the image mapping solution obtained in section 2.8.8 is used as the basis in the process as opposed to the inaccurate connection between the reference catalogue and the catalogues of interest used as a basis the first time. A random subset of 40 stars are being held back during the refinement in order to check the quality of the process, and these are not used in the registration solution. Also, the number of counts needed for a star to be registered in the detection catalogue, section 2.8.7, is increased[33] to further improve the quality of the result.

When the process is carried out the second time and a new image mapping solution obtained, this solution is applied to the stars held back during the refinement and the same quality check as above is done with these stars.

[32] section B.5

[33] This number was set to 3 during first processing, and increased to 6 the second time.

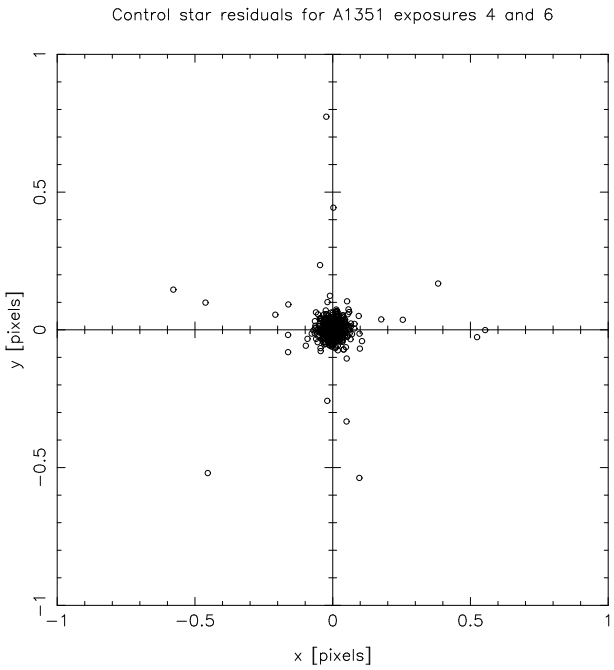

Figure 2.5: Residuals in the image mapping, showing the differences in the r-coordinates between exposures 4 and 6. The unit length is the pixel size; 0.″2060.

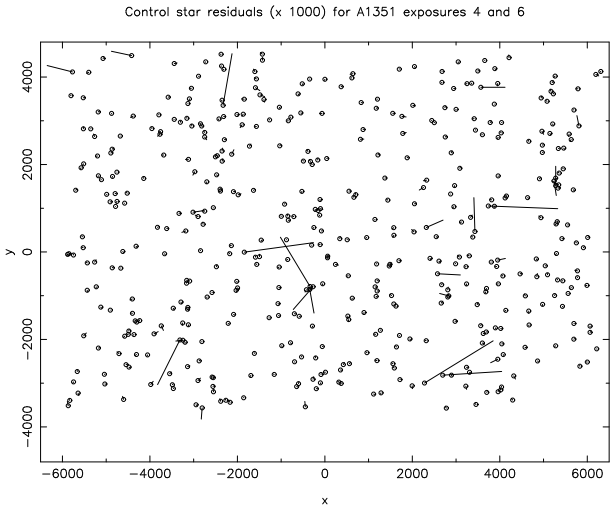

Figure 2.6: Residuals in the image mapping shown as vectors, the length of the vector is enlarged by 1000 and the base of the vector is the object position. This image shows the residuals of exposures 4 and 6.

The resulting residual plots are shown in Figure 2.7 - 2.8 for the same exposures as previous. With the exception of one vector in Figure 2.8 these plots show that the mapping now is very accurate. The residuals show no obvious systematic variations, so it is reasonable to assume that the one out-of-place vector is not a cause for problems with further use of this image mapping solution.

Applying the final transformation coefficients, a_{ilm}, to equation (2.6) gives the mapping from detector coordinates in x_i-space to sky coordinates in r-space (as $r = r(x_i)$). However, when introduced to a target image in r-space it would be necessary to compute the image in x_i-space, yielding that the inverse mapping $x_i = x_i(r)$ would be more useful for later calculations.

To obtain the inverse mapping a grid of points is created, covering a region of x_i-space corresponding to that of the chip in process. The transformation from x_i-coordinates to r-coordinates is then applied to the grid. The x_i, r value pairs calculated from this process are fed to the same `IMCAT` program used to solve for the least squares solution from equation (2.11) in the last section, and the inverse mapping,

$$x_p = r + \sum_{l,m} a'_{ilm} f_{lm}(r) \; , \tag{2.12}$$

is hence solved for, in order to obtain the coefficients a'_{ilm}.

2.9 The master image

By stacking all science images into one, making sure that each object fall onto the same pixels, the final image will contain higher S/N values than each image alone. The weak lensing signal in the faint objects is hence also easier to detect. It is therefore desirable to use only one set of images that cover the entire galaxy cluster field of interest while carrying out the final analysis. This means making separate images that together can be put into one "master `FITS` file" originating from all the exposures used until now. The size of this master image is $12,000 \times 8,000$ pixels, corresponding to a total area of $41\farcm2 \times 27\farcm5$[34] covered by the `CFH12K` images. By creating 24 separate images, each of 2048×2048 pixels, these can be put together in a 6×4 grid to make up the master image (with an overlap of 24 pixels on the edges).

2.9.1 Gain variations and differential extinction

To be able to make this master image, any gain and quantum efficiency variation between the chips and any differential extinction between the exposures must be detected and measured. This can easily be done using `IMCAT` (with the command `fitmagshifts`). After applying the final astrometric solution

[34] slightly smaller area than originally

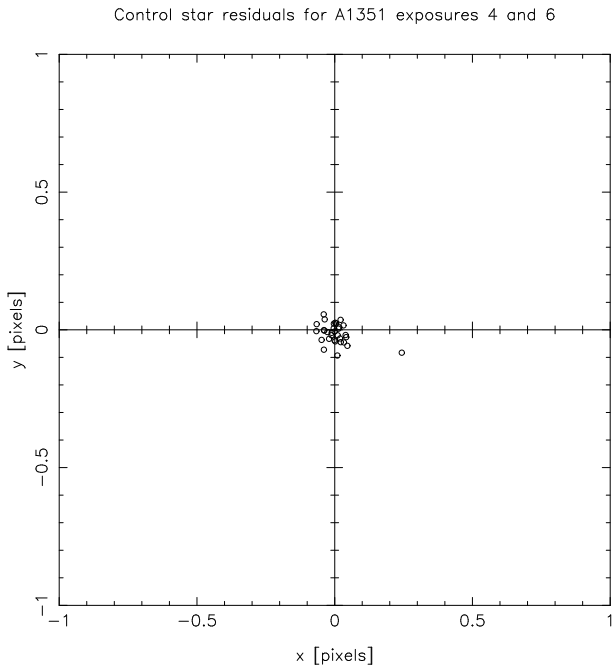

Figure 2.7: The residuals between the r-coordinates of exposures 4 and 6 for a set of control stars. The unit length is the pixel size of $0\farcs2060$.

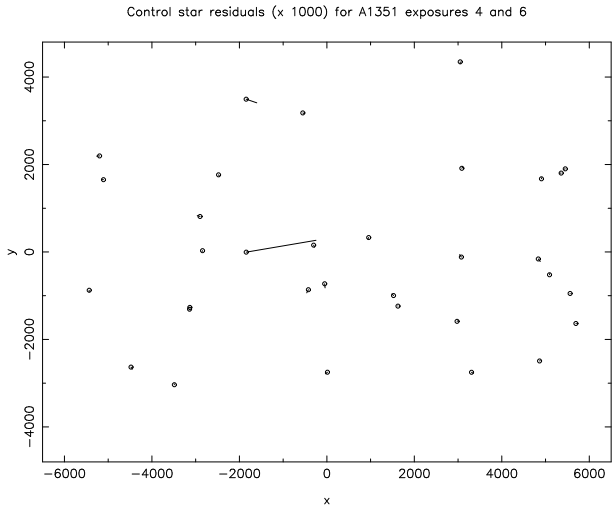

Figure 2.8: Residuals for a set of control stars shown as vectors, the length of the vector is enlarged by 1000 and the base of the vector is the object position. The residuals between exposures 4 and 6 are shown.

to the star catalogues obtained in section 2.8.3, all the chip catalogues from the same exposure were put together into one exposure catalogue. These exposure catalogues were then merged with each other and parameters to correct for gain and QE variations and differential extinctions obtained.

Mathematically the gain and QE variations between chips and differential extinction between exposures are found after modelling the magnitude of a star, m_{ce}, as measured in the c'th chip within the e'th exposure as

$$m_{ce} = m + m_c + m_e \ , \tag{2.13}$$

where m is the true magnitude, m_c is the photometric zero-point offset caused by the gain and QE variation between chips, and m_e is the differential extinction between exposures. Then m_c and m_e are solved for by least squares minimisation, these being measured relative to CCD11 and a chosen reference exposure respectively. As a result two catalogues are produced, one containing the coefficients of the gain and QE variations and the other those of the differential extinctions.

The coefficient catalogues were produced separately for the two galaxy clusters. The two m_c catalogues were then averaged into one catalogue and the same done with the m_e catalogues, letting the average catalogues be used in further calculations. The extinction corrections between the exposures were very small; typically ~ 0.01 magnitudes, whereas the zero-point offsets between the chips were somewhat larger; typically ~ 0.1 magnitudes and with a maximum correction of $\simeq 0.47$ magnitudes.

2.9.2 Combining exposures

The master image is made from combining all available data from the same region of the sky. This means defining a region in the sky (depending on which part of the master image is being processed) and cutting out this area from all the images of relevance, making a stack of images that all cover the same region of the sky. At the same time the gain and QE variations and the differential extinctions are corrected for, leaving only the final combining of the stack images to be performed. After first masking out cosmic rays the images in the same stack are combined into one image, which then represents one of the 24 parts of the master image. The mode of the pixel values in the image is then set to 0.

Combining many different images into one means that the background will not necessarily remain perfectly flat in the combined image. It is therefore important to flatten the background of the master image, and for this task the same procedure as explained in section 2.6 is carried out on the different master image parts. At the end of the process the mode is again set to 0. It is also necessary to make new object catalogues corresponding to these combined images, and the object detection process of section 2.8.1 is used for this purpose. The aperture photometry carried out in the same section is

also applied to the catalogues, and in addition the celestial coordinates are computed and added to FITS headers and object catalogues[35].

2.9.3 Masking by examination

As the number of images is limited to only 24 it is now practicable to examine them more closely and mask out saturated stars and bad regions to prevent wrong information in the object catalogues from interfering with later analysis. Wrong information could in this case be a saturated star detected as several objects, or something registered as objects which is in reality only irregularities in the outermost edges of the master FITS file. These irregularities arise when only a few images make a distribution in the stacking process. Due to dithering between exposures fewer images define the outer regions, which leads to these parts containing lower S/N values than the rest of the image. They also appear more noisy, as cosmic rays and noise will have a bigger influence here than within areas combined from several images. These noisy areas will therefore also contain more false detections as they appear to have many peaks.

The masking is done by manually looking at each image[36] and placing a quadrangle over each area to be masked out. The images are visualised using both the FITS image and the corresponding object catalogue as in Figure 2.9; the objects are taken from the catalogue and plotted on top of the image as small points. One mask file is produced for each image/catalogue, this simply being a new catalogue defining the mask quadrangles in a way that the coordinates of two opposite corners of the quadrangle are stored.

All the smaller catalogues are then merged into one catalogue. With the mask files at hand it is easy to reject the "objects" not corresponding to actual stars or galaxies, and the result is one big object catalogue containing only real objects. Whilst merging, the object coordinates of each image are shifted in order to be placed correctly according to the other parts of the master image. As objects with very low S/N values or very small r_g would rather behave as noise than being of any importance in the analysis, these are rejected in the process. The resulting object catalogue is hence ready to be used in further analysis. The different mask files are also merged into one big file, using the same shifts as previously applied to the object coordinates during the process.

2.10 Closing the reduction phase

The result from the pre-processing discussed in this chapter is 24 final reduced images that can be put together in a 6×4 grid to make up the master

[35] See section 2.8.2 for a description of this world coordinate system.
[36] using plotcat, see section C.1

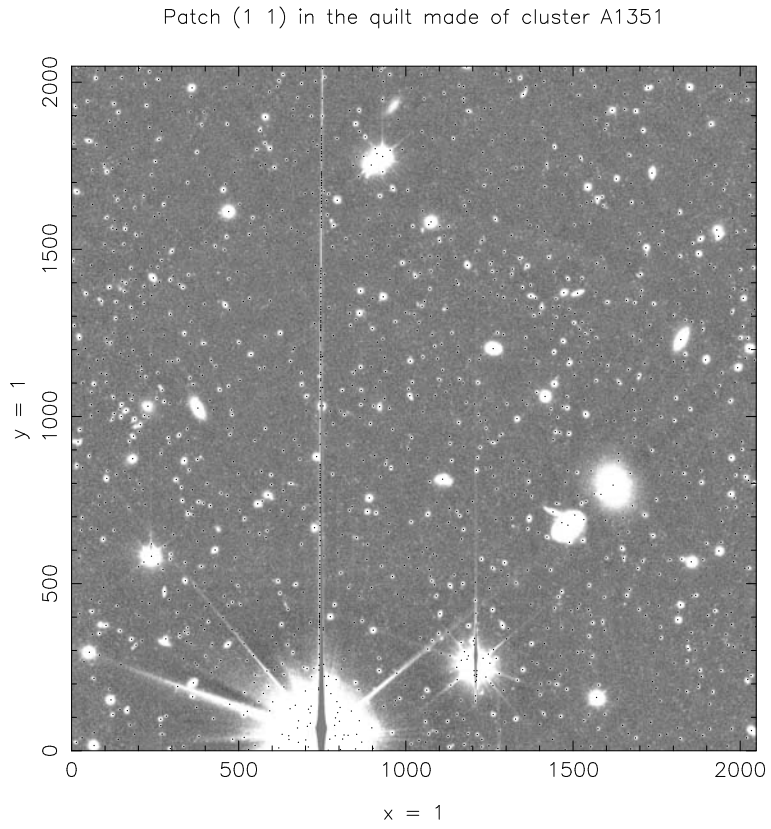

Figure 2.9: Visualising one part of the master FITS image for the purpose of masking saturated stars and bad regions. Every point corresponds to one object detection in the corresponding object catalogue. A saturated star is clearly detected as several objects and these need to be removed from the object catalogue.

FITS image. The master images of Abell 1351 and Abell 1995 are displayed in Figure 1.6 and Figure 1.7, respectively. These master images are carefully refined and different errors corrected for, and are hence accurate enough to be used instantly in the weak lensing analysis to be carried out in the next chapter.

Chapter 3

Weak lensing analysis

Whatever its form and physical state, only the total mass density of a galaxy cluster is relevant in inducing gravitational lensing of the light from background objects. The light rays are deflected by the mass density of the cluster, causing the shapes of the background images to be distorted and sometimes to be also seen as multiple images. Two factors influence the different levels of distortions produced in gravitational lensing; the surface mass density of the cluster, and the alignment of the background objects with the cluster centre of mass and the observer. Big arcs and arclets are seen as the result of *strong lensing*, whereas the *weak lensing* distortions may only be detected as statistically altered object shapes of a group of galaxies.

Good alignment and a surface mass density close to or larger than the critical surface mass density, Σ_{crit}[1], are required to produce giant arcs. This strong lensing can then be used for investigation of the mass distribution in central areas of the galaxy cluster acting as the lens. The condition characterising weak lensing, $\kappa \equiv \Sigma/\Sigma_{crit} \ll 1$, leads to the background objects being only slightly distorted. As opposed to strong lensing, the mass distribution in the galaxy cluster can in this case be traced much further out from the cluster core.

This chapter covers the analysis done on the 24 final reduced images from Chapter 2. By measuring the observed ellipticities of lensed background galaxies, the mass of the lensing galaxy cluster can be estimated using the Kaiser & Squires (1993) method[2]. This estimation of mass is obtained by comparing the observed values of shear and surface mass density with the corresponding values calculated for different models. Least-squares minimisations are used to find the best fit and hence the mass of the galaxy cluster.

The theory behind this chapter is found in Kaiser, Squires & Broadhurst (1995), Kaiser (1995), Squires & Kaiser (1996), Luppino & Kaiser (1997),

[1] See Chapter 1 for a consideration on the topic.
[2] section 1.3

Narayan & Bartelmann (1997), Hoekstra et al. (1998), Clowe et al. (2000), Wright & Brainerd (2000), Dahle et al. (2002), Wold et al. (2002) and Heymans et al. (2005).

3.1 Shear measurements

Identifying weak lensing effects requires measuring the ellipticities of a large number of background galaxies. The main source of noise in weak lensing analysis is the intrinsic distribution of ellipticities amongst these galaxies. This makes weak lensing difficult to measure despite it occurring in every cluster. In order to distinguish between distorted images resulting from a weak lens and the usual distribution of shapes existing in an unlensed galaxy population the ellipticities are examined for a systematic shift. In particular, a tangential alignment of the galaxy shapes around the cluster centre would confirm the existence of a weak lens.

An additional source of error comes from the faint background galaxies being smeared by the seeing Point Spread Function (PSF). The weak shear signal is hence suppressed because this smearing will cause the galaxy images to appear more circular than before the smearing. The PSF may also contain anisotropies, causing it to change as a function of position in the image. The PSF anisotropies caused by the telescope distortion and the chip layout are partially accounted for in the astrometric registration process[3]. This process is accurate enough, so that there are no new anisotropies introduced from registration. The remaining smearing resulting from an anisotropic PSF is corrected for in section 3.1.2.

3.1.1 Object ellipticities

The ellipticities of the objects are measured during the registration process[4] and stored in catalogues corresponding to the different image parts of the master `FITS` image. Their weighted quadrupole moments, Q_{ij}, defined by equation (2.3) give the parametrisation of the objects. Q_{ij} is related to the weighted ellipticity parameters (also called the polarisation parameters), e_α, of a perfect ellipse by

$$e_\alpha \equiv Q_\alpha / T \ , \tag{3.1}$$

with

$$Q_1 \equiv Q_{11} - Q_{22} \ , \quad Q_2 \equiv 2Q_{21} \ , \quad T \equiv Q_{11} + Q_{22} \ . \tag{3.2}$$

Polarisation is referred to as the correlation function of image shear. This function is used in the statistical description of shear appearances in an image to determine whether the shear values are randomly distributed or if

[3] section 2.8.4
[4] section 2.8.1

there is some systematic shift in these values, indicating a gravitational lens. The first-order shift in polarisation (quantified by e_α) caused by the shear, γ, is

$$\delta e_\alpha = P^{sh}_{\alpha\beta}\gamma_\beta \ , \tag{3.3}$$

where the subscripts imply a summation over β,

$$P^{sh}_{\alpha\beta}\gamma_\beta = \sum_{\beta=1}^{2} P^{sh}_{\alpha\beta}\gamma_\beta \ . \tag{3.4}$$

$P^{sh}_{\alpha\beta}$ denotes the *post-seeing shear polarisability tensor*, which measures the response of an image to a shear. Because this response is measured *before* any corrections are made with respect to smearing by the seeing disk, this shear polarisability tensor is denoted as being "post-seeing". The pre-seeing shear polarisability tensor is hence calculated from $P^{sh}_{\alpha\beta}$ (see later this section), and from these calculations the shear can be found.

$P^{sh}_{\alpha\beta}$ is given by

$$P^{sh}_{\alpha\beta} = X^{sh}_{\alpha\beta} - e_\alpha e^{sh}_\beta \tag{3.5}$$

with $X^{sh}_{\alpha\beta}$ and e^{sh}_β defined as

$$X^{sh}_{\alpha\beta} = \frac{1}{Q_{11}+Q_{22}} \times \int \begin{bmatrix} 2W\theta^2 + 2W'(\theta_1^2-\theta_2^2)^2 & 4W'(\theta_1^2-\theta_2^2)\theta_1\theta_2 \\ 4W'(\theta_1^2-\theta_2^2)\theta_1\theta_2 & 2W\theta^2 + 8W'\theta_1^2\theta_2^2 \end{bmatrix} f(\boldsymbol{\theta}) d^2\boldsymbol{\theta} \tag{3.6}$$

and

$$e^{sh}_\alpha = 2e_\alpha + \frac{2}{Q_{11}+Q_{22}} \int \begin{pmatrix} \theta_1^2-\theta_2^2 \\ 2\theta_1\theta_2 \end{pmatrix} W'\theta^2 f(\boldsymbol{\theta}) d^2\boldsymbol{\theta} \ , \tag{3.7}$$

W' denoting the derivative of W with respect to θ^2. The surface brightness function is defined by $f(\boldsymbol{\theta})$, where $\boldsymbol{\theta}$ is the angular coordinate measured relative to the centre of the object, this being defined by the centroid of $f(\boldsymbol{\theta})$. The vector $\boldsymbol{\theta}$ is given by the components θ_1 and θ_2, and $d^2\boldsymbol{\theta} = d\theta_1 d\theta_2$. The length of $\boldsymbol{\theta}$ is defined by $\theta = (\theta_1^2+\theta_2^2)^{1/2}$.

The smearing of the object shapes is caused by an anisotropic PSF. This anisotropy can be be explained by a convolution[5] of a small, normalised, anisotropic PSF, $g(\boldsymbol{\theta})$, with a circularly symmetric seeing disk, and the quadrupole moments will hence change as

$$Q'_{ij} = Q_{ij} + q_{lm}Z_{lmij} \ , \tag{3.8}$$

q being the unweighted quadrupole moments of the PSF

$$q_{lm} \equiv \int \theta_l\theta_m g(\boldsymbol{\theta}) d^2\boldsymbol{\theta} \tag{3.9}$$

[5]See section B.4 for an explanation of the mathematical term convolution.

and Z_{lmij} being given by

$$Z_{lmij} = \frac{1}{2}\int f(\boldsymbol{\theta})\frac{\partial^2[W(\boldsymbol{\theta})\theta_i\theta_j]}{\partial\theta_l\partial\theta_m}d^2\boldsymbol{\theta}\ . \tag{3.10}$$

The change in polarisation caused by an anisotropy in the PSF is given by

$$\delta e_\alpha = P^{sm}_{\alpha\beta}p_\beta\ , \tag{3.11}$$

where p_α represents a measure of the PSF anisotropy,

$$p_\alpha \equiv \begin{pmatrix} q_{11}-q_{22} \\ 2q_{12} \end{pmatrix}\ , \tag{3.12}$$

and $P^{sm}_{\alpha\beta}$ is known as the smear polarisability. $P^{sm}_{\alpha\beta}$ is given by

$$P^{sm}_{\alpha\beta} = X^{sm}_{\alpha\beta} - e_\alpha e^{sm}_\beta \tag{3.13}$$

with

$$X^{sm}_{\alpha\beta} = \frac{1}{Q_{11}+Q_{22}} \times \int \begin{bmatrix} W+2W'\theta^2+W''(\theta_1^2-\theta_2^2)^2 & 2W''(\theta_1^2-\theta_2^2)\theta_1\theta_2 \\ 2W''(\theta_1^2-\theta_2^2)\theta_1\theta_2 & W+2W'\theta^2+4W''\theta_1^2\theta_2^2 \end{bmatrix} f(\boldsymbol{\theta})d^2\boldsymbol{\theta} \tag{3.14}$$

and

$$e^{sm}_\alpha = \frac{1}{Q_{11}+Q_{22}}\int \begin{pmatrix} \theta_1^2-\theta_2^2 \\ 2\theta_1\theta_2 \end{pmatrix}(2W'+W''\theta^2)f(\boldsymbol{\theta})d^2\boldsymbol{\theta}\ . \tag{3.15}$$

Here the prime refers to differentiation with respect to θ^2.

3.1.2 Correcting for the Point Spread Function

Ignoring the effects of photon counting noise, it is possible to express the observed ellipticity of a galaxy as

$$e^{obs}_\alpha = e^s_\alpha + P^\gamma_{\alpha\beta}\gamma_\beta + P^{sm}_{\alpha\beta}p_\beta \tag{3.16}$$

where e^s_α is the intrinsic ellipticity of the galaxy, the second term denotes the shift in ellipticity caused by the gravitational shear, γ_β, and the third term represents the smearing of the galaxy image from the anisotropic PSF (Luppino & Kaiser 1997)[6]. These last two terms will be examined more closely in the following subsections.

Also present in equation (3.16) are the pre-seeing *shear polarisability tensor*, $P^\gamma_{\alpha\beta}$, and the *smear polarisability tensor*, $P^{sm}_{\alpha\beta}$[7]. $P^{sm}_{\alpha\beta}$, e^{obs}_α, and the centroid of the object are easily calculated by `IMCAT` and added to the respective object catalogues (using the command `getshapes`), together with the post-seeing shear polarisability tensor, $P^{sh}_{\alpha\beta}$, given by equation (3.5).

[6] See Appendix A for a deduction of equation (3.16).

[7] Note that these are not actually tensors but rather quasi-tensors (Kaiser, Squires & Broadhurst 1995).

The Point Spread Function anisotropy

The change in polarisation resulting from the PSF anisotropy, δe_α, is given by equation (3.11). To be able to calculate this change in polarisation, p_β has to be determined. One way of obtaining this component is to apply equation (3.16) to stellar objects. The stars are intrinsically circular ($e^s_\alpha = 0$), and as they are foreground objects they are not lensed by the galaxy cluster ($\gamma_\beta = 0$). p_β is hence left as the only unknown parameter in the equation. This p_β is the same for all objects because the changes in their shapes are applied *after* the light hits Earth's atmosphere. These "post-atmospheric" distortions therefore need to be removed from the galaxy shapes in order to obtain the correct weak-lensing measurements. Since $P^{sm}_{\alpha\beta}$ and e^{obs}_α are already calculated for all the objects, it is easy to calculate p_β for all the stars. This value is hence applied to equation (3.11) and the ellipticities of the galaxies are corrected by $-\delta e_\alpha$ (using the `IMCAT` commands `efit` and `ecorrect` respectively). The galaxies now have the polarisation values they would have had if the PSF were perfectly isotropic. The calculations done here all assume noise-free data. However, the use of bright stars in the process makes the problem of photon counting noise negligible.

Due to the PSF changing as a function of position across the field, the ellipticities of the stars were fitted to a sixth order polynomial model. This model is derived from a Taylor series expansion[8] with the coefficients being determined by least-squares minimisations. The position of each galaxy is then used as a basis for calculating the ellipticity of the PSF at that location, and thus the correction to the galaxy's ellipticity can be calculated. For this correction procedure to work, it is crucial that all fluctuations of the PSF anisotropy across the field are sampled. This is only possible with a sufficient amount of stars involved in the process. For the galaxy clusters Abell 1351 and Abell 1995 analysed in this thesis, 410 and 530 stars were used from each field, respectively. This was more than sufficient, as polynomials of any order up until the limit of the `IMCAT` program `efit` used for the fitting process (the sixth order) could be applied.

As the offsets between the exposures (used in making the master `FITS` image) were not large but merely dithering, the same object will not land on different chips in different exposures. The PSF will hence not change in one object as a result of PSF anisotropy across the mosaic, leading to there being no need to correct for such anisotropies.

Figure 3.1 and 3.2 show the ellipticities of the stars in the field of Abell 1995 before and after the correction for PSF anisotropies, respectively. It is seen from the first plot that the stars in this field have systematic ellipticities up to ~7-9% in one direction. The second plot shows that the correction applied has been sucsessful, reducing the star ellipticities to typically <1.5%.

[8] section B.2

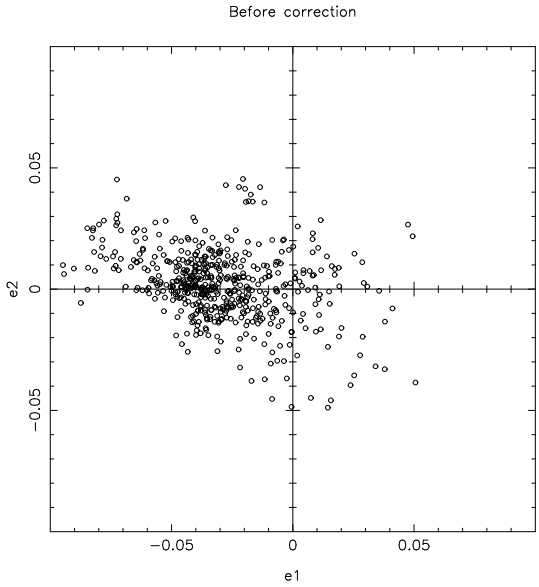

Figure 3.1: Ellipticities of stars in the Abell 1995 field before the correction for PSF anisotropy.

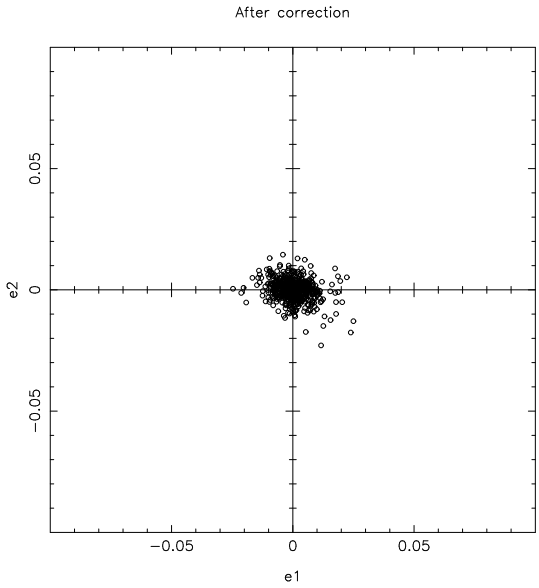

Figure 3.2: Stars in the field of Abell 1995 have now been corrected for PSF anisotropy, and the ellipticities of the stars have clearly been improved as the stars now gather much more in the centre of the plot as opposed to Figure 3.1.

The shear polarisability

In order to convert the observed ellipticities of the background galaxies to an estimate of gravitational shear, the suppression of these ellipticities resulting from smearing by the seeing disk needs to be corrected for. Equation (A.2) defines the pre-seeing shear polarisability, P^γ. To make the equation correspond with the rest of this section subscripts are added, transferring the equation into

$$P^\gamma_{\alpha\beta} = P^{sh}_{\alpha\beta} - P^{sm}_{\alpha\delta} \frac{P^{sh\star}_{\delta\mu}}{P^{sm\star}_{\mu\beta}} \,. \tag{3.17}$$

$P^{sh}_{\alpha\beta}$ and $P^{sm}_{\alpha\beta}$ are the post-seeing shear polarisability tensor and the smear polarisability tensor respectively and $P^{sh\star}$ and $P^{sm\star}$ are the same tensors applied to stellar objects. Combining the correction from equation (3.11) applied earlier with the p^γ seeing correction that still needs to be carried out, the final estimation of the shear is found by Luppino & Kaiser (1997) to be

$$\gamma_\alpha = \frac{e_\alpha - P^{sm}_{\alpha\beta} p_\beta}{P^\gamma_{\alpha\beta}} \,. \tag{3.18}$$

Assuming that the PSF is left almost circular from the corrections already done, the off-diagonal elements of the polarisabilities in equation (3.17) can be neglected as they are expected to be small compared to the diagonal elements. This comes from the fact that the polarisability tensors transform e_α, which is a polar and not a real vector. A polar remains the same when rotated 180°, whilst a vector would turn into its own negative. Because the polarisability tensors transform polars rather than vectors, they are not real tensors. Ideally they would have off-diagonal elements equal to zero, but because of noise in calculations etc., this is not the case. However, the values will be smaller than the uncertainties of these numbers, and can therefore be neglected. By also assuming the object sizes do not change when correcting the ellipticities, the description of the P-values will remain the same after the corrections. The polarisabilities can therefore be estimated using the approximation $P = \frac{1}{2}(P_{11} + P_{22})$, leaving the average $P^{sh\star}/P^{sm\star}$ to be calculated as

$$\left\langle \frac{P^{sh}}{P^{sm}} \right\rangle^\star = \frac{1}{N_{stars}} \sum_{stars} \frac{P^{sh\star}_{11} + P^{sh\star}_{22}}{P^{sm\star}_{11} + P^{sm\star}_{22}} \,. \tag{3.19}$$

The pre-seeing shear polarisability is hence evaluated as

$$P^\gamma = \frac{1}{2}(P^{sh}_{11} + P^{sh}_{22}) - \frac{1}{2}(P^{sm}_{11} + P^{sm}_{22}) \left\langle \frac{P^{sh}}{P^{sm}} \right\rangle^\star \,, \tag{3.20}$$

and with $P^{sh}_{\alpha\beta}$ and $P^{sm}_{\alpha\beta}$ being calculated by `IMCAT` this equation is easily solved for. Having established these results the gravitational shear can then be calculated from equation (3.18).

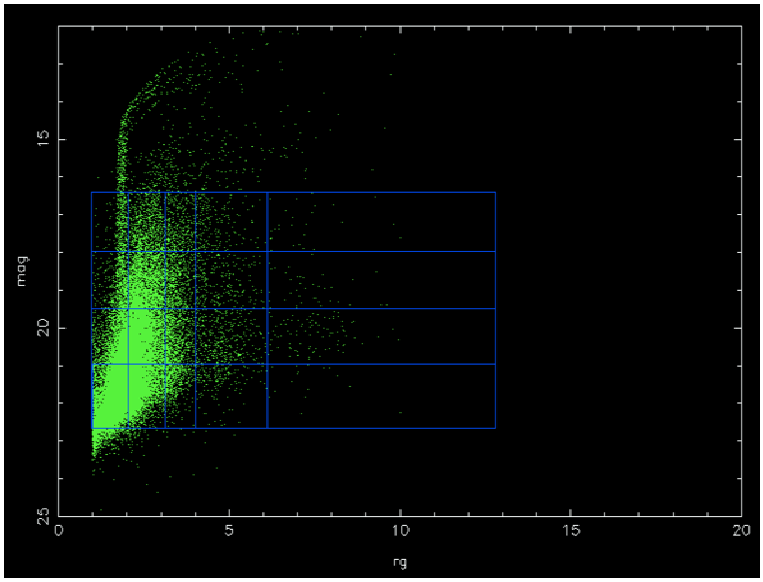

Figure 3.3: The approximate spacing of the bins used in estimating the PSF dilution. The plot is not accurate as the spacing of the bins in x-direction were determined from the average r_g value of the stars, and is merely displayed to obtain a qualitative understanding of the method.

By applying a correction factor of $1/P^{\gamma}$[9] to the galaxy ellipticities, these are converted into a shear. Because estimating the PSF dilution for each individual galaxy will lead to additional noise, a method of determining the median P^{γ} within several bins is applied instead. The background galaxies are displayed in an r_g-magnitude diagram and a grid of bins placed on top of the plot as shown in Figure 3.3. The spacing of the bins are decided by trying to locate approximately the same amount of galaxies in each bin. The median of $1/P^{\gamma}$ for each bin is then computed and applied to the galaxies within that bin.

The faintest and smallest galaxies are more affected by seeing and have lower S/N values than the larger galaxies. Measurements made on them will therefore be noisier. As the S/N of the data increases, the measurements will have lower errors. This is seen from the correction factor calculated for each bin. For bins containing large galaxies this value would converge to unity, whist in bins containing only small and faint galaxies the correction factor would be large. Given that large correction factors indicate low S/N values, these galaxies also have the poorest shape determinations. They are therefore of less importance, and to account for this during the analysis weights are assigned to the galaxies. This is done by calculating a normalised

[9]From equation (3.18), with equation (3.11) already corrected for.

weight,

$$w_i = \left\langle \frac{\sigma_{e_i}}{\langle P^\gamma \rangle_i} \right\rangle^{-2} , \tag{3.21}$$

for each bin. $w_i\gamma_\alpha$ is then used in later calculations rather than γ_α. In the above equation, σ_{e_i} is the observed dispersion of galaxy ellipticities, e, and $\langle P^\gamma \rangle_i$ is the average value of P^γ, both values concerning the i'th bin of the r_g-mag diagram. As w_i is inversely proportional to the dispersion in P^γ, the galaxies with poorly determined $1/P^\gamma$ will be given less weight.

3.2 Mass reconstruction

The surface brightness of distant background objects is mapped according to

$$f_{obs}(\boldsymbol{\theta}) = f_{true}(\boldsymbol{\theta} - \nabla_\theta \phi) , \tag{3.22}$$

resulting from gravitational lensing by a foreground mass concentration along the line of sight. The gravitational surface potential is denoted ϕ, and is related to the dimensionless surface mass density, κ, by

$$\nabla^2_\theta \phi = 2\kappa , \tag{3.23}$$

where κ is given by equation (1.21) and $\nabla^2_\theta \phi$ is derived with respect to the angular coordinate, $\boldsymbol{\theta}$. The surface brightness of a galaxy will be distorted as

$$f_{obs}(\boldsymbol{\theta}) = f_{true}(\psi_{ij}\theta_j) \tag{3.24}$$

where $\boldsymbol{\theta}$ is measured relative to the centre of the galaxy. The distortion (or amplification) tensor is a symmetric 2×2 tensor[10]

$$\psi_{ij} = \delta_{ij} - \frac{\partial^2 \phi}{\partial\theta_i \partial\theta_j} . \tag{3.25}$$

where δ_{ij} is the Dirac function[11].

Looking at equation (3.23) it is possible to express κ in terms of ϕ as

$$\kappa = \frac{1}{2}(\phi_{,11} + \phi_{,22}) \tag{3.26}$$

where the commas represent derivatives with respect to $\boldsymbol{\theta}$;

$$\phi_{,ij} \equiv \frac{\partial^2 \phi}{\partial\theta_i \partial\theta_j} . \tag{3.27}$$

Though κ cannot be measured directly from the shapes of the background galaxies, the mean distortion in these galaxies can be quantified by looking

[10] see also equation (A.7)

[11] $\delta(x - x_i) = 0$ for $x \neq x_i$ and 1 otherwise

for a systematic deviation from an average ellipticity of zero. As a uniform sheet of mass can be added without altering the shear (usually referred to as "the mass sheet degeneracy"), the quantity measured from these distortions is in reality the reduced shear, g,

$$g = \frac{\gamma}{1-\kappa} \; . \tag{3.28}$$

The reduced shear, g, is also referred to as the observable distortions in the background galaxies, and is a combination of shear and surface mass density. As it is assumed that $\kappa \ll 1$ under the weak lensing limit, it is reasonable to use the approximation that $g \approx \gamma$. If the background galaxies are assumed to have an isotropic intrinsic ellipticity distribution[12], the distortion measured in the galaxies can be translated into a shear by a direct scaling.

The relation between γ and ϕ is given by

$$\begin{aligned} \gamma_1 &= \frac{1}{2}(\phi_{,11} - \phi_{,22}) \\ \gamma_2 &= \phi_{,12} \; . \end{aligned} \tag{3.29}$$

The Fourier transform of the shear, $\tilde{\gamma}$, can be converted to that of the surface mass density, $\tilde{\kappa}$. This provides a method for converting the measured shear field to a surface mass density field.

The optimally weighted combination has a flat noise power spectrum and is given by

$$\tilde{\kappa} = \frac{(\tilde{\boldsymbol{k}}_1^2 - \tilde{\boldsymbol{k}}_2^2)\tilde{\gamma_1} + 2\tilde{\boldsymbol{k}}_1\tilde{\boldsymbol{k}}_2\tilde{\gamma_2}}{\tilde{\boldsymbol{k}}_1^2 + \tilde{\boldsymbol{k}}_2^2} \; , \tag{3.30}$$

where the $\tilde{\boldsymbol{k}}_i$ are the coordinates in Fourier space. An estimate of the surface mass density as a convolution of the shear with a kernel, χ_α, is then derived by inverse Fourier transforming the above equation,

$$\kappa(\boldsymbol{\theta}_0) = -\frac{1}{\pi}\int \chi_\alpha(\boldsymbol{\theta} - \boldsymbol{\theta}_0)\gamma_\alpha(\boldsymbol{\theta}) d^2\boldsymbol{\theta} \tag{3.31}$$

with

$$\chi_\alpha(\boldsymbol{\theta}) = \frac{1}{\theta^4}\begin{pmatrix} \theta_1^2 - \theta_2^2 \\ 2\theta_1\theta_2 \end{pmatrix} \tag{3.32}$$

and $\boldsymbol{\theta}_0$ being the location where κ is calculated.

However, as the method[13] assumes an infinite spatial extent of the data field, a bias will occur in the outer parts of the reconstruction as the data obtained will always be finite. Nevertheless, when dealing with wide-field imaging data the observed fields are so large that this will not affect the results in any significant way.

[12] Appendix A

[13] originally presented by Kaiser & Squires (1993)

Due to the mass sheet degeneracy, the method will only be able to measure the surface mass density to within an additive constant, this being the mean surface mass density of the field. Since $g \approx \gamma$ is assumed the mass maps created are more qualitative than quantitative. Contamination from cluster galaxies amongst the background galaxies used in the weak lensing measurements is also not corrected for. However, the maps still present good estimates of cluster mass distributions as these assumptions are reasonable in creating mass maps. When fitting the data to theoretical mass profiles later in this chapter, the errors are looked into and corrected for.

Smoothed mass maps of the galaxy clusters presented in this thesis were generated using the above method. The fainter the object is, the lower is the S/N value of that object in the image. As the background galaxies are the faintest objects in the image, these were extracted by choosing objects with low S/N values. This was done by selecting objects detected at low significance, ν, where $\nu = S/N$ $(6 < \nu < 100)$[14]. The smoothing was done with a two-dimensional Gaussian filter in Fourier space, corresponding to the transfer function

$$T(\tilde{\boldsymbol{k}}) = \exp(-0.5\tilde{\boldsymbol{k}}^2\Theta^2) \,, \tag{3.33}$$

where Θ is the width of the Gaussian. By varying Θ the optimal map can be derived; this being a map containing good balance between spatial resolution and noise. A possibility is to use adaptive smoothing to obtain a more accurately detailed map. This method creates a map that contains the same noise level in the entire image, but where the spatial resolution varies. However, as the above method creates maps accurate enough for the purposes of this thesis, the method of adaptive smoothing will not be looked into. Figure 3.4 shows three different mass maps for each galaxy cluster, these having different Θ-values emphasising how the ratio of noise and spatial resolution can be varied.

Instead of applying this smoothing after the surface mass density is estimated, it can be incorporated directly in equation (3.31) by replacing the Fourier transform of $\chi_\alpha(\tilde{\boldsymbol{k}})$, $2\chi_\alpha(\boldsymbol{\theta})/\pi\theta^2$, by the Fourier transform of $\chi_\alpha(\tilde{\boldsymbol{k}})T(\tilde{\boldsymbol{k}})$. When evaluating equation (3.31) it is converted into a sum over galaxies as e_α is not actually a continuous polar field (as thought of up until now), but rather a set of samples of e_α at the random locations of the background galaxies, $\boldsymbol{\theta}_g$, together with a random intrinsic ellipticity for each galaxy.

With the smoothing applied, the equation will be

$$\hat{\kappa}(\boldsymbol{\theta}_0) = -\frac{1}{2n}\sum_g W(\boldsymbol{\theta}_g - \boldsymbol{\theta}_0)\chi_\alpha(\boldsymbol{\theta}_g - \boldsymbol{\theta}_0)\frac{w_g e_\alpha}{P^\gamma} \,, \tag{3.34}$$

where n is the mean surface number density of the background galaxies, w_g

[14] ν is calculated by the IMCAT program etprofile.

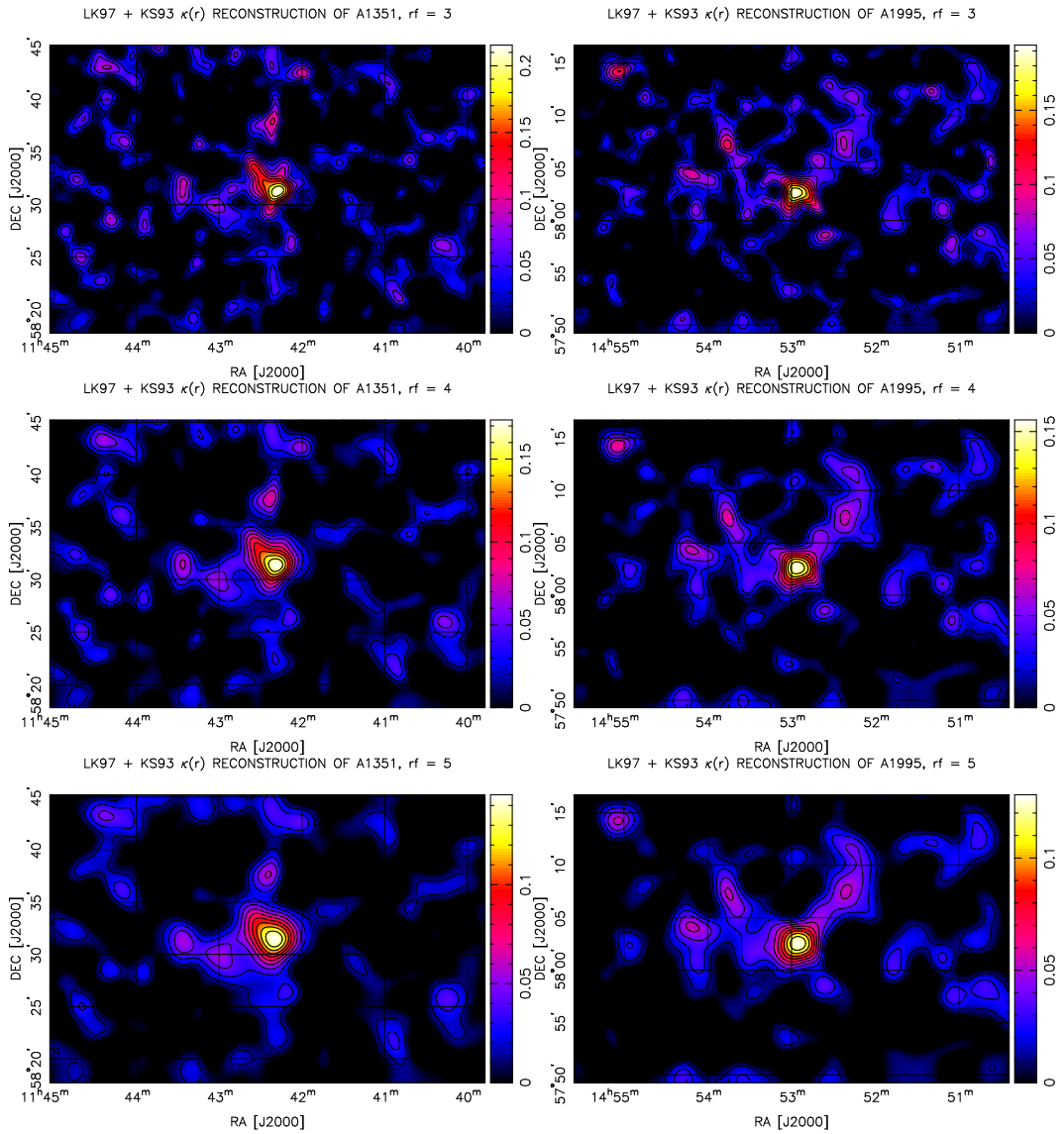

Figure 3.4: The projected surface mass density in the fields of Abell 1351 (left) and Abell 1995 (right). Θ is given in units of pixels of size $12\farcs875$. The values are, from the upper image and down, 3, 4 and 5. The scale bar on the right runs from zero to the highest peak value of κ.

is given by equation (3.21) and W is given by

$$W(\boldsymbol{\theta}) = \frac{1}{(2\pi)^2} \int T(\tilde{\boldsymbol{k}}) J_2(\tilde{\boldsymbol{k}}\boldsymbol{\theta}) d^2\tilde{\boldsymbol{k}} \, . \tag{3.35}$$

Here $J_2(\tilde{\boldsymbol{k}}\boldsymbol{\theta})$ is a second order Bessel function of the first kind[15].

This kind of analysis provides a useful check on whether the detected distortions are really due to gravitational lensing. The distortion field resulting from gravitation has only one real degree of freedom. This is because it is determined by a scalar, the mass density of the cluster. When creating a mass map two components of the shear field are projected; one that is generated by the gravitational lensing and one from noise.

A general distortion field has two real degrees of freedom. Rotating the objects by 45° should result in zero, plus fluctuations due to random noise in the shear estimates. Mathematically this equals calculating the curl of the surface mass density, $\nabla \times \kappa$. This is done by swapping the two components of the shear and changing the sign on one of them. The map created should hence show only random fluctuations as the distortions caused by gravitational lensing should cancel out and only the distortions caused by artificial sources should be visible. Figure 3.5 shows examples of such maps displaying the random noise of the maps in Figure 3.4.

The "control" maps of Abell 1351 show that the distortions detected in the cluster originate from gravitational lensing. The maps show only random fluctuations and these are hence assumed to result from distortions caused by artificial sources.

The corresponding maps of Abell 1995 show more patterns than those of Abell 1351, as the centre consists of zero noise surrounded by some structuring noise containing peaks in a formation around it. These patterns could indicate that the fluctuations are not completely random. However, comparing the noise maps of Abell 1995 to that made by Dahle et al. (2002) shows significant similarities. The noise map of Dahle et al. contains an area in the centre with few fluctuations, and it also contains structuring noise around this area. Most important, both studies show similar peaks in the noise maps, indicating that these peaks are only random noise. In their paper Dahle et al. have measured weak gravitational lensing in 38 galaxy clusters, Abell 1351 and Abell 1995 being amongst these. The clusters of interest are observed using the 8192^2 University of Hawaii CCD mosaic (UH8K) at the 2.24 m University of Hawaii telescope, and the methods used to derive the mass estimations are not the same as used in this thesis. It is therefore plausible that the noise map of Abell 1995 show only random fluctuations, as there can be very few similar systematic effects in both studies.

The mass reconstruction of Abell 1351 from Dahle et al. (2002) is slightly different from the one made in this thesis. The maps generated in this thesis

[15] section B.3

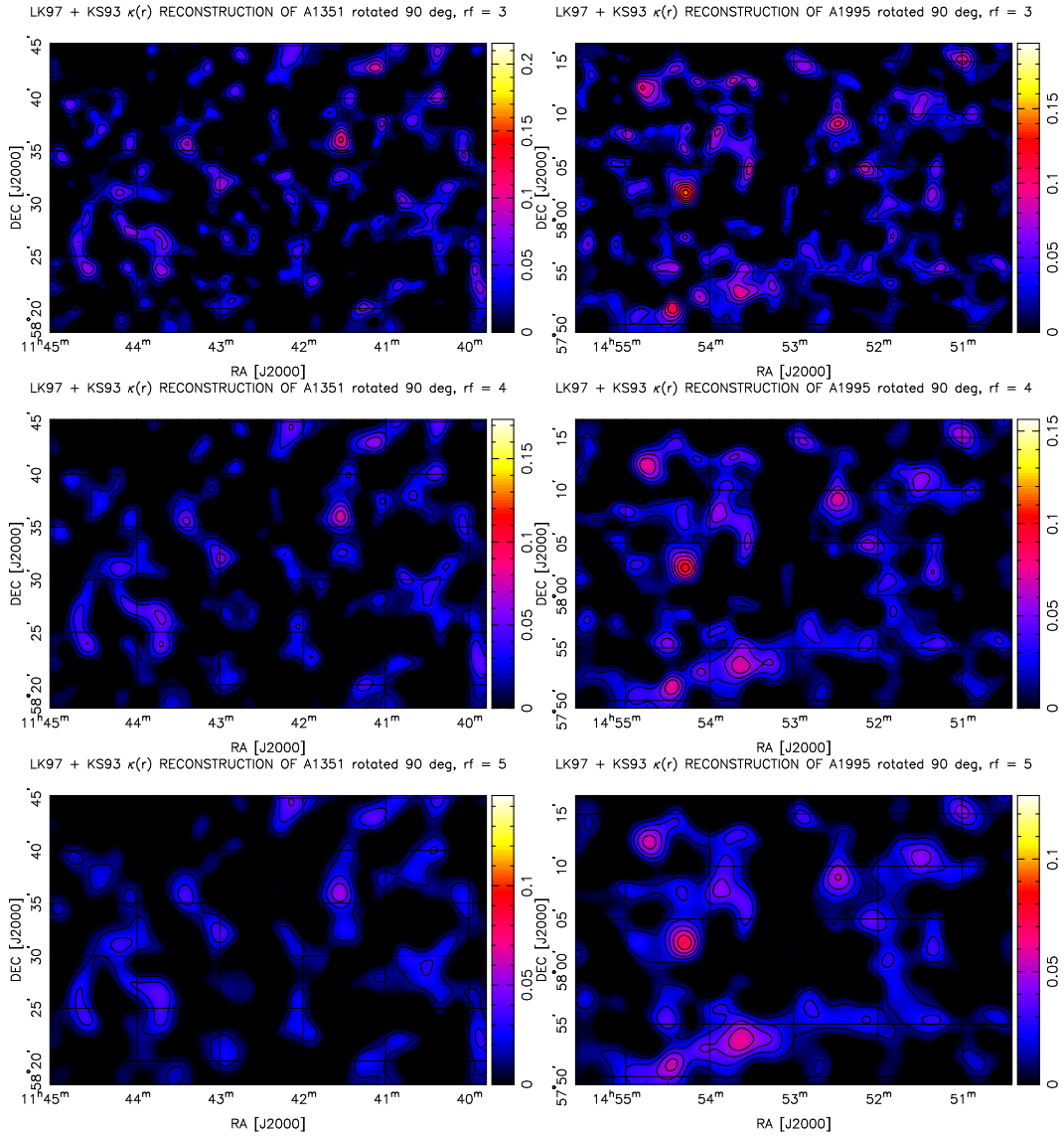

Figure 3.5: Random noise in the mass maps (Figure 3.4) of Abell 1351 (left) and Abell 1995 (right). The values of Θ are given in units of pixels of size $12\farcs875$, shown here are $\Theta = 3, 4, 5$. The scale bar on the right has the same scaling as in the mass maps.

show a mass filament extending from the cluster centre towards the east, and a possible filament extending towards the south. The southward filament contains no peaks, and it is therefore uncertain whether this is really a mass filament. The mass map of Abell 1351 made by Dahle et al. shows only one peak southeast of the centre, but no filament extending further east. However, as the cluster was somewhat unstable in the mass reconstructions by Dahle et al. (priv. comm.), the maps of Abell 1351 presented in this thesis are likely to be more accurate.

The mass reconstructions of Abell 1995 are very similar in the two studies. Both maps show two mass filaments extending towards the northeast and the northwest, indicating mass falling into the centre of the cluster. The mass filaments displayed in the maps can be dark matter extending between galaxies in the cluster. As the mass reconstructions of this thesis map the surface mass density to farther radii than those of Dahle et al., they are believed to be more accurate given the constraints of the reconstruction algorithm. Section 4.1.1 in Chapter 4 covers a discussion on the topic and also gives a detailed comparison of the two studies.

3.3 Modelling the lensing data

The mass of a galaxy cluster can be estimated from comparing observed distortions in the background galaxies to those predicted by realistic theoretical density profiles. The χ^2-test is used to determine the best fit, giving the parameters of the model. An estimate of the cluster mass can then be derived.

The theoretical profiles used in mass estimations in this thesis are both spherically symmetrical. It is therefore convenient to use a tangential average in circular bins of the reduced shear, g_T, to carry out the mass estimations. The reduced tangential shear is related to the tangential shear and the surface mass density by $g_T = \gamma_T/(1-\kappa)$ at radii larger than the Einstein radius[16], θ_E. It is measured in all the background galaxies contained in a faint galaxy catalogue generated by selecting galaxies detected at low significance ($6 < \nu < 100$). The average tangential distortion, $\langle g_T \rangle$, is measured as a function of radius in 17 radial bins. The bins are logarithmically spaced, starting at $r = 150''$ to avoid the large contamination from cluster galaxies close to the centre of the field (see next subsection). This centre is taken to be the location of the peak in the mass map generated in the previous section. The `IMCAT` program `etprofile` measures g_T for all the background galaxies and calculates the average for each bin. The theoretical values of g_T are calculated for the average radius of each bin, $\langle r \rangle_i$.

The relative distance of the background galaxies and the lensing cluster is required when calculating the mass of a cluster. Some information about the

[16] section 1.2.1

redshift distribution ($n(z)$) of the background galaxies is therefore needed. As there is no specific redshift information on the background galaxies the distances have to be estimated statistically. This is done by calculating the mean of $\beta \equiv D_{ds}/D_s$, where D_{ds} is the angular diameter distance between the lens and the source and D_s between the observer and the source. Using the redshift distribution of corresponding faint galaxies from the Hubble Deep Field (HDF) North, $\langle\beta\rangle$ is estimated. The empirical relation

$$\langle\beta\rangle = -1.21 z_l + 0.91 \tag{3.36}$$

is considered an excellent approximation to $\langle\beta\rangle$ in the $0.15 < z_l < 0.35$ range, assuming the ΛCDM (cold dark matter) cosmological model of $\Omega_M = 0.3$ and $\Omega_\Lambda = 0.7$. z_l is the redshift of the lensing cluster. Equation (3.36) is calculated for a ΛCDM model from the relation used in Dahle et al. (2002) for an Einstein - de Sitter model.

Cluster galaxy contamination

At small projected radii from the cluster centre the faint galaxy catalogue will contain some cluster galaxies in addition to background galaxies. As these cluster galaxies are included in the lensing measurements, this contamination will lead to the shear estimates being systematically biased towards lower values. By assuming the edges of the field to be approximately free from cluster galaxies, the density of background galaxies can be estimated. The contribution from cluster galaxies to the background galaxy density is then found by calculating the tangential average in radial bins.

Figure 3.6 shows the percentage of cluster galaxies in the faint galaxy catalogues as a function of distance from the cluster centre. The plot includes both galaxy clusters of interest. Because the cluster contamination at the edges of the field is assumed to be negligible, the average background level is set to zero by subtracting the median value of the image. It therefore appears like the cluster contamination in Figure 3.6 is negative at some radii, but this is merely an effect from random fluctuations in the background and artificially setting the average background level to zero. The cluster galaxy contamination is also displayed in two dimensions in Figure 3.7.

As the measured shear values are lowered because of this cluster galaxy contamination, modifications must be applied to the theoretical shear values. If this is not done before comparing the measured values with the theoretically calculated values, the analysis will not be correct and hence the results not accurate. The reason for adjusting the theoretical values rather than the measured values is that this method is much easier.

To systematically bias down the theoretical shear values a correction value is calculated in radial bins of linear spacing in the faint galaxy catalogue. These correction values are based on each cluster's respective contamination `FITS` file represented by Figure 3.7, the outermost value being

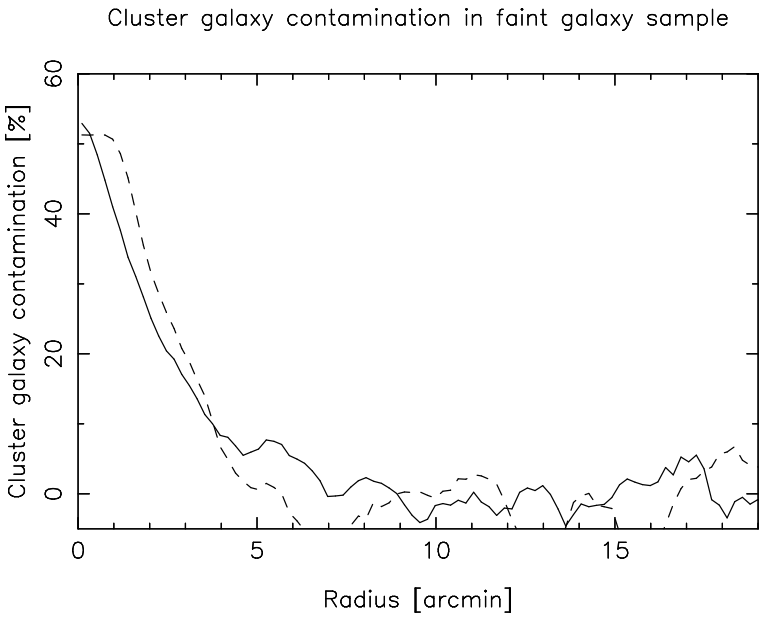

Figure 3.6: The percentage of cluster galaxies in the faint galaxy catalogues. The dashed line represents Abell 1351 and the solid line Abell 1995. The shear values of the clusters are measured from the radial cut-off at 2′.5.

set to 1 to mimic contamination-free boundaries of the field. The theoretical shear value is then multiplied with the corresponding correction value before compared to the measured shear value. The correction values are found by the `IMCAT` program `profile`.

3.3.1 The singular isothermal sphere profile

The singular isothermal sphere (SIS) mass profile is the simplest mass profile used in gravitational lensing analysis. The model assumes that stars and other mass components behave like particles of an ideal gas, confined by a spherically symmetric gravitational potential. The equation of state of these objects is given by

$$p = \frac{\rho k T}{m} \,, \tag{3.37}$$

where p, ρ, and m are the pressure, the mass density and the mass of the objects respectively. k is the Boltzmann constant, $k = 1.38 \times 10^{-23}\mathrm{J/K}$, and T is the temperature. In thermal equilibrium T is related to the velocity dispersion, σ_v, of the objects through

$$m\sigma_v^2 = kT \,. \tag{3.38}$$

As it is assumed that the stellar gas is isothermal, the temperature, or equivalently the velocity dispersion, does not depend on radius but is constant

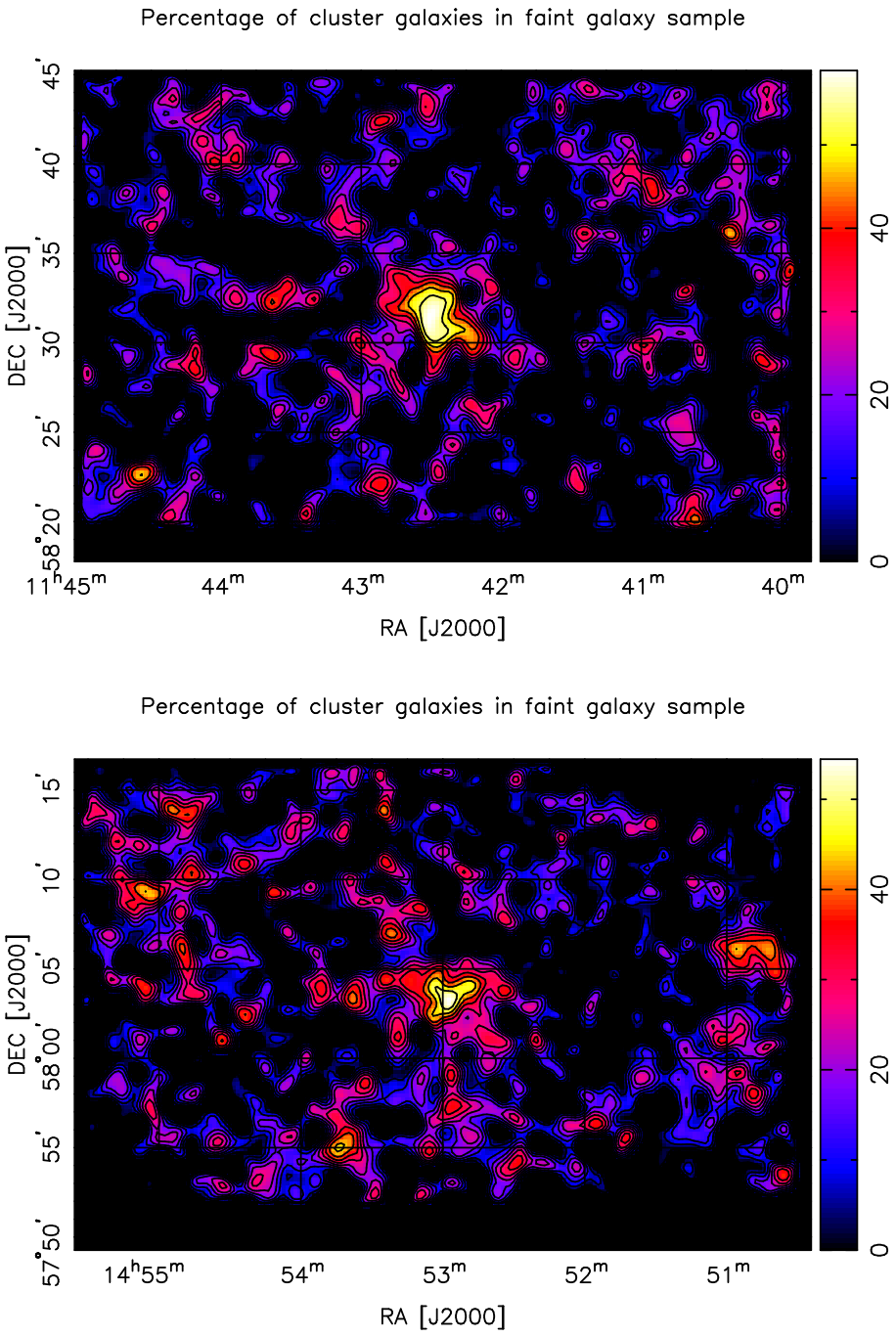

Figure 3.7: The percentage of cluster galaxies in the faint galaxy catalogues displayed in three dimensions, the scale bar running from zero to the percentage value in the image. The upper image shows Abell 1351 and the lower Abell 1995. The radial cut-off from where the shear values are measured is a circle in the centre of the image with a radius of 2′.5. It is clearly seen that the background galaxy catalogues are heavily contaminated inside this cut-off.

across the galaxy cluster. The SIS profile is therefore characterised by σ_v alone, as this is the only free parameter once the cluster centre is fixed. This is seen from the density profile of the model, which is given in terms of a three-dimensional radius, r,

$$\rho_{SIS}(r) = \frac{\sigma_v^2}{2\pi G r^2} \, . \tag{3.39}$$

The radial dependence of the shear for an SIS profile, $\gamma_{SIS}(\theta)$, equals the dependence of the surface mass density, $\kappa_{SIS}(\theta)$, and is given by

$$\gamma_{SIS}(\theta) = \kappa_{SIS}(\theta) = \frac{\theta_E}{2\theta} \, . \tag{3.40}$$

θ is the angular coordinate measured relative to the centre of the galaxy cluster and θ_E is the Einstein radius,

$$\theta_E = 4\pi \left(\frac{\sigma_v}{C}\right)^2 \frac{D_{ds}}{D_s} \, , \tag{3.41}$$

where C is the speed of light. When carrying out the calculations D_{ds}/D_s is estimated by $\langle\beta\rangle$ using equation (3.36).

The best fit is determined by comparing measured shear values to those calculated by the model. The best fit of the SIS profile is determined by calculating χ^2 for a range of σ_v values, letting the smallest χ^2 value decide the best fit. The results are shown in Table 3.1.

3.3.2 The NFW profile

The Navarro, Frenk & White (NFW) profile appears to give a very good description of the radial mass distribution inside the virial radius, r_{vir}, of a galaxy cluster. It is derived from fitting the density profile of numerical simulations of cold dark matter halos (Navarro et al. 1997). The virial radius is defined as the three-dimensional radius inside which the "steady" cluster galaxies are contained. The galaxies outside r_{vir} are yet to fall towards the centre of the cluster for the first time, after which a more or less steady oscillation towards and from the cluster centre is entered. For an Einstein - de Sitter universe ($\Omega_M = 1$, $\Omega_\Lambda = 0$) the virial radius equals r_{200}, the radius inside which the mass density of the cluster equals $200\rho_c$.

The NFW mass density profile is given by

$$\rho_{NFW}(r) = \frac{\delta_c \rho_c}{(r/r_s)(1 + r/r_s)^2} \, , \tag{3.42}$$

where

$$\rho_c = \frac{3H^2(z_l)}{8\pi G} \tag{3.43}$$

is the critical density[17], $H(z_l)$ is the Hubble parameter at the redshift of the cluster, z_l, and G is the gravitational constant. δ_c is defined as the characteristic over-density for the cluster,

$$\delta_c \equiv \frac{200}{3} \frac{c^3}{\ln(1+c) - c/(1+c)} , \tag{3.44}$$

where c is a dimensionless number known as the concentration parameter. The scale radius, r_s, is a characteristic radius of the cluster given by

$$r_s = \frac{r_{200}}{c} , \tag{3.45}$$

The mass of an NFW cluster contained within r_{200} can then be expressed as

$$M_{200} \equiv M(r_{200}) = \frac{800\pi}{3} \rho_c r_{200}^3 . \tag{3.46}$$

The analytical expressions for shear and surface mass density for the NFW profile are derived by Wright & Brainerd (2000). Only a short description is given here, further details are found in the paper. The quantities of γ_{NFW} and κ_{NFW} are hence given from the equations,

$$\gamma_{NFW}(x) = \frac{\bar{\Sigma}_{NFW}(x) - \Sigma_{NFW}(x)}{\Sigma_{crit}} \tag{3.47}$$

and

$$\kappa_{NFW}(x) = \frac{\Sigma_{NFW}(x)}{\Sigma_{crit}} , \tag{3.48}$$

where x is a dimensionless radius,

$$x = \frac{R}{r_s} . \tag{3.49}$$

R is the projected radius relative to the centre of the cluster lens, given by $R = D_l(\theta_1^2 + \theta_2^2)^{1/2}$, where D_l defines the angular diameter distance between the observer and the lens. $\Sigma_{NFW}(x)$ describes the radial dependence of the surface mass density of an NFW lens and is derived by integrating equation (3.42) along the line of sight. $\bar{\Sigma}_{NFW}(x)$ is the mean surface mass density inside x.

The existing FORTRAN program gamma.f (H. Dahle, priv. comm.) was used to calculate γ_T and κ. This was done for different values of c, ranging from 0.1 to 24.9 in steps of 0.1. When estimating cluster mass at radii larger than the virial radius, an additional error from contamination concerning the projected structures outside r_{vir} must be taken into account[18] (Metzler

[17] section 1.1

[18] See section 4.1 for a further discussion about this paper.

et al. 2001). A correction factor is therefore applied to the error estimates of M_{200} during the calculations.

The NFW density profile is shallower than the SIS near the centre of the cluster but steeper in the outer parts. Once the centre of the cluster is fixed, the NFW profile has two free parameters; r_{200} and c. The first fitting process was done by keeping c fixed and varying r_{200}, the best fit (and the corresponding r_{200}) being determined by the smallest χ^2 value. The value of c is determined by Bullock et al. (2001) using the ΛCDM cosmological model together with $h = 0.7$ and $\sigma_8 = 1.0$, where $M_\star \simeq 1.5 \times 10^{13} h^{-1} M_\odot$ at $z = 0$. For a ΛCDM model[19] $r_{200} = 1.194 r_{vir}$, and the empirical expression for c is given by

$$c = \frac{5.8}{1.194(1 + z_l)} \, , \tag{3.50}$$

where the number 5.8 is estimated from numerical simulations and is considered accurate for a halo with virial mass $M_{vir} = 8 \times 10^{14} M_\odot$. As the mass in these simulations only varies as $\sim M_{vir}^{0.13}$ and is close to the mass estimates of Abell 1351 and Abell 1995, this mass dependence can be disregarded. Equation (3.50) is therefore considered a good estimate of c for the data in this thesis. The number 1.194 comes from converting r_{vir} to r_{200} and must be applied when using cosmological models containing a cosmological constant different from 0. Table 3.1 shows the results from this fitting process.

In the second fitting process both r_{200} and c are altered, creating a grid of c, r_{200} values. The best fit r_{200} is first determined for each value of c[20], then the best fit c is found. Both of these "best fit" determinations are done by minimising χ^2. Figure 3.9 plots the process, showing the different χ^2 values as c is altered. M_{200} is plotted as a function of c in Figure 3.8, giving the parameters at a 68% confidence level. The results from this fitting process are shown in Table 3.1. This table also shows M_{500}, the mass inside r_{500}.

Figure 3.10 displays $\langle g_T \rangle$ as a function of radius for both galaxy clusters. The measured values of $\langle g_T \rangle$ are shown as points with error bars at a 68% confidence level. The best fit models from the SIS and NFW profile are indicated by lines. The models are corrected for cluster member contamination.

[19] $\Omega_M = 0.3$ and $\Omega_\Lambda = 0.7$

[20] ranging from 0.1 to 2.4 in steps of 0.1

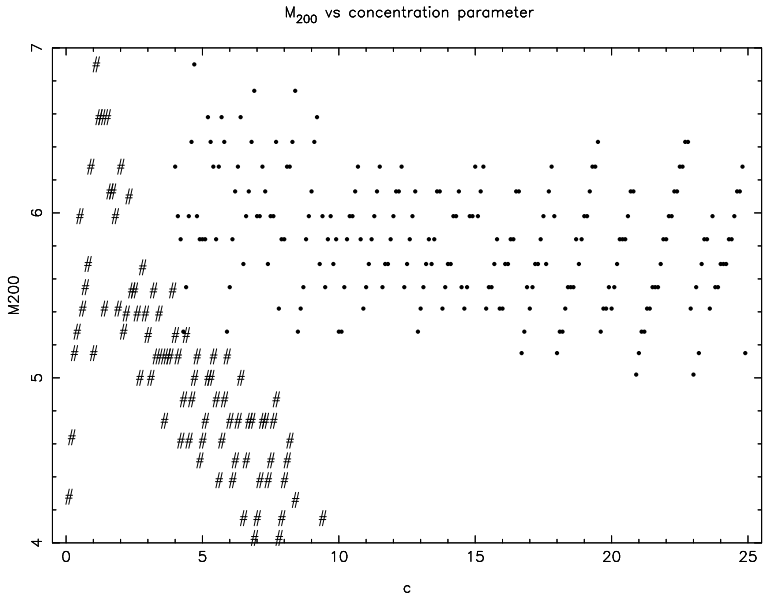

Figure 3.8: The best fit values for the concentration parameter at a 68% confidence level. The y-axis represents the corresponding mass at r_{200}. The values of Abell 1351 are marked with a filled circle and the values of Abell 1995 with a #. The best fit value for Abell 1351 is $c = 21.7$, and $c = 0.9$ for Abell 1995.

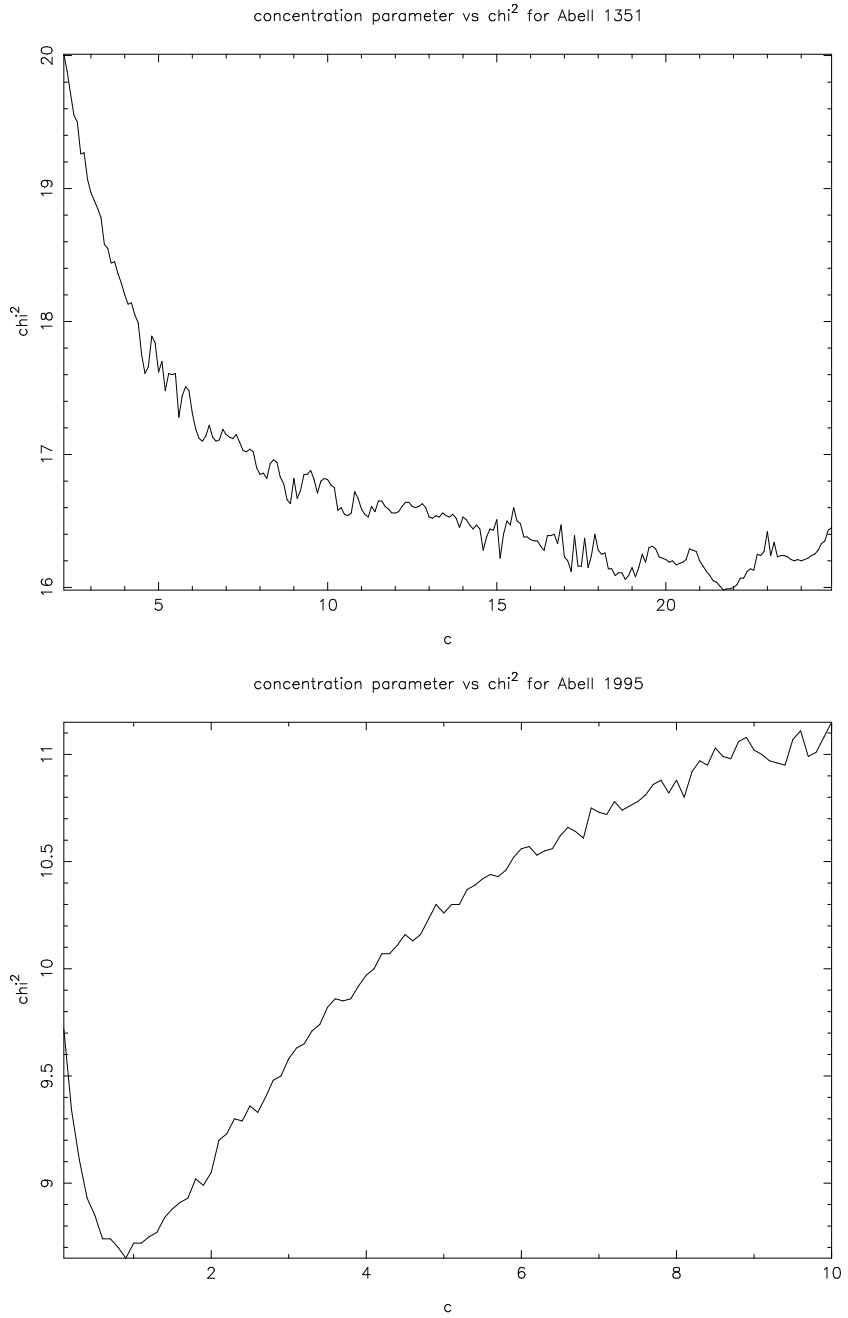

Figure 3.9: χ^2 given as a function of c for the NFW profile with c as a free parameter. The upper plot represents Abell 1351 and the lower Abell 1995. The best fit c values are $c = 21.7$ for Abell 1351 and $c = 0.9$ for Abell 1995.

SIS	Abell 1351	Abell 1995
θ_E	$16\farcs2 \pm 3\farcs6$	$14\farcs4 \pm 4\farcs3$
σ_v [km s^{-1}]	1040 ± 115	980 ± 145
χ^2_ν	1.26	0.59
NFW, fixed c		
c	$3.67^{+1.88}_{-1.25}$	$3.68^{+1.89}_{-1.25}$
r_{200}	$386\farcs6 \pm 38\farcs1$	$358\farcs7 \pm 46\farcs0$
r_{200} [h^{-1}Mpc]	1.27 ± 0.12	1.17 ± 0.15
M_{200} [$10^{14}h^{-1}M_\odot$]	6.58 ± 2.59	5.13 ± 2.38
χ^2_ν	1.15	0.62
NFW, free c		
c	21.7 ± 13.8	$0.9^{+2.3}_{-0.7}$
r_{200}	$365\farcs3 \pm 24\farcs4$	$380\farcs5 \pm 60\farcs9$
r_{200} [h^{-1}Mpc]	1.20 ± 0.08	1.25 ± 0.20
M_{200} [$10^{14}h^{-1}M_\odot$]	5.55 ± 1.82	6.28 ± 3.43
χ^2_ν	1.00	0.54
NFW, "best fit" fixed c		
c	21.7 ± 13.8	$0.9^{+2.3}_{-0.7}$
r_{500}	$255\farcs7 \pm 16\farcs7$	$211\farcs5 \pm 35\farcs3$
r_{500} [h^{-1}Mpc]	0.84 ± 0.05	0.69 ± 0.11
M_{500} [$10^{14}h^{-1}M_\odot$]	4.78 ± 1.63	2.68 ± 1.28
χ^2_ν	1.00	0.54

Table 3.1: Best results for Abell 1351 and Abell 1995 I band shear profile. For SIS the results are given in terms of the velocity dispersion, σ_v, and for NFW in terms of r_{200} (definition given in the text) and the concentration parameter, c. $M_{200,500}$ are the two-dimensional projected masses inside $r_{200,500}$, and χ^2_ν is χ^2/Df, where Df is the number of degrees of freedom, given by the number of fitting points minus the number of free parameters. The error limits are given at a 68% confidence level.

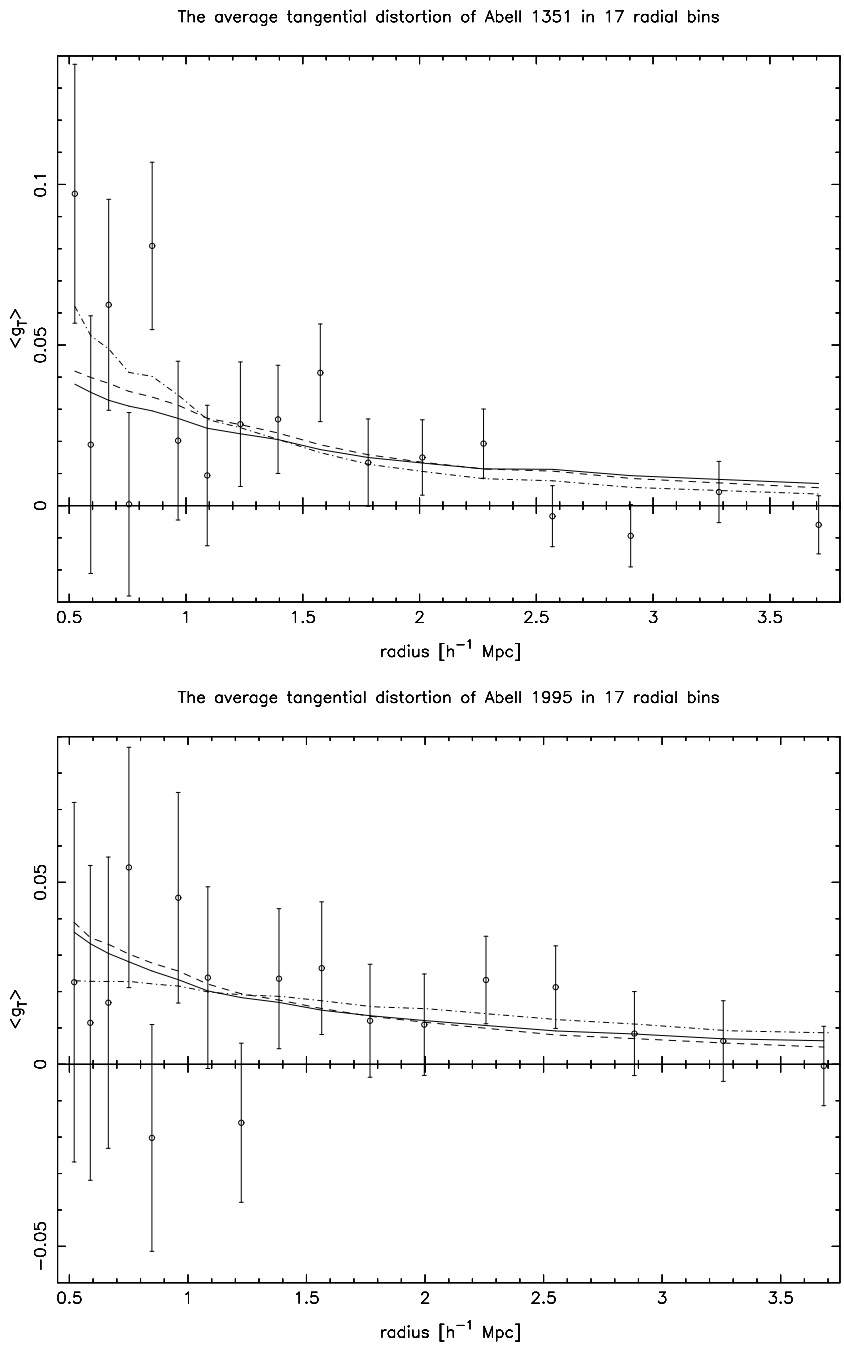

Figure 3.10: The reduced tangential shear as a function of radius for Abell 1351 (top) and Abell 1995 (bottom). The averaged gravitational lensing distortion of background galaxies are shown as points with error bars at a 68% confidence level. The lines indicate the best fit models, the solid line representing the SIS profile, the dashed line the NFW profile and the dot-dashed line the NFW profile with the best fit c parameter.

Chapter 4

Discussion and conclusions

This thesis presents a reconstruction of the mass density profiles of the galaxy clusters Abell 1351 and Abell 1995. The results are obtained using weak gravitational lensing. The estimated mass distributions are based on measurements of shear values from data obtained with the `CFH12K` mosaic CCD camera at the Canada-France-Hawaii 3.6 m Telescope (`CFHT`). The shear values are measured using an improved and corrected version of the KSB95 method (Kaiser, Squires and Broadhurst, 1995), the corrections to the model presented by Luppino & Kaiser (1997).

The three-dimensional mass distribution in the clusters are estimated assuming that the clusters are spherically symmetric and following either a Singular Isothermal Sphere (SIS) profile or a Navarro, Frenk & White (1995; NFW) profile. The estimates are based on the ΛCDM model, with $\Omega_M = 0.3$ and $\Omega_\Lambda = 0.7$. Mass maps are generated using two-dimensional reconstructions of the dimensionless surface mass density. The mass estimates given at r_{200} and r_{500} are estimated by fitting the shear measurements to theoretical models. Both the SIS model and the model are applied to the data. Finally the concentration parameter of the NFW profile is estimated for the two galaxy clusters. The results from this process were remarkable, as the best fit gave concentration parameters quite different from those typically found.

Throughout this chapter and unless otherwise is stated, when referring to results obtained in this thesis using an NFW model (r_{200} and M_{200}), the results are those obtained using a free c parameter.

4.1 Results

X-ray observations provide an efficient method to measure substructure and determine the dynamical state of galaxy clusters, particularly data obtained from Chandra and XMM-Newton (Irgens et al., 2002). Allen et al. (2003)

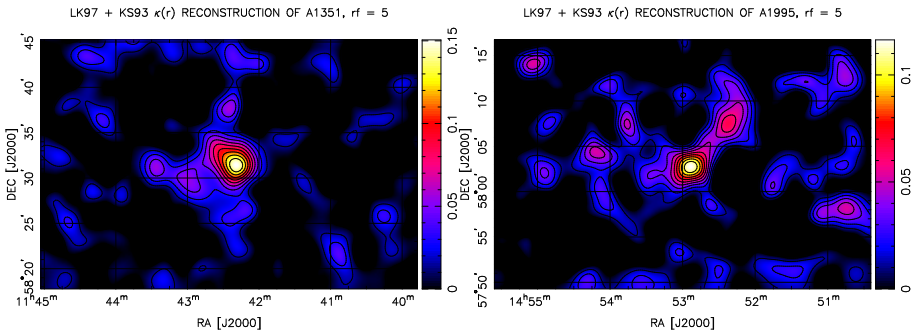

Figure 4.1: The mass maps of Abell 1351 (left) and Abell 1995 (right) ($\Theta \approx 64''$).

present a study based on Chandra[1] X-ray data showing that the galaxy cluster Abell 1351 exhibit significant dynamical activity and is undergoing a major merger event. Examining the surface mass density profile in Figure 4.1 and the shear measurements of Abell 1351 confirm that there are two mass concentrations about to fuse together, suggesting the cluster to be in a formation phase. Allen et al. show that the cluster does not have a simple X-ray structure, also supporting this indication.

Irgens et al. (2002) estimate the dynamical velocity dispersion and virial mass of five X-ray-luminous rich clusters, including Abell 1351. Their study is based on a virial analysis, applying the virial theorem to positions and velocities of cluster galaxies. Such analyses assume the cluster to be in dynamical equilibrium. As discussed above this is not the case for Abell 1351, suggesting that this inaccurate approach may be the reason for the unusually high velocity dispersion of $\sigma_v = 1680^{+340}_{-229}$ km s^{-1} obtained by Irgens et al. Taking the uncertainties into account, neither the velocity dispersion, the virial radius, nor the mass estimates in their study are consistent with those found in this thesis. Irgens et al. found σ_v using the SIS profile, whilst $r_{vir} = r_{200}/1.194$ and $M_{vir} = M_{200}/1.194^3$ are found using the NFW profile. The estimates of r_{vir} by Irgens et al. would be 13% larger assuming a ΛCDM model, compared to the numbers presented in the paper which is calculated assuming an Einstein - de Sitter universe. This is accounted for when comparing the results. There are also some uncertainities in the virial mass estimates in the Irgens et al. paper regarding possible bias arising from including/excluding galaxies outside/inside the virialised part of the cluster.

The colour-magnitude diagram of a cluster will clearly display the cluster galaxy red sequence consisting of early-type galaxies. As these galaxies are typically large and elliptical they will gather in an area of the diagram called the red sequence, located around the same colour and covering about

[1]ROSAT X-ray data were also presented in the study, however the clusters of interest were observed using only Chandra.

half the magnitude range, starting at small values. Irgens et al. (2002) exploit this fact to separate cluster members from possibly background or foreground galaxies, as these objects will have different $V-I$ and hence appear different places in the diagram. They apply this to Abell 1351, yielding a colour-magnitude diagram clearly showing an additional red sequence at smaller colour values than those of the cluster members. This hence implies a structure of foreground or background galaxies.

Comparing a galaxy sample containing all galaxies down to a certain magnitude with a sample where appropriate cuts have been made in the colour-magnitude diagram[2], Irgens et al. found clear evidence of a foreground mass structure[3] when looking at Abell 1351. Metzler et al. (2001) argue that large-scale structures surrounding the galaxy clusters ($r \sim 10 - 20\ h^{-1}$Mpc) may be a source of bias in weak lensing mass estimates. Using numerical simulations of structure formation in a ΛCDM model they quantify the effect large-scale structure has on the weak lensing estimates of M_{200}. They conclude that the mass estimates are likely to be overestimated by $\sim 30\%$ on average. However, more distant, uncorrelated structure along the line of sight to the cluster is not expected to cause errors in the weak lensing measurements (Metzler et al. 2001). In this thesis this possible bias in mass estimates is accounted for by larger error bars in the NFW fitting process[4]. A corresponding correction factor in the velocity dispersion is not known, therefore no corrections were applied to the SIS estimate.

The galaxy cluster Abell 1995 is quite different from Abell 1351. It is assumed to be a stable cluster in dynamical equilibrium, which is probably the reason that X-ray studies of this cluster are more compatible with lensing studies. Including error bars in the calculations, the mass estimates of Abell 1995 introduced in this thesis are consistent with the X-ray based estimate made by Dühring (2002). Patel et al. (2000) present an X-ray based estimate about twice as large, though the velocity dispersion of Patel et al. is more consistent with that of this thesis. Both these studies assume a ΛCDM model. The velocity dispersion and the mass measurements obtained in this thesis are calculated using different estimate profiles[5]. This is a reason why the consistency can vary when comparing both the velocity dispersion and the mass estimates to other studies that are not based on gravitational lensing. The σ_v for Abell 1995 derived by Irgens et al. (2002) is very similar to that of Patel et al. Although the virial radius presented by Irgens et al. is consistent with that of this thesis (converting the results into a ΛCDM model) the virial mass differs by an amount of 2×10^{14} M$_\odot$. This shows that even though the mass estimates are not similar for different types of studies,

[2]The cuts were made to include early-type galaxies at the cluster redshift.

[3]A foreground mass structure is additional mass along the line of sight, like galaxies belonging to other clusters.

[4]section 3.3.2

[5]σ_v is estimated using the SIS profile, and M_{200} using the NFW profile.

the differences could depend solely on different mass estimation profiles.

Both clusters show signs of strong gravitational lensing in the centre, especially Abell 1351 that has a clearly visible arc near the centre of the cluster (Ytre-Eide, 2005). This means that the surface mass density here is larger than the critical surface mass density. By applying strong gravitational lensing to the cluster centre the morphology can be examined more closely than possible using only weak lensing. However, as strong lensing is very concentrated, only the structure close to the arcs can be examined this way. As a result strong lensing can only be applied to the centre of the cluster, and when mapping the mass structure of a whole cluster weak lensing must be used. The appearance of strong lensing in a cluster will not affect the weak lensing measurements in any significant way. However, Kneib et al. (2003) argue that including strong lensing information improved the precision of both the mass and concentration estimates in their study, suggesting that there are good reasons for doing so.

Figure 3.10 plots the measured shear values as a function of radius. The diagrams clearly show that the NFW profile with a free concentration parameter is the best fit model to these clusters, as this curve follows the shear measurements more closely than the other profiles. The SIS profile and the NFW profile keeping c fixed are in very good agreement with each other. This is surprising, because the SIS model is in general assumed not to be a good estimator of the mass density profile, whilst the NFW is expected to map the density quite close. The difference in the NFW curves of different concentration parameters hence shows the importance of applying a correct c to the profile.

A larger field of view yields more accurate lensing measurements of the mass, due to the larger number of background galaxies in the field. The estimate of the mass density is improved with the weak lensing signal, this itself improves with the amount of shear measurements of the field. In many clusters there also exists large amounts of mass at large radii, which means that with a small field of view the whole cluster is actually not imaged. A larger field of view will therefore give better constraints on the concentration parameter of the NFW profile, and therefore on the mass density profile of the galaxy cluster. The concentration parameter is defined as the ratio of r_{200} to the scale radius, indicating that a small c would yield $r_s \rightarrow r_{200}$. As defined by the NFW profile, $\rho(r) \propto r^{-1}$ at radii smaller than r_s and $\rho(r) \propto r^{-3}$ at radii larger than r_s. This implies that for clusters with a small concentration parameter (and hence a large r_s) the mass density is decreasing more slowly when going to larger radii than for clusters with a large c value.

As the best fit c for Abell 1351 was quite large, this implies that the cluster has a small scale radius. A small r_s hence leads to the conclusion that most of the mass of Abell 1351 is concentrated close to the centre of the cluster. Figure 3.10 also suggests this, as the steep (best fit NFW) curve

close to the centre indicates that the shear values decrease rapidly. To obtain an accurate c parameter, it is necessary to set the radial cut-off from where the shear values are measured[6] close to the cluster centre. As most of the cluster mass is concentrated within r_s this cut-off must be set to a value less than r_s. In order to obtain the correct concentration parameter, the scale parameter must be contained in the mass estimate (as c is estimated from r_s). Figure 3.9 shows a sharp turn and a clearly determined best fit value of c for Abell 1995, whilst the curve for Abell 1351 does not cleanly present the best fit c parameter of this cluster. This is presumably resulting from not measuring the shear values of small enough radii concerning Abell 1351, whilst it was not a problem for Abell 1995 which has a large scale radius close to r_{200}. Figure 3.10 too indicates that r_s is large. If the mass density of a cluster is decreasing slowly ($\rho \propto r^{-1}$), the shear values will decrease slowly too, indicating that the mass is almost evenly distributed going from small to large radii. As seen in Figure 3.10 this phenomenon is present in the Abell 1995 cluster, the best fit curve being close to flat.

Bullock et al. (2001) present a study of dark matter halo density profiles in a high-resolution N-body simulation using a ΛCDM cosmology. Their sample contains about 5000 haloes in the mass range $10^{11} - 10^{14} h^{-1}$ $M_\odot$ at $z = 0$. The sampling is made such that the halos are found in any environment and is not dependent on the dynamical stage of the halo after virialisation. Bullock et al. find that for halos of the same mass, the concentration, $c_{vir} \equiv r_{vir}/r_s$, can be given by $c_{vir} \propto (1+z)^{-1}$, where z is the redshift of the halo. This is contrary to earlier beliefs that c_{vir} does not vary much with redshift. Equation (3.50) is derived from this conclusion, implying that there is a general "best fit c" that can be applied to all types of galaxies.

Despite the study of Bullock et al. (2001), most clusters looked at or simulated for the purpose of finding a good general concentration parameter for a typical galaxy cluster are stable clusters with a simple structure. Numerically simulated clusters typically have concentration parameters around 4-5 (Kneib et al. 2003; Broadhurst et al 2005), somewhat smaller than obtained here for Abell 1351 and larger than for Abell 1995. The results in this thesis hence give a larger spread in c values than expected, proving it hard to obtain such applicable parameter.

The predicted best fit c value was not expected to apply to Abell 1351 as it is not dynamically stable and there is strong evidence of a foreground mass structure. For Abell 1995, which is characterised as a stable cluster, the predicted best fit c is closer to the one measured in this thesis. Within error bars the two c values are consistent. However, the error bars of c presented in this thesis are somewhat large and may be overestimated. Because the values of γ_T and κ are calculated in advance using a FORTRAN program

[6] section 3.3

(gamma.f[7]), there are restrictions on the values applied by $x = R/r_s$[8]. When c reaches large values during the fitting process the x values tend to get too large for γ_T and κ to be calculated, making it difficult to obtain reliable χ^2 values for that particular c. This makes it difficult to estimate both error bars. The uncertainty of the best fit concentration parameter is therefore set to $\pm$ the largest error value of c to make the estimations more robust.

Kneib et al. (2003) present a wide-field lensing study of the cluster Cl 0024+1654 using data obtained from the Hubble Space Telescope (HST). They fit both the SIS and NFW (free c) profiles, and in addition a cored power law (CPL) model. The best fit concentration parameter from this paper is (for the central mass concentration) $c = 22^{+9}_{-5}$, similar to that of Abell 1351 estimated in this thesis of $c = 21.7 \pm 17.0$. There are other papers indicating large concentration parameters. Gavazzi (2005) and Broadhurst et al. (2005) conclude with c values of $c = 11.73 \pm 0.55$ and $c = 13.7^{+1.4}_{-1.1}$ respectively. Due to the spread in c values, it seems there are more underlying factors driving the value of the concentration parameter than are taken into account when trying to estimate it from simulations. It might not even be possible to estimate a generally applicable value of c.

Kneib et al. conclude that the large-scale distribution of total mass in the cluster Cl 0024+1654 over $0.1 < r < 5$ Mpc is reasonably well fitted by an NFW-like profile (Kneib et al., 2003). The NFW method with two free parameters hence gives a reasonable mass estimate when fitting lensing shear measurements to the profile.

4.1.1 Comparison with Dahle et al. 2002

Dahle et al. (2002) present weak gravitational lensing mass measurements of 38 highly X-ray luminous galaxy clusters, including Abell 1351 and Abell 1995, assuming an Einstein - de Sitter cosmology. They present mass maps generated using the same method (Kaiser & Squires, 1993 (KS93)) as in this thesis. However, in deriving the results their maps are based on, the clusters of interest are observed using a different telescope (`UH` 2.24 m telescope), a different camera (`UH8K`) and a different shear estimator (Kaiser 2000; K2K). The results achieved in this thesis can therefore reasonably be compared to the Dahle et al. paper to obtain an external check.

The images of Dahle et al. are slightly deeper, but the differences are marginal[9]. They observe a smaller field than that of this thesis by a factor of three. As they use a smaller telescope and a less sensitive detector the exposure time is longer. The seeing is quite similar in the two data sets,

[7] section 3.3.2

[8] The calculations for γ_T and κ were done for x values ranging from zero to one hundred. The equation for x is given in equation (3.49).

[9] The differences were 0.15 I magnitude for Abell 1351 and 0.3 for Abell 1995, given for objects detected at a given S/N level.

though in average about 0.″1 better for Abell 1995 in the Dahle et al. study. As this difference is negligible the conclusion is that the image quality of the data sets are roughly the same.

The methods used to measure the shear in the two data sets are fairly different. The K2K (Kaiser 2000) method used in the Dahle et al. paper is in principle more accurate, and is an improved development of the KSB95 (Kaiser et al., 1995, modified by Luppino & Kaiser, 1997) method used in this thesis. It is also newer, and hence should be more up-to-date. On the other hand, the KSB95 method is more thoroughly tested, and it is easier to implement. The reason for choosing this method in this thesis was therefore that it would be easier to learn and apply to the data. Also, as the Master's thesis is time-limited, it was uncertain whether there was a sufficient amount of time to be spent learning the K2K method. The KSB95 method gives an underestimate of the measured shear values (tested on simulated data) of 2% - 15%, strictly depending on details in its implementation. It also makes some assumptions that are not strictly correct, but in reality they seem not to affect the results in a noticeable manner.

The two $\kappa(r)$ reconstructions of Abell 1995 presented by Dahle et al. and in this thesis are very similar. They both show filaments extending towards the northeast and the northwest. The northeastern filament is bigger in the map of this thesis, extending further east than that of Dahle et al. This can be explained from limitations in the κ reconstruction algorithm, as the algorithm sets the net mass inside the field to zero. In the presence of real mass concentrations in the field, the height of the mass peaks are biased downward with respect to the random shear as a result of this. It is clear that when using this method to estimate a $\kappa(r)$ field, the reconstruction will be more accurate with the larger field of view. The field in this thesis is three times larger than that of Dahle et al. It reaches radii at which the projected mass density is expected to be small, keeping the bias at a minimum.

The $\kappa(r)$ reconstructions of Abell 1351 in the two data sets are a bit more different, though the main peaks are still the same. The map of Dahle et al. show a filament extending towards the southeast, whereas in the map of this thesis this filament stretches more directly towards the east, and in addition another filament extending towards the south has appeared. The mass peak in the centre is also larger, again resulting from bias in the $\kappa(r)$ reconstruction algorithm. The work done on Abell 1351 by Dahle et al. also suffers from a somewhat unstable reconstruction (priv. comm.), leading to the conclusion that this thesis' study of Abell 1351 is more accurate.

The Dahle et al. study uses the SIS profile to estimate the mass concentration, given in terms of the velocity dispersion. Again the estimates of σ_v for Abell 1995 are similar, Dahle et al. giving an estimate about 50 km/s higher taking the uncertainties into consideration. This can easily be ex-

plained from the fact that Dahle et al. use the assumption[10] $g_T = \gamma_T$ in their estimations rather than deriving the accurate expression of $g_T = \gamma_T/(1+\kappa)$. In contrast to Abell 1995, the σ_v estimates for Abell 1351 differ by about 200 km/s with uncertainties, the Dahle et al. estimate again being the highest. As Dahle et al. have assumed an Einstein - de Sitter cosmology, their σ_v values will be slightly different compared to a ΛCDM model, but will not have a big influence on the conclusions made from this section.

Allen et al. (2003) have used the Dahle et al. observations to obtain mass estimates using the NFW model and assuming a ΛCDM model. The results of this thesis obtained using the same model and varying r_{200} and c gave somewhat different results. The mass estimate by Allen et al. for Abell 1995 is consistent to that of this thesis, mainly due to the large error bars. For Abell 1351 the mass estimate given by Allen et al. is about 2.3 times as large as that of this thesis, uncertainties included. Estimating M_{200} using a fixed $c = 5$ as Allen et al. did yields little differences concerning Abell 1351. For Abell 1995 this process resulted in the error bars being halved, leading to a mass estimate not consistent with that of Allen et al. It therefore seems like Allen et al. have used larger r_{200} values than used in this thesis, as this would also lead to larger values of M_{200}.

Comparing the tangential shear values of Abell 1351, the values obtained by Dahle et al. are higher than those of this thesis by a value of 0.1 on average, disregarding error bars. Taking the uncertainties into consideration they are close to consistent. These discrepancies are probably the reason to the differences in σ_v discussed earlier. The $\langle g_T \rangle$ values decrease more rapidly in the Dahle et al. study, indicating the same as concluded in this thesis about the dynamical state of the cluster. The $\langle g_T \rangle$ vs. radius plot of Abell 1995 was not presented in the Dahle et al. paper, and therefore no comparisons are made for this cluster, regarding the tangential shear values.

The similarities in the two studies are much larger than the differences. This implies that the work done in this thesis is reliable, and the results worth taking notice of. The larger field of view in the images of this thesis provides a better mass estimate than that of Dahle et al. This in particular applies to the galaxy cluster Abell 1995 that shows strong indications of a large r_s and hence a large mass concentration also at large radii. The large amount of background galaxies in the field improves the lensing measurements, and hence the estimates of the mass density. The large field of view also allows for mapping the surface mass density at larger radii than before.

4.2 Conclusion

By looking at images obtained with a wide-field camera, the large field of view minimises some issues that could otherwise have been sources to errors

[10] section 3.2 and section 3.3

in the mass estimations. The $\kappa(r)$ reconstruction algorithm assumes the net mass inside the field to be zero[11], which is a cause to bias in the estimates. With a large field this bias is negligible, as the assumption is not far from the average mass distribution inside the field.

Comparing the profiles used to fit the data in this thesis shows that the NFW profile with both the concentration parameter and r_{200} altered through the fitting process gave the best fit results. The concentration parameters were quite different for the two clusters, and especially Abell 1351 gave a best fit c far from the generally considered best fit parameter. As earlier studies have also calculated a concentration parameter in this range (e.g. Kneib et al., 2003), it is not considered to be caused by errors in the estimation process. Using wide-field data also allows for mapping the mass density to further radii than done before, leading to better constraints on the concentration parameter.

The differences in the estimates of M_{200} between keeping c fixed or free is about $10^{14}\ h^{-1}\ \mathrm{M}_{\odot}$ for both clusters, implying that keeping c fixed can result in biases in the mass estimates. However, as this is within the error bars of both clusters the difference is not significant for the analysis of this thesis. If larger constraints could be set on the estimates, leading to the error bars to be lowered, the importance of applying the correct correction value is far more crucial.

Gavazzi (2005) looks into the topic of discrepancies between lensing and other mass estimations. He argues that these disagreements originates from the relative normalisation of two-dimensional and three-dimensional mass estimates. Further, by not assuming the dark matter and stellar components to be spherically symmetric distributed the discrepancies will not be as large as they are now.

4.3 Future studies

Knowing the best fit c parameter yields an approximate estimate of the scale radius of the galaxy cluster. The inner radius outside which the shear is measured can be varied to find the optimal radius, resulting in a more accurate mass estimate. Concluding with a large c value to be the best fit concentration parameter of a particular cluster implies a small scale radius, suggesting that a smaller inner radius in the shear measurements will result in a more precise mass estimation of that cluster. As this process is computationally intensive there was not sufficient time to carry it out in this study.

Given more time the K2K method could be carried out in addition, in order to compare the two methods and also obtain the most accurate analysis of the data. In addition strong lensing measurements could be applied to

[11] The data field is assumed to have an infinite spatial extend, see section 3.2.

the cluster centres to reveal more of the structure in these areas, and to test whether this might improve the mass estimates of this thesis.

Finally it would be interesting to fit the data to the cored power law profile (Kneib et al. 2003) in addition to the profiles fitted in this thesis. In contrast to the SIS and NFW profiles, the CPL profile is not a physically motivated model but rather a more general model. CPL has an arbitrary outer slope, a free parameter n yielding $\rho \propto r^n$ when $r \to \infty$.

Bibliography

[Abell (1958)] Abell, G. O. 1958, ApJS, 3, 211

[Abell et al. (1989)] Abell, G. O., Corwin, H. G., & Olowin, R. P. 1989, ApJS, 70, 1

[Allen et al. (2003)] Allen, S. W., Schmidt, R. W., Fabian, A. C., & Ebeling, H. 2003, MNRAS, 342, 287

[Böhringer et al. (2000)] Böhringer, H., et al. 2000, ApJS, 129, 435

[Broadhurst et al. (2005)] Broadhurst, T., Takada, M., Umetsu, K., Kong, X., Arimoto, N., Chiba, M., & Futamase, T. 2005, ApJL, 619, L143

[Bullock et al. (2001)] Bullock, J. S., Kolatt, T. S., Sigad, Y., Somerville, R. S., Kravtsov, A. V., Klypin, A. A., Primack, J. R., & Dekel, A. 2001, MNRAS, 321, 559

[Clowe et al. (2000)] Clowe, D., Luppino, G. A., Kaiser, N., & Gioia, I. M. 2000, ApJ, 539, 540

[Coles & Lucchin (2002)] Coles, P., & Lucchin, F. 2002, Cosmology: The Origin and Evolution of Cosmic Structure, Second Edition, by Peter Coles, Francesco Lucchin, pp. 512. ISBN 0-471-48909-3. Wiley-VCH , July 2002.,

[Comins & Kaufmann (2003)] Comins, N. F., & Kaufmann, W. J. 2003, Discovering the Universe, 6th edition, W.H. Freeman, 2003

[Dahle et al. (2003)] H. Dahle, S. Hannestad and J. Sommer-Larsen, 2003, ApJ, 588, L73

[Dühring (2002)] Dühring, M. 2002, Master's thesis, Niels Bohr Institutet for Astronomi, Fysik og Geofysik, Astronomical Observatory

[Gavazzi (2005)] Gavazzi, R. 2005, A&A, 443, 793

[Hawking (2003)] Hawking, S. 2003, The Penguin Dictionary of Physics, 3rd edition, the Penguin Group

[Heymanns et al. (2005)] C. Heymans et al., 2005, arXiv:astro-ph/0506112

[Hoekstra et al. (1998)] Hoekstra, H., Franx, M., Kuijken, K., & Squires, G. 1998, ApJ, 504, 636

[Howell (2000)] Howell, S. B. 2000, Handbook of CCD astronomy / Steve B. Howell. Cambridge, U.K. ; New York : Cambridge University Press, c2000

[Irgens et al. (2002)] Irgens, R. J., Lilje, P. B., Dahle, H., & Maddox, S. J. 2002, ApJ, 579, 227

[Kaiser (1995)] Kaiser, N. 1995, arXiv:astro-ph/9509019

[Kaiser (2000)] Kaiser, N. 2000, ApJ, 537, 555

[Kaiser & Squires (1993)] Kaiser, N., & Squires, G. 1993, ApJ, 404, 441

[Kaiser et al. (1995)] Kaiser, N., Squires, G., & Broadhurst, T. 1995, ApJ, 449, 460

[Kaiser et al. (1999)] Kaiser, N., Wilson, G., Luppino, G. & Dahle, H., 1999, arXiv:astro-ph/9907229

[Kneib et al. (2003)] Kneib, J.-P., et al. 2003, ApJ, 598, 804

[Luppino & Kaiser (1997)] Luppino, G. A., & Kaiser, N. 1997, ApJ, 475, 20

[Metzler et al. (2001)] Metzler, C. A., White, M., & Loken, C. 2001, ApJ, 547, 560

[Murdin (2001)] Murdin, P. 2001, Encyclopedia of Astronomy and Astrophysics, Institute of Physics Publishing, Bristol and Philadelphia

[Navarro et al. (1995)] Navarro, J. F., Frenk, C. S., & White, S. D. M. 1995, MNRAS, 275, 720

[Navarro et al. (1997)] Navarro, J. F., Frenk, C. S., & White, S. D. M. 1997, ApJ, 490, 493

[Narayan & Bartelmann (1997)] Narayan, R., & Bartelmann, M. 1997, arXiv:astro-ph/9606001

[Nelson (2003)] Nelson, D. 2003, The Penguin Dictionary of Mathematics, 3rd edition, the Penguin Group

[Patel et al. (2000)] Patel, S. K., et al. 2000, ApJ, 541, 37

[Pedersen & Dahle 2006] Pedersen & Dahle 2006, ApJ, to be submitted

[Refsdal (1964)] Refsdal, S. 1964, MNRAS, 128, 295

[Ridpath (2003)] Ridpath, I. 2003, Oxford Dictionary of Astronomy, revised edition, Oxford University Press

[Squires & Kaiser (1996)] Squires, G., & Kaiser, N. 1996, ApJ, 473, 65

[Walsh et al. (1979)] Walsh, D., Carswell, R. F., & Weymann, R. J. 1979, Nature, 279, 381

[Wold et al. (2002)] Wold, M., Lacy, M., Dahle, H., Lilje, P. B. & Ridgway, S. E. 2002, Mon. Not. Roy. Astron. Soc. 335, 1017, arXiv:astro-ph/0205336

[Wright & Brainerd (2000)] Wright, C. O., & Brainerd, T. G. 2000, ApJ, 534, 34

[Ytre-Eide (2003)] Ytre-Eide, M. 2003, C.Sc. thesis, Institute of Theoretical Astrophysics, University of Oslo

Appendix A

The shear-polarisation relation

The outline of the shear-polarisation relation given in this appendix is taken from Luppino & Kaiser (1997), with additional corrections from Hoekstra et al. (1998). The measured polarisation, e, will change when introduced to a gravitational shear, γ, as

$$e \rightarrow e' = e + \gamma P^{\gamma} \; . \tag{A.1}$$

The equation implies that the expectation value for the polarisation, $\langle e' \rangle$, is proportional to γ. This can be assumed because the expectation value of e will be very close to zero, $\langle e \rangle \approx 0$, due to the assumption that the galaxy shapes are randomly distributed in the absence of systematical gravitational lensing. It may be that close galaxies will have some gravitational effect on each other, but this effect is negligible when dealing with a large number of galaxies, as is the case with the data used in this thesis.

To be able to make an estimate of the shear and hence calculate the mass distribution of the galaxy cluster, the constant of the shear polarisability, the pre-seeing shear polarisability tensor, P^{γ}, must be determined. For this purpose a linear function of the observed galaxy surface brightness is used throughout this thesis[1]:

$$P^{\gamma} = P^{sh} - P^{sm} \frac{P^{sh\star}}{P^{sm\star}} \tag{A.2}$$

where P^{sh} and P^{sm} are the post-seeing shear polarisability tensor and the smear polarisability tensor respectively, defined in section 3.1.1, and $P^{sh\star}$ and $P^{sm\star}$ are the same tensors applied to stellar objects.

Ideally, a perfect image can be derived by observing with an instrument containing a Point Spread Function (PSF), g, that is perfectly circular. If a

[1] To show the general case the different parts of the equations will not contain subscripts throughout this appendix. However, they denote the same quantities as given by equations elsewhere in this thesis.

galaxy has an intrinsic surface brightness, f, the image observed with this instrument would have

$$f_\circ = g \otimes f \tag{A.3}$$

and from this the ideal polarisation $e = e(f_\circ)$ can be derived[2]. If a small PSF anisotropy is introduced by convolving g with a small kernel, q, this kernel being highly anisotropic, then

$$f_\circ \to f'_\circ = g' \otimes f = q \otimes g \otimes f \ . \tag{A.4}$$

As a result the polarisation will change

$$e \to e' = e + P^{sm} p \ , \tag{A.5}$$

where a measurement of the PSF anisotropy is given by p (as in equation (3.16)) and the smear polarisability can be obtained from the image $f'_\circ$ as $P^{sm} = P^{sm}(f'_\circ)$. The result derived here is used in section 3.1.2 in correcting for the PSF anisotropy.

By applying a shear to the perfect image

$$f_\circ \to f'_\circ = S^\gamma (g \otimes f) \ , \tag{A.6}$$

with the shear operator, S^γ, being defined such that

$$(S^\gamma h)_\theta = h[(\delta_{ij} + \psi_{ij})\theta_j] \tag{A.7}$$

with

$$\psi_{ij} = \begin{bmatrix} \gamma_1 & \gamma_2 \\ \gamma_2 & -\gamma_1 \end{bmatrix} \ , \tag{A.8}$$

the polarisation will change to linear order in γ as

$$e \to e' = e + P^{sh} \gamma \tag{A.9}$$

and P^{sh} can then be measured from the image as $P^{sh} = P^{sh}(f'_\circ)$.

By first convolving f with an anisotropic PSF, g', and then applying a weak shear

$$f' \to S^\gamma (g' \otimes f) \ , \tag{A.10}$$

this combined operation will lead to a shift in the polarisation given by

$$e' \to e^s + P^{sh}\gamma + P^{sm} p(g') \ , \tag{A.11}$$

being linear in both γ and p. However, as P^{sh} describes the polarisation effects of a shear that is applied after seeing, and the real lensing effects are applied before seeing, the γ - e relation cannot be calibrated using P^{sh} just

[2]Equation (A.3) denotes a convolution of g with f, see section B.4 for a further examination of this mathematical term.

as it is. If used as stated the response will tend to be overestimated when dealing with small objects.

It can be shown that the application of a shear followed by a convolution with a circularly symmetric seeing kernel, g, gives the exact same result as if the convolution was done with a slightly anisotropic anti-sheared kernel, $g' = [S^\gamma]^{-1}g$, first and then having the shear applied

$$f_\circ \rightarrow f'_\circ = g \otimes (S^\gamma f) = S^\gamma \left[([S^\gamma]^{-1}g) \otimes f \right] \ . \tag{A.12}$$

By smearing the perfectly circular PSF with a suitable kernel, q, the approximation can be made that this effect is fundamentally identical to that caused by the shear on the polarisation of a PSF anisotropy. This approximation is very good when dealing with seeing caused by atmospheric turbulence, resulting in

$$e \rightarrow e' = e + P^{sh}\gamma + P^{sm}p([S^\gamma]^{-1}g) \ . \tag{A.13}$$

Because stars are intrinsically point-like objects the shear has no effect on them and $e = e' = 0$. Applying equation (A.13) on stellar objects hence results in

$$p([S^\gamma]^{-1}g) = -\gamma \frac{P^{sh\star}}{P^{sm\star}} \ , \tag{A.14}$$

implying that, for a non-stellar object,

$$e \rightarrow e' = e + \gamma \left(P^{sh} - P^{sm} \frac{P^{sh\star}}{P^{sm\star}} \right) \ . \tag{A.15}$$

This is the same result as stated in equations (A.1) and (A.2).

As opposed to P^{sh} which only depends on the object shape, P^{sm} scales as the inverse area of the object. For large objects P^{sm} will therefore be much less than P^{sh}, and $P^\gamma \rightarrow P^{sh}$. For small objects the response is decreased by the negative term, and for stellar objects $P^\gamma \rightarrow 0$.

Appendix B

Mathematical definitions

The mathematical definitions and explanations described in this appendix are taken from the web pages of Mathworld, http://mathworld.wolfram.com/, and the two Penguin dictionaries of Mathematics and Physics.

B.1 Stereographic projection

By projecting the points P' on the surface of a sphere from the sphere's north pole, N, to a point P in a plane tangent to the south pole, S, their stereographic projection are obtained. As shown in Figure B.1 this is simply a map projection.

The stereographic projections of Figure B.2 have a simple algebraic form. The relative positions of the projection plane and z-axis leads to a variety of different transformation formulae. These can be listed as (starting from top left going to the right)

$$\begin{array}{lll} P' = \frac{2r}{2r-z}P & P' = \frac{2r}{z}P & P' = \frac{r}{z}P \\ P' = \frac{2r}{r-z}P & P' = \frac{2r}{r+z}P & P' = \frac{r}{r+z}P \; . \end{array} \tag{B.1}$$

B.2 Taylor series

A Taylor series is a series expansion of a real function $f(x)$ about a point $x = a$. Taylor's theorem expresses the function as the sum of a polynomial and a remainder,

$$\begin{aligned} f(x) = f(a) + f'(a)(x-a) + f''(a)\tfrac{(x-a)^2}{2!} \\ + f'''(a)\tfrac{(x-a)^3}{3!} + \cdots + R_n \; . \end{aligned} \tag{B.2}$$

Here R_n is the remainder after n terms, given by

$$R_n = \frac{1}{n!}h^n f^{(n)}(a + h\theta) \tag{B.3}$$

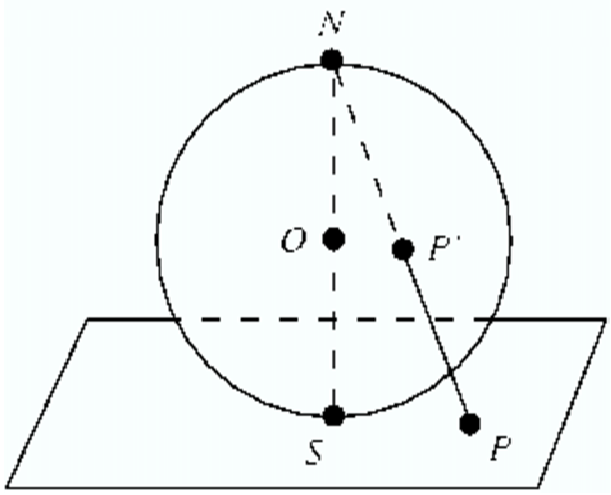

Figure B.1: The map projection.

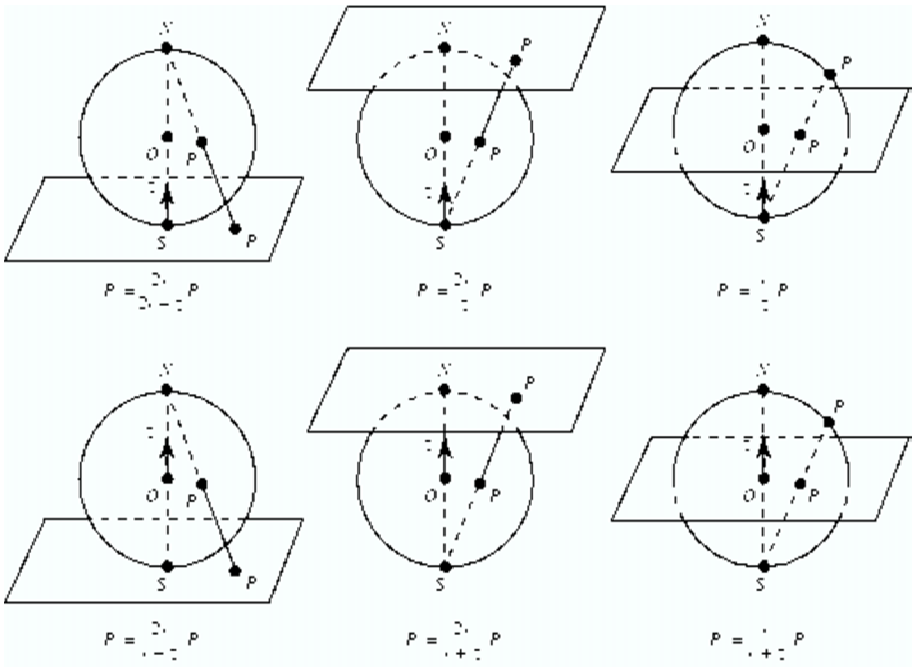

Figure B.2: The stereographic projection. The stereographic spheres have radius r and z-axis as shown.

where $h = (x - a)$ and θ lies between 0 and 1.

If $n \to \infty$ this expansion is a Taylor series. If also $R_n \to 0$ as $n \to \infty$, it represents the function given by equation (B.2). The series is called a Maclaurin series if $a = 0$.

B.3 The Bessel functions

The Bessel functions occur in many applications in physics and engineering, for example in problems of heat conduction. They are power series in x that satisfy the Bessel's equation, this being a second-order differential equation of the form

$$x^2 \frac{d^2y}{dx^2} + x\frac{dy}{dx} + (x^2 - n^2)y = 0 \,, \tag{B.4}$$

where n is a constant indicating the order of the Bessel's equation.

$J_n(x)$ denote the Bessel functions of the first kind, these being the most important of the Bessel functions. These functions are the solutions to the Bessel's equation being non-singular at the origin, and are given by

$$J_n(x) = \frac{1}{\pi}\int_0^\pi \cos(nt - x\sin t)dt \tag{B.5}$$

$$= \sum_{r=0}^{\infty} \frac{(-1)^r}{r!\,\Gamma(n+r+1)} \left(\frac{x}{2}\right)^{n+2r} \,. \tag{B.6}$$

n is a nonzero integer denoting the order of the Bessel function. The series form is only valid if n is a positive integer. Figure B.3 plots $J_n(x)$ for $n = 0, 1, \ldots, 5$.

Bessel functions of the second kind (also called Neumann functions) are denoted $Y_n(x)$, and are simple combinations of Bessel functions. They are also solutions to the Bessel's equation, but now being singular at the origin. Bessel functions of the third kind are special combinations of the first and second kinds, also called Hankel functions.

B.4 Convolution

The convolution of two functions $f(x)$ and $g(x)$ is an integral expressing the amount of overlap of f as it is shifted over g. This is done such that the convolution of f and g over a finite range $[0, x]$ is given by

$$f \otimes g = \int_0^x f(t)g(x - t)dt \,, \tag{B.7}$$

where the symbol $\otimes$ denotes the convolution.

Convolution taken over an infinite range is expressed as

$$f \otimes g = \int_{-\infty}^{\infty} f(t)g(x - t)dt = \int_{-\infty}^{\infty} g(t)f(x - t)dt \,. \tag{B.8}$$

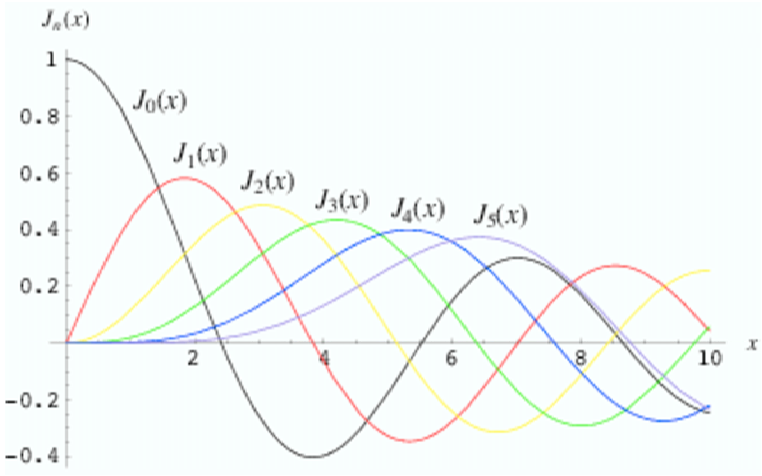

Figure B.3: Bessel functions of the first kind of orders $n = 0, 1, \ldots, 5$.

B.5 Maximum likelihood

Likelihood is the hypothetical probability that an already occurred event would generate a particular outcome. It refers to past events with known outcomes as opposed to a probability that refers to the occurrence of future events. For a continuous random variable X with frequency function $f(x;\alpha)$, the likelihood function is $f(x_i;\alpha)$, corresponding to the observation x_i. $f(x_i;\alpha)$ is considered a function of α, α being the parameter of the distribution. Given n independent observations, $x_1, x_2, \ldots, x_n$, from this distribution the likelihood function is given by

$$L = f(x_1;\alpha)f(x_2;\alpha)\cdots f(x_n;\alpha)\ . \tag{B.9}$$

The maximum likelihood estimation is a procedure where the likelihood is maximised by an estimator of the parameter of the distribution. Differentiating the logarithm of the likelihood function with respect to α to find the maximum value is a well used method in obtaining the estimates.

Appendix C

IMCAT

The IMCAT software was developed by Nick Kaiser[1] initially to carry out faint galaxy photometry for weak lensing. IMCAT is optimised for shape measurements of faint galaxies and weak lensing and provides a fairly complete set of tools for weak lensing analysis. The tools are arranged in a tree of directories with three main branches: `imtools` that deal only with FITS files, `cattools` that operate only on catalogues and `imcattools` that tend to be more specialised than the two previous branches, focusing on faint galaxy photometry.

Weak lensing occurs in every cluster. It is, however, difficult to measure because of the ellipticities present in the background galaxies. This represents the main source of noise in weak lensing analysis. In addition, the weak shear signal is suppressed by the occurrence of the faint galaxies being smeared by the seeing point spread function (PSF) and therefore circularise the galaxy images[2]. The PSF may also contain anisotropies that makes it dependent on the location in the image. IMCAT consists of advanced techniques for measuring galaxy ellipticities and correcting for these errors which makes it a very good tool to use in weak lensing analysis. The facts about IMCAT presented here can be found on the IMCAT homepage, http://www.ifa.hawaii.edu/ kaiser/imcat/content.html.

C.1 Using IMCAT

The IMCAT commands are invoked from the shell, via shell scripts or from Perl scripts like all standalone UNIX commands. All IMCAT commands have an instruction manual[3] that is viewed by adding the *-u* option to the command.

[1] kaiser@hawaii.edu, http://www.ifa.hawaii.edu/~kaiser/

[2] section 3.1

[3] Some of these instruction manuals can be somewhat unclear to new users.

This can be very useful as there are no textbooks written on IMCAT[4]. The IMCAT commands all take different options, using the default value if none is specified. There are also commands that are actually *Perl* scripts performing several IMCAT commands after each other and thereby making it easier for the user to execute. These types of commands clearly facilitate the usage of IMCAT as some of the simple IMCAT commands put restrictions on the image to be executed. An example is *chunkyfp* that runs the command *(h)findpeaks* on a large image by cutting it in pieces, executing the command on each piece and putting the pieces back together when executed. This is fortunate because (h)findpeaks can only be executed on images no bigger than a certain size.

The IMCAT imtools are made for image processing files stored in the FITS[5] format. Non-IMCAT images are assumed to be stored in the big-endian byte order decreed by the NASA NOST FITS definition[6]. This is, however, inefficient when used with little-endian machines like Linux on PC, so Kaiser decided to store the images in native format. In order to use IMCAT it is therefore necessary to filter the images through *changesex* first to switch the byte order of the FITS file from big-endian to little-endian. To make the the files work with non-IMCAT software they have to be switched back to the original byte order.

The command *ic* (image calculator) is the most important of the imtools. By using ic it is possible to carry out general operations on FITS images, such as subtracting one image from another or combining images to make a median image where the median value from different exposures but centred on the same pixel is chosen.

To work with catalogues IMCAT uses the cattools branch of the IMCAT tree. cattools contains a number of commands that makes it possible to detect and store objects from the FITS files in catalogues as well as making required FITS files from information given in the catalogues. IMCAT provides a large number of tasks to be performed on several catalogues at the same time, such as comparing them to find objects present in both catalogues or finding transformation parameters between the object coordinates, to name but a few others.

The format of the catalogues is defined by *lc* (list catalogue) which generates an ASCII format listing of a catalogue as its default mode. However, lc is very useful for manipulating catalogues by using the numerous command line options. The lc program processes catalogues one object at a time[7] by reading the object from standard input, performing a manipulation on the object and writing the result to standard output. The type of manipula-

[4]There are however a few articles written about image processing and analysis of weak lensing material using IMCAT, see Kaiser et al., 1999 and Wold et al., 2002.

[5]Flexible Image Transport System

[6]http://fits.gsfc.nasa.gov/

[7]lc is similar to the UNIX command awk for this task.

tion to be performed is specified by options on the command line, with both scalars, vectors and matrices allowed as entries. The fact that `lc` can also read and write in binary format results in a large gain in efficiency.

To visualise the catalogues graphically `IMCAT` uses *plotcat*. This program is based on `PGPLOT` - a FORTRAN subroutine package for drawing simple scientific graphs, originally developed for use with astronomical data reduction programs[8].

C.1.1 Perl

When executing the same `IMCAT` commands on a number of images one after each other, *Perl*[9] is an ideal programming language to use for this purpose. It is very straight forward, both to learn and to use and also flexible when it comes to performing the same task on several images one after the other. By making a list (*listname.db*) of the exposure names Perl accesses a new name each time the loop is executed. By utilising a second loop and a list containing just the chip numbers each image is treated separately.

Perl attempts to fill the gap between low-level programming and high-level programming[10]. It is not necessary to compile Perl manually; when Perl is run its internal compiler first runs through the entire source turning it into byte-codes and then Perl's byte-code engine actually runs them. This means it is fast to run; every loop and every calculation is just compiled once and then run at top speed and comments and white spaces do not slow down the process. Figure C.1 shows a simple example of a Perl script, where the task of the script is just to change the name of the file. As seen in the script, the subroutine *echosys* prints the command to the terminal window from where the script is run and also executes the same command in `IMCAT`, printing an error message if the call to `IMCAT` fails.

[8] http://www.astro.caltech.edu/~tjp/pgplot/

[9] Practical Extraction and Report Language (Learning Perl, Schwartz & Phoenix, O'Reilly 2001) or - as stated in the textbook - Pathologically Eclectic Rubbish Lister.

[10] C and C++ are examples of low-level programming languages while "shell" programming is high-level.

```
#! /usr/bin/perl
# Script: example.pl
# Perl script to show an example of how it can be done

require "images.db";
#goes through every exposure
for ($i = 0; $i < $nimages; $i++) {
  #"wordslist.list" is a list of the numbers 00 - 12 in 2 digits
  open (WORDSLIST, "wordslist.list") || die "can't open wordslist.list: $!";

  #goes through every chip of the same exposure
  while ($number = <WORDSLIST>) {
    chomp($number);
    $oldfile = $homedir.$imname[$i].$number.".fits";    #old file
    $newfile = $homedir.$imname[$i].$number.".new";     #new file

    #change the name of the file
    echosys("mv $oldfile $newfile");
  }
}

sub echosys {
  print @_, "\n";
  system(@_) && die "$0: System call $_[0] failed!\n";
}
```

Figure C.1: An example of a simple Perl script.